

FIRST MOMENT OF AZIMUTHAL ANISOTROPY IN AU+AU COLLISIONS FROM THE
BEAM ENERGY SCAN AT THE RELATIVISTIC HEAVY ION COLLIDER

A dissertation submitted
to Kent State University in partial
fulfillment of the requirement for the
degree of Doctor of Philosophy

By

Prashanth Shanmuganathan

August, 2016

© Copyright

All rights reserved

Except for previously published materials

Dissertation written by

Prashanth Shanmuganathan

B.Sc. (Physics, Honors), University of Colombo, 2009

Ph.D., Kent State University, 2016

Approved by

Dr. Declan Keane, Chair, Doctoral Dissertation Committee

Dr. Spyridon Margetis, Members, Doctoral Dissertation Committee

Dr. Veronica Dexheimerz

Dr. Deng-Ke Yang

Dr. Jonathan Selinger

Accepted by

Dr. James T. Gleeson, Chair, Department of Physics

Dr. James L. Blank, Dean, College of Arts and Sciences

TABLE OF CONTENTS

TABLE OF CONTENTS	iii
LIST OF FIGURES	vii
LIST OF TABLES	xvii
ACKNOWLEDGEMENTS	xix
1. INTRODUCTION	1
1.1. The Big Bang, Quark Gluon Plasma and Quantum Chromodynamics	1
1.2. Ultra-Relativistic Heavy Ion Collisions	3
1.2.1. Scanning the QCD Phase Diagram via Heavy Ion Collisions	5
1.3. The Beam Energy Scan Program at STAR	7
1.3.1. Signatures of QGP Formation	7
1.3.1.1. Elliptic Flow Measurements	9
1.3.1.2. Jet Quenching	10
1.3.2. Search for Critical Point	12
1.3.3. Search for First-Order Phase Transition	13
1.4. Dissertation Outline	13
2. DIRECTED FLOW AND THE SEARCH FOR A FIRST-ORDER PHASE TRANSITION	15
2.1. Anisotropic Flow	16
2.1.1. Introduction	16
2.1.2. Fourier Expansion	17
2.1.3. Flow Harmonics	18

2.1.3.1.	Directed Flow	18
2.1.3.2.	Elliptic Flow	19
2.1.3.3.	Higher Harmonics	20
2.2.	Directed Flow and a Possible First-Order Phase Transition	20
2.3.	Selected Directed Flow Results	21
2.3.1.	Experimental Measurements	22
2.3.1.1.	NA49	22
2.3.1.2.	AGS-E895	23
2.3.1.3.	STAR-BES Phase-I	25
2.3.2.	Models With Relevance to Directed Flow	26
2.3.2.1.	Hadronic Transport Model (UrQMD)	26
2.3.2.2.	Ideal Hydrodynamics with Isochronous Freeze-Out	27
2.3.2.3.	Frankfurt Hybrid Model	28
2.3.2.4.	Parton-Hadron-String Dynamics Model	29
2.3.2.5.	Jet AA Microscopic (JAM) Transport Model	31
3.	EXPERIMENTAL SETUP	34
3.1.	The Relativistic Heavy Ion Collider	34
3.2.	The STAR Experiment	36
3.2.1.	The Time Projection Chamber	37
3.2.2.	Time of Flight detector	41
3.2.3.	Beam Beam Counters	43
4.	ANALYSIS	45
4.1.	Data	45
4.1.1.	Event Selection	45
4.1.2.	Centrality Selection	47
4.1.3.	Track Selection	50

4.2. Particle Identification	50
4.2.1. π^\pm, K^\pm and $p(\bar{p})$ Identification	50
4.2.2. Reconstructing $\Lambda, \bar{\Lambda}, K_S^0$ and yields	53
4.2.2.1. Mixed Event Background Estimation	56
4.2.2.2. Side Band Background Estimation	57
4.2.2.3. Rotational Background Estimation	58
4.3. BBC Event Plane Calculation	59
4.3.0.1. Shift Correction	61
4.3.0.2. Event Plane Resolution	63
4.4. Directed Flow Measurements	65
4.4.1. Directed Flow of Charged Particles – $\pi^\pm, K^\pm, p(\bar{p})$	66
4.4.2. Directed Flow of Neutral Strange Particles – $\Lambda, \bar{\Lambda}, K_S^0$	66
4.4.3. Systematic Uncertainties	68
4.4.3.1. Detector Acceptance and Efficiency	69
5. EXPERIMENTAL RESULTS	74
5.1. V_0 Invariant Mass Distributions	74
5.2. Rapidity Dependence of Directed Flow	77
5.2.1. Intermediate Centrality Au+Au Collisions	77
5.2.1.1. BES Data Analysis	78
5.2.1.2. UrQMD Model Calculations	82
5.2.1.3. Systematic Uncertainty Study	85
5.2.1.4. Net-Particle Directed Flow	91
5.2.1.5. Summary of Intermediate Centrality Results	93
5.2.2. Peripheral and Central Au+Au Collisions	95
5.2.3. Different Definitions of Wide Centrality Bins	97
5.3. Centrality Dependence of Directed Flow	99

6. SUMMARY AND OUTLOOK 112

 6.1. Summary 112

 6.2. Outlook 115

BIBLIOGRAPHY 123

APPENDICES

 A. SERVICE WORK FOR THE STAR COLLABORATION 125

 A.1. STAR Collaboration’s Record System Upgrade 125

 A.2. Lead-Scintillating Fiber Calorimeter for STAR Forward Tracking 126

LIST OF FIGURES

Figure 1.1. The energy density in l QCD calculations as a function of temperature. The arrows on the right show the energy density values for an ideal Stefan-Boltzmann gas. This figure is reproduced from Ref. [2].	2
Figure 1.2. A possible schematic phase diagram of QCD matter. The solid lines show the boundaries between different phases. The blue dot labeled “Critical Point?” indicates the possible end point of a first-order phase boundary between the hadronic and QGP phases.	3
Figure 1.3. Space-time evolution of a relativistic heavy-ion collision. This figure is reproduced from Ref. [11].	4
Figure 1.4. A schematic version of the QCD phase diagram. Some of the quantitative details shown, like trajectories corresponding to collisions at specific beam energies, are speculative. This figure is reproduced from Ref. [16].	7
Figure 1.5. STAR’s measurement of v_2 as a function of transverse kinetic energy ($m_T - m$), both scaled by n_Q , for 0-80% central Au+Au collisions at six beam energies. This figure is reproduced from Ref. [27].	9
Figure 1.6. Nuclear modification factor (R_{CP}) as a function of transverse momentum for charged hadrons produced in Au+Au collisions at STAR. This figure is reproduced from Ref. [16].	12
Figure 1.7. $\kappa\sigma^2$ for net protons as a function of beam energy for 0-5% and 70-80% central Au+Au collisions. This figure is from [35].	13

Figure 2.1. The cartoon on the left shows the overlapping (participant) region in a heavy-ion collision. The cartoons on the right illustrate how the initial spatial anisotropy of the participants in the xy plane is transferred to the final-state momentum anisotropy in the $p_x p_y$ plane. 16

Figure 2.2. Visualization of the contribution from each flow harmonic to the deviation from isotropic azimuthal emission of final-state particles. 18

Figure 2.3. Schematic cartoon of Directed flow. 19

Figure 2.4. Directed flow of protons and charged pions as a function of rapidity for $40A$ and $158A$ GeV Pb+Pb collisions. Data points are mirrored at negative rapidity. This figure is reproduced from Ref. [53] published by the NA49 collaboration at CERN. Note that fixed-target experiments normally give the kinetic energy of the beam ions per nucleon in the laboratory frame, which is not the same convention as $\sqrt{s_{NN}}$ defined earlier. 22

Figure 2.5. Beam energy dependence of the slope of $\langle p_x(y) \rangle$ for 1.2, 2, 4, 6, 8 and $11.5A$ GeV Au+Au fixed-target collisions. The linear term F in a cubical fit function, $Fy + Cy^3$, is used to extract the slope. This analysis is based on normalized rapidity, where the projectile and target are always at ± 1 by definition. This figure is reproduced from Ref. [55]. 24

Figure 2.6. The left side shows an older definition of directed flow (average p_x) for protons and Λ s as a function of normalized center of mass rapidity in 2, 4, 6 and $8A$ GeV Au+Au fixed-target collisions. The open circles shows reflected data points. On the right side, panel (a) shows the slope of $\langle p_x(y) \rangle$ as a function of beam energy using a linear fit. Panel (b) shows this slope, in the form of a ratio for Λ over proton, as a function of beam energy. This figure is reproduced from Ref. [59]. 25

Figure 2.7. Directed flow slope, dv_1/dy , near midrapidity for 7.7, 11.5, 19.6, 27, 39, 62.4 and 200 GeV 10-40% central Au+Au collisions for protons, antiprotons and π^\pm . Measurements from NA49 [53] and E895 [55] with comparable but not identical cuts are also plotted. This figure is reproduced from Ref. [49].	26
Figure 2.8. Directed flow from the UrQMD model, compared with STAR BES measurements.	27
Figure 2.9. Ideal three-fluid hydrodynamic calculation of directed flow for net baryons from Au+Au collisions at intermediate centrality. Star markers correspond to EOS with the assumption of a first-order phase transition. The red arrow indicates the trend of directed flow assuming an EOS without a phase transition. This figure is based on calculations reported in Ref. [43].	28
Figure 2.10. Proton v_1 slope from the hybrid model, and from the hybrid code with Boltzmann transport turned off, in order to show two cases of pure hydrodynamics. Experimental results are shown as green markers. This figure is reproduced from Ref. [63].	29
Figure 2.11. Directed flow slope $F = dv_1/dy$ near midrapidity as a function of beam energy for protons, antiprotons, and π^- in intermediate-centrality Au+Au collisions. Experimental measurements from STAR [49], NA49 [53], and E895 [55] are also shown. Shaded bands show UrQMD results from Ref. [49]. This figure is reproduced from Ref. [64].	31
Figure 2.12. Proton and π^- directed flow in 10-40% central Au+Au collisions at $\sqrt{s_{NN}} = 7.7 - 27$ GeV. Standard JAM and attractive JAM models are compared with STAR measurements [49]. This figure is reproduced from Ref. [68].	33
Figure 3.1. The gold ion acceleration scheme at RHIC. In the figure (1)–EBIS, (2)–Linac, (3)–Booster, (4)–AGS, (5)–AGS to RHIC transfer line, (6)–RHIC rings. This figure is reproduced from Ref. [74].	36

Figure 3.2. Diagram of the STAR experiment and some of its subsystems. The end-cap electromagnetic calorimeter (EEMC) is pulled back in this diagram, allowing more of the internal details of STAR to be viewed.	37
Figure 3.3. The STAR Time Projection Chamber (TPC). This figure is reproduced from Ref. [75].	38
Figure 3.4. One of the TPC pad plane sectors. This figure is reproduced from Ref. [75].	39
Figure 3.5. Real time event display for a gold+gold event reconstructed in the TPC. When all tracks are projected onto a single plane as in these examples, the density of tracks appears to be very high.	41
Figure 3.6. Side and end view of a TOF multigap resistive plate chamber (MRPC) module. This figure is reproduced from Ref. [78].	42
Figure 3.7. Illustration of the relative positions of TPC, VPD and TOF detectors with respect to the beam pipe. A single tray of TOF MRPC modules is indicated. This figure is reproduced from Ref. [80].	43
Figure 3.8. A single beam-beam counter (BBC) array of scintillator tiles.	44
Figure 4.1. Black data points shows normalized $\frac{dN_{\text{events}}}{dN_{\text{ch}}^{\text{raw}}}$ distributions for BES energies. The three shaded bands shows the centrality classes for central (0-10%) intermediate (10-40%) and peripheral (40-80%) collisions. The red histogram shows Monte Carlo Glauber simulations. This figure is reproduced from Ref. [81].	48
Figure 4.2. The plot on the left shows energy loss (dE/dx) for all particles as a function of electric charge times momentum in the TPC detector. The plot on the right shows dE/dx after particle identification cuts based on information from both TOF and TPC.	51
Figure 4.3. The mass^2 distribution from the TOF detector without any cuts for particle identification.	53
Figure 4.4. $V0$ decay topology diagram.	55

Figure 4.5. Illustration of mixed $V0$ event background estimation for Λ at $\sqrt{s_{NN}} = 11.5$ GeV for 10-40% centrality. Panel (a) shows the signal+background and the mixed event background; panel (b) shows the same after the background is normalized; and panel (c) presents the invariant mass peak for Λ after background subtraction.	57
Figure 4.6. This plot illustrates the side band method in the case of the Λ signal. Vertical and horizontal axes are truncated for better clarity. S_0 , S_1 , and S_2 are signal + background entries, while B_0 , B_1 , and B_2 are background entries. . . .	58
Figure 4.7. On the left is shown the west and east BBC detectors, for positive and negative η , respectively. On the right is shown the inner two rings of the BBC. The red numeral is tile number and blue numeral is the PMT number; these two are not always the same, since the read-out of tiles 7 and 9, and of 13 and 15, are coupled together.	59
Figure 4.8. Raw event plane distribution for east, west and full event plane calculations.	61
Figure 4.9. The shift-corrected event plane distribution for east, west and full event plane calculations. The distributions for 27 GeV and 39 GeV are scaled by factors of 0.75 and 0.5, respectively.	63
Figure 4.10. First order event plane resolution for all BES energies.	65
Figure 4.11. Histogram of signal+background (left) and normalized mixed-event background (right) for Λ as a function of invariant mass and $\phi - \Psi_{RP}$. These histograms are for 30-40% centrality Au+Au collisions at $\sqrt{s_{NN}} = 19.6$ GeV, with rapidity $0.2 < y \leq 0.4$	67
Figure 5.1. Invariant mass distribution of Λ for 10-40% centrality at $\sqrt{s_{NN}} = 11.5$ GeV. The solid blue histogram shows signal + background. The blue shaded area shows the mixed event background. The solid red area shows background-subtracted Λ candidates.	75

Figure 5.2. Invariant mass distribution of K_S^0 for 10-40% centrality at $\sqrt{s_{NN}} = 11.5$ GeV. The solid blue histogram shows signal + background. The blue shaded area shows the mixed event background. The solid red area shows background-subtracted K_S^0 candidates.	75
Figure 5.3. Λ invariant mass in thirty bins of $(\phi - \Psi_{RP})$ is shown for $-0.8 \leq y \leq -0.6$ and 30-40% centrality Au+Au collisions at a beam energy of 11.5 GeV.	76
Figure 5.4. K_S^0 invariant mass in thirty bins of $(\phi - \Psi_{RP})$ is shown for $0.4 \leq y \leq 0.6$ and 20-30% centrality Au+Au collisions at a beam energy of 7.7 GeV.	77
Figure 5.5. Directed flow (v_1) as a function of rapidity for p , Λ , \bar{p} , $\bar{\Lambda}$, K^\pm , K_S^0 and π^\pm for 10-40% centrality Au+Au collisions. Error bars are statistical. The v_1 magnitude is exceptionally large for $\bar{\Lambda}$ at 7.7 GeV, and therefore in that panel only, v_1 and its errors are divided by 5 to fit on the common vertical scale.	79
Figure 5.6. dv_1/dy near mid-rapidity as a function of beam energy for p , \bar{p} , π^\pm , Λ and $\bar{\Lambda}$ for 10-40% central Au+Au collisions. The dv_1/dy for $\bar{\Lambda}$ at 7.7 GeV is -0.13 ± 0.02 , which lies off-scale, below the lower end of the vertical axis. Error bars are statistical.	81
Figure 5.7. dv_1/dy near mid-rapidity as function of beam energy for K^+ , K^- and K_S^0 for 10-40% central Au+Au collisions. Error bars are statistical.	82
Figure 5.8. Directed flow as a function of rapidity for p , Λ , \bar{p} , $\bar{\Lambda}$, K^\pm , K_S^0 and π^\pm for 10-40% central UrQMD Au+Au collisions. Error bars are statistical. The v_1 magnitude is exceptionally large for \bar{p} and $\bar{\Lambda}$ at 7.7 and 11.5 GeV, and therefore for only for those four panels, v_1 and its errors are divided by 5 to fit on the common vertical scale.	83
Figure 5.9. The left panel shows dv_1/dy near mid-rapidity as function of beam energy for p , \bar{p} , π^\pm , Λ and $\bar{\Lambda}$ from UrQMD events for 10-40% central Au+Au collisions. Similarly, the right panel is for K^\pm and K_S^0 . Error bars are statistical.	84

Figure 5.10. Error from systematic variations is shown by the shaded band for v_1 vs. y , for particles Λ , $\bar{\Lambda}$ and K_S^0 , in 10-40% central collisions at a beam energy of 11.5 GeV.	86
Figure 5.11. Error from systematic variations is shown by the shaded band for v_1 vs. y , for particles Λ , $\bar{\Lambda}$ and K_S^0 , in 10-40% central collisions at a beam energy of 39 GeV.	87
Figure 5.12. Error from systematic variations is shown by the shaded band for v_1 vs. y , for particles p , \bar{p} , π^\pm and K^\pm , in 10-40% central collisions at a beam energy of 11.5 GeV. The systematic error for π^\pm is small and is not visible on the scale of this plot.	88
Figure 5.13. Error from systematic variations is shown by the shaded band for v_1 vs. y , for particles p , \bar{p} , π^\pm and K^\pm , in 10-40% central collisions at a beam energy of 39 GeV. The systematic error for π^\pm is small and is not visible on the scale of this plot.	89
Figure 5.14. The effect from different sources of systematic error is shown for dv_1/dy from 10-40% central collisions at a beam energy of 11.5 GeV on left and of 39 GeV on right. The cut number is defined in Table 4.4 and 4.5 for Λ and $\bar{\Lambda}$ baryons, and in Table 4.6 and 4.7 for K_S^0 . For Λ and $\bar{\Lambda}$, cut number 33 is the final data point with systematic and statistical errors, cut number 34 corresponds to systematic errors from event and track quality cuts, and cut number 35 includes only $V0$ systematic errors. For K_S^0 , cut number 19 is the final data point with systematic and statistical errors.	90
Figure 5.15. The effect from different sources of systematic error is shown for dv_1/dy from 10-40% central collisions at a beam energy of 11.5 GeV. The cut number is defined in Table 4.8 for p and \bar{p} , and in Table 4.9 for π^\pm and K^\pm . Cut number 15 is the final data point with systematic and statistical errors.	91

Figure 5.16. dv_1/dy near mid-rapidity at 10-40% centrality for net protons, net Λ s and net kaons.	92
Figure 5.17. Slope of v_1 near mid-rapidity as a function of beam energy for protons, antiprotons, Λ , $\bar{\Lambda}$, and π^\pm for 10-40% central collisions. Solid data points show BES data and shaded bands show UrQMD calculations. The dv_1/dy for $\bar{\Lambda}$ at 7.7 GeV is -0.13 ± 0.02 , which lies off-scale, below the lower end of the vertical axis. Error bars are statistical, while caps show systematic errors.	94
Figure 5.18. Slope of v_1 near mid-rapidity as a function of beam energy for K^\pm and K_s^0 for 10-40% central collisions. Solid data points show BES data and shaded bands show UrQMD calculations. Error bars are statistical, while caps show systematic errors.	95
Figure 5.19. Directed flow (v_1) as a function of rapidity for p , Λ , \bar{p} , $\bar{\Lambda}$, K^\pm , K_s^0 and π^\pm in 0-10% centrality Au+Au collisions. Error bars are statistical. The v_1 magnitude is exceptionally large for \bar{p} and $\bar{\Lambda}$ at 7.7 and 11.5 GeV, and hence for only those panels, v_1 and its errors are divided by 5 to fit on the common vertical scale. . .	96
Figure 5.20. Directed flow (v_1) as a function of rapidity for p , Λ , \bar{p} , $\bar{\Lambda}$, K^\pm , K_s^0 and π^\pm in 40-80% centrality Au+Au collisions. Error bars are statistical. The v_1 magnitude is exceptionally large for \bar{p} and $\bar{\Lambda}$ at 7.7 and 11.5 GeV, and hence for only those panels, v_1 and its errors are divided by 5 to fit on the common vertical scale. . .	97
Figure 5.21. Comparison of dv_1/dy for different combinations of centrality bins with the default intermediate-centrality class. Error bars are statistical.	99
Figure 5.22. dv_1/dy near midrapidity as a function of centrality for p . Top panel from STAR data and bottom panel is from UrQMD. Error bars are statistical. In general, systematic errors are comparable to statistical errors, but are omitted to reduce clutter.	101

Figure 5.23. dv_1/dy near midrapidity as a function of centrality for Λ . Top panel from STAR data and bottom panel is from UrQMD. Error bars are statistical. In general, systematic errors are comparable to statistical errors, but are omitted to reduce clutter.	102
Figure 5.24. dv_1/dy near midrapidity as a function of centrality for π^+ . Top panel from STAR data and bottom panel is from UrQMD. Error bars are statistical. In general, systematic errors are comparable to statistical errors, but are omitted to reduce clutter.	103
Figure 5.25. dv_1/dy near midrapidity as a function of centrality for π^- . Top panel from STAR data and bottom panel is from UrQMD. Error bars are statistical. In general, systematic errors are comparable to statistical errors, but are omitted to reduce clutter.	104
Figure 5.26. dv_1/dy near midrapidity as a function of centrality for K^+ . Top panel from STAR data and bottom panel is from UrQMD. Error bars are statistical. In general, systematic errors are comparable to statistical errors, but are omitted to reduce clutter.	105
Figure 5.27. dv_1/dy near midrapidity as a function of centrality for K^- . Top panel from STAR data and bottom panel is from UrQMD. Error bars are statistical. In general, systematic errors are comparable to statistical errors, but are omitted to reduce clutter.	106
Figure 5.28. dv_1/dy near midrapidity as a function of centrality for K_S^0 . Top panel from STAR data and bottom panel is from UrQMD. Error bars are statistical. In general, systematic errors are comparable to statistical errors, but are omitted to reduce clutter.	107
Figure 5.29. Systematic error for dv_1/dy as a function of centrality is shown for p , Λ , π^+ and π^- at a beam energy of 11.5 GeV.	108

Figure 5.30. Systematic error for dv_1/dy as a function of centrality is shown for p , Λ , π^+ and π^- at a beam energy of 39 GeV. 109

Figure 5.31. Systematic error for dv_1/dy as a function of centrality is shown for K^\pm and K_S^0 at a beam energy of 39 GeV. 110

Figure 5.32. Systematic error for dv_1/dy as a function of centrality is shown for K^\pm and K_S^0 at a beam energy of 39 GeV. 111

Figure A.1. GEANT drawing of the prototype built in 2014. A cross-sectional view of the calorimeter cells (FCal) and pre-shower (PS) detector is shown, along with the STAR detector and the beam pipe. 127

Figure A.2. GEANT drawing of the proposed arrangement of annular calorimeter cells, to be placed on the west side of the STAR detector. The calorimeter cells are shown in green. 128

LIST OF TABLES

Table 1.1. Beam energy scan results from various particle accelerators, converted to μ_B and T_{ch} values using a thermal model. For RHIC energies below 7.7 GeV, the points are interpolations, and cover energy points that are on track to be investigated using the STAR experiment in fixed target mode in 2019 and 2020. The values are extracted from Ref. [17–19]	8
Table 4.1. Statistics and energy-dependent cuts and parameters.	47
Table 4.2. $N_{\text{ch}}^{\text{raw}}$ for nine centrality bins at BES energies.	49
Table 4.3. V0 topological cuts for Λ and K_S^0 particles. A momentum-dependent lower mass cut for pions is selected to reject contamination from electron misidentification. All lengths are in centimeters and all masses are in GeV/c^2	55
Table 4.4. Minimum and maximum event and track cuts used for systematic study of $\Lambda(\bar{\Lambda})$. The cut number is a unique identifier assigned to each minimum and maximum cut value, used later to identify that variation in the plots. All lengths are in centimeters, all momenta are in GeV/c and all masses are in GeV/c^2	70
Table 4.5. Minimum and maximum p_T , V0 and decay daughter track cuts used to estimate systematic errors for $\Lambda(\bar{\Lambda})$. The cut number is a unique identifier assigned to each minimum and maximum cut, used later to identify that variation in the plots. All lengths are in centimeters, all momenta are in GeV/c and all masses are in GeV/c^2	71

Table 4.6. Minimum and maximum event and track cuts used to estimate systematic errors for K_S^0 . The cut number is a unique identifier assigned to each minimum and maximum cut, used later to identify that variation in the plots. All lengths are in centimeters.	71
Table 4.7. Minimum and maximum p_T , $V0$ and decay daughter track cuts used to estimate systematic errors for K_S^0 . The cut number is a unique identifier assigned to each minimum and maximum cut, used later to identify that variation in the plots. All lengths are in centimeters, and all momenta are in GeV/c	72
Table 4.8. Minimum and maximum event and track cuts used to estimate systematic errors for protons. The cut number is a unique identifier assigned to each minimum and maximum cut, used later to identify that variation in the plots. All lengths are in centimeters, all momenta are in GeV/c and all masses are in GeV/c^2	73
Table 4.9. Minimum and maximum events cuts used to estimate systematic errors for pions and kaons. The cut number is a unique identifier assigned to each minimum and maximum cut, used later to identify that variation in the plots. All lengths are in centimeters, all momenta are in GeV/c and all masses are in GeV/c^2	73
Table 5.1. Summary of the event statistics used in UrQMD simulations. For reference, real event statistics are also shown.	82
Table 5.2. Alternative groupings of coarse centrality bins.	98

ACKNOWLEDGEMENTS

First of all I would like to thank the taxpayers of United States of America, for the vast amount of research money that they have devoted. I have tried my best to justify each taxpayer dollar spent, in my dissertation analysis.

I would like to express my special appreciation to my dear advisor and mentor Professor Dr. Declan Keane. From the day one he has offered me continuous support for my studies and research. I also want to thank him for helping on my presentations, preparing for the conferences, and writing my thesis. My advisor allowed me to station in Brookhaven national laboratory, helped me to work on multiple projects with different experts in my field, which helped to enrich the experience. I could not have imagined having a better Ph.D. advisor.

I am grateful to Dr. Les Bland, Dr. Hank Crawford and Dr. Jack Engelage for giving opportunity to work on hadronic calorimeter project, and for their enormous amount of time that they spent on educating me on calorimeter development. It was my pleasure to work with them.

I am indebted to Dr. Jerome Lauret and Dr. Dmitry Arkhipkin for helping me to learn new software technologies and for the time that they spent on guiding me to meet the standards in developing new software tools, during their busy schedule.

I would like to thank members of STAR collaboration with whom I have interacted during the dissertation analysis. Particularly, I would like to thank Prof. Lokesh Kumar, Prof. Mike Lisa, Prof. Bill Llope, Dr. Akio Ogawa, Dr. Yadav Pandit, Prof. Margetis Spyridon, Dr. Alexander Schmah, Dr. Subhash Singha, Dr. Gang Wang, Dr. Jason Webb, Dr. Zhangbu Xu, Dr. Nu Xu, Dr. Wei-Ming Zhang for valuable discussions and advises that helped me during the Ph.D.

I would like to thank our graduate secretaries Loretta Hauser (who mothered many of us during initial hard time), Constance Reho and Kelly Conley, our grant secretary Ida Cellitti, STAR secretary Liz Mogavero and staff of international office at Kent State University for their assistance in office work. I am also grateful to all of my teachers, lecturers, professors, lab assistants and technicians who took important roll in my academic career.

Finally, I would like to thank my wife Nithiya and my dear parents for their love and courage, which bring me as a successful person in life.

CHAPTER 1

INTRODUCTION

1.1 The Big Bang, Quark Gluon Plasma and Quantum Chromodynamics

The Big Bang model tells us that the universe we see now was born 13.8 billion years ago, from a cosmic singularity. There is considerable evidence that the medium created a few microseconds after the Big Bang was an extremely hot (10^{22} °K) and dense (10^{90} Kg/cm³) primeval fireball. At this high temperature and density, the created medium is dominated by quarks and gluons, which are the known fundamental constituents of strongly-interacting matter. The state of quarks and gluons when they are not confined is called Quark-Gluon Plasma. As the universe rapidly expanded and cooled, the quark and gluons went through a phase transition to form composite particles called hadrons. The force between quarks is relatively weak at short distances (like the radius of a proton or less), but becomes much stronger at longer distances. This property is called asymptotic freedom: two or more quarks move freely only within small volumes (they are 'deconfined'), a statement that can be reformulated in terms of interactions at high energy. Quantum Chromodynamics (QCD) describes the strong interaction between quarks and gluons. Like photons in Quantum Electrodynamics (QED), the gluons in QCD are the mediators of the strong force. However, gluons experience the strong force among themselves, by exchange of so-called color charge, a mechanism that has no parallel among the photons of QED.

This confined hadronic phase of quarks and gluons, and the deconfined QGP phase, are predicted in lattice QCD (ℓ QCD) calculations. In the numerical ℓ QCD approach, space and time are treated as discrete lattice points [1]. Figure 1.1 shows energy density as a function of

temperature in units of critical temperature (T/T_c) [2]. Another important state variable is the baryon chemical potential, μ_B , a measure of net-baryon density. Near the critical temperature, ℓ QCD shows a sudden change in the energy density, suggesting changes in the degrees of freedom in the system. These calculations also imply that the phase boundary between QGP and hadron gas near zero μ_B is a crossover, and the corresponding critical temperature is about 154 MeV [3–7]. A crossover transition very likely happened in the early expansion of the universe. ℓ QCD and other models hint that the transition becomes discontinuous at high μ_B , becoming a first-order phase transition [8, 9]. Figure 1.2 shows a conjectured phase diagram of QCD matter in the plane of temperature and baryon chemical potential, with different possible phases [10].

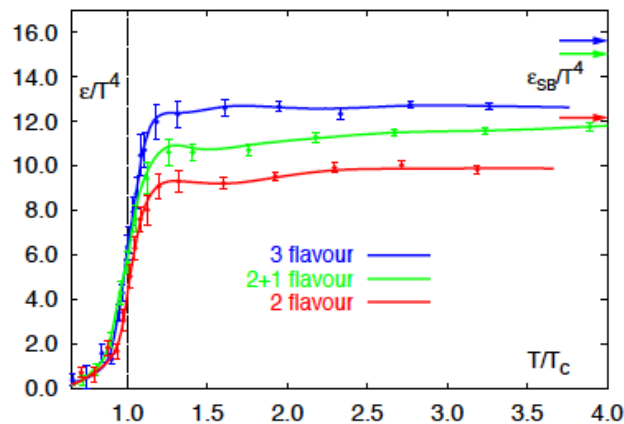


Figure 1.1: The energy density in ℓ QCD calculations as a function of temperature. The arrows on the right show the energy density values for an ideal Stefan-Boltzmann gas. This figure is reproduced from Ref. [2].

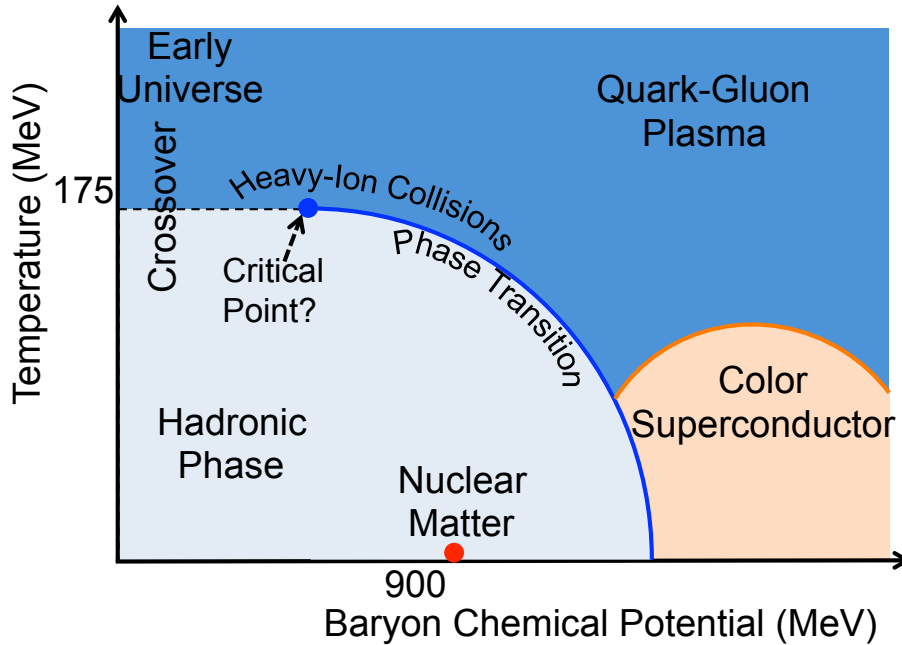


Figure 1.2: A possible schematic phase diagram of QCD matter. The solid lines show the boundaries between different phases. The blue dot labeled “Critical Point?” indicates the possible end point of a first-order phase boundary between the hadronic and QGP phases.

1.2 Ultra-Relativistic Heavy Ion Collisions

In the laboratory, QGP can be created for a very brief time in a heavy-ion collision at ultra-relativistic energies. It has been speculated that a crossover might occur between hadronic matter and QGP throughout the accessible region of the phase diagram, and therefore there would be no first-order phase transition and no critical end point if this speculation were to be correct. However, a majority of theorists advocate the picture represented in Figure 1.2. The search for evidence of a first-order phase transition and/or of a critical point is a major objective of the field of experimental heavy-ion physics. In an ultra-relativistic nuclear collision, heavy ions such as gold, uranium, or copper are accelerated to $\sqrt{s_{NN}} \sim 10$ GeV or above (this Mandelstam notation denotes the energy per initial-state nucleon pair in the center of mass frame). To achieve higher temperature and energy density, i.e., significantly above $\sqrt{s_{NN}} \sim 10$ GeV, collider-type accelerators are needed.

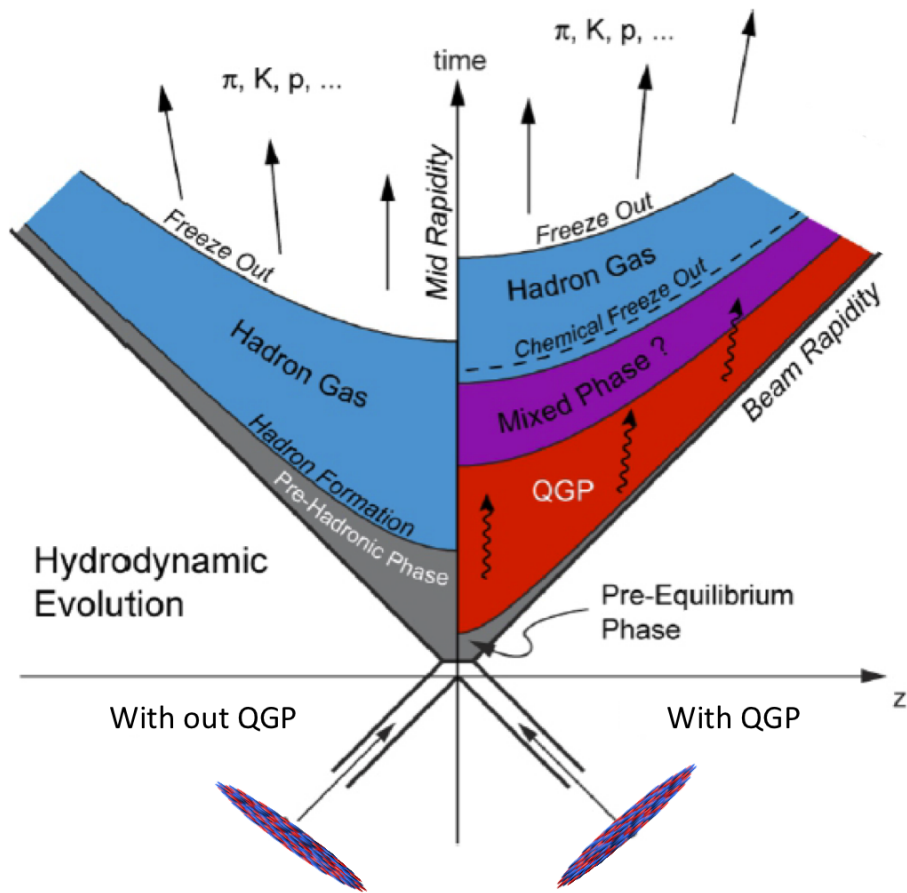


Figure 1.3: Space-time evolution of a relativistic heavy-ion collision. This figure is reproduced from Ref. [11].

Figure 1.3 illustrates the evolution of a relativistic heavy-ion collision in space-time. At relativistic speeds, spherical ions are Lorentz contracted along the beam direction, and take the form of highly oblate ellipsoids. When the two nuclei collide, interactions start in the overlapped region (the participant zone). At the lower end of the beam energy region of interest, there is partial stopping, whereby some of the initial baryon number (which must be conserved) is slowed down to the rapidity (velocity) of the center of mass frame. This produces a dense region of finite μ_B where QGP is likely to be formed for a brief time. At much higher beam energies, there is less stopping of the initial baryons, and the central fireball is characterized by $\mu_B \sim 0$; in this case, QGP is formed with a higher degree of certainty.

The system evolution during a nuclear collision can be separated into several stages. First, during the time of pre-equilibrium (less than 1 fm/c) hard scattering of partons (quarks or gluons) occurs. A large amount of energy is deposited into the participant region, creating a fireball. Next, after the pre-equilibrium stage, a QGP is expected to form, and the system approaches thermal equilibrium, at least locally. Due to the enormous energy density (about 3 to 5 GeV/fm³) and high temperature (0.2 to 0.3 GeV), the fireball experiences an outward pressure gradient. This pressure gradient leads the fireball to expand and its temperature decreases. A crossover or first-order phase transition may occur. In the next stage, the collective expansion continues, and the system is mostly in a hadronic phase. At a temperature (T_{ch}), the system density reaches a point where inelastic interactions cease, and the abundances of the various particle species in the final state is fixed. This stage is called chemical freeze out. After this point, no new particles are created, and particle multiplicity is fixed. Then the system further expands, and the mean free path between the particles continues to increase. At a temperature (T_{KE}), the mean free path become larger than the system radius, and even elastic interactions cease. This final stage is called kinetic or thermal freeze out.

1.2.1 Scanning the QCD Phase Diagram via Heavy Ion Collisions

The net baryon number is fixed for a given pair of colliding nuclei, and all the measurements analyzed in this dissertation come from a single heavy system: gold on gold ($^{197}\text{Au} + ^{197}\text{Au}$). As the collision energy increases, the amount of energy transferred to the fireball increases, and it freezes out at a decreasing baryon chemical potential. Therefore, the collision energy can be related to the temperature and baryon chemical potential at the point of chemical freeze out. Experimentally, the chemical freeze out surface and the kinetic freeze out surface are estimated by combining thermal model calculations with measurements of particle yields and transverse momentum distributions. At each beam energy, the ideal goal would be to map the explored region of the QCD phase diagram at the time when phase boundaries are crossed.

However, knowledge of the explored region of the QCD phase diagram at the later time of chemical freeze out is also useful and important.

The Beam Energy Scan program (BES) was initiated by the Relativistic Heavy Ion Collider (RHIC) community to explore the predicted critical point and the region of the predicted first-order phase transition in the QCD phase diagram. The Solenoidal Tracker At RHIC (STAR) [12] and the Pioneering High Energy Nuclear Interaction eXperiment (PHENIX) [13] are the two functioning experiments at RHIC. BES Phase-I was completed in 2014, and RHIC is preparing for BES Phase-II, including fixed target experiments, in 2019 and 2020. Various experiments at the Super Proton Synchrotron (SPS) [14] in CERN, Switzerland, and at the Alternating Gradient Synchrotron (AGS) [15] at Brookhaven National Laboratory have also contributed insightful measurements in or near the beam energy region explored in this dissertation. The beam energies studied at CERN's Large Hadron Collider (LHC) are very high, and are essentially limited to $\mu_B = 0$, where we know that QGP always involves a crossover transition. Figure 1.4 shows an alternative schematic phase diagram for QCD matter. Chemical and kinetic freeze out curves are illustrated. However, many of the other quantitative details on this version of the phase diagram (like trajectories corresponding to collisions at specific beam energies) are speculative. Table 1.1 summarizes a set of T_{ch} and μ_B points, mostly extracted by varying the beam energy in different experiments.

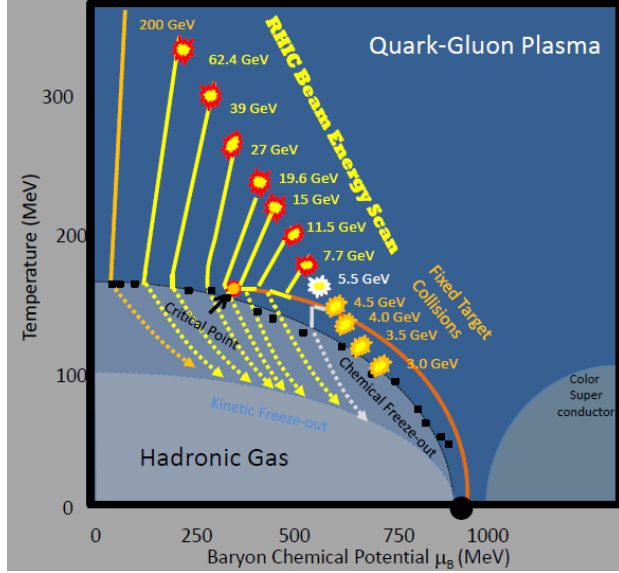


Figure 1.4: A schematic version of the QCD phase diagram. Some of the quantitative details shown, like trajectories corresponding to collisions at specific beam energies, are speculative. This figure is reproduced from Ref. [16].

1.3 The Beam Energy Scan Program at STAR

Analyses in this dissertation are based on measurements at the STAR experiment during Phase-I of the BES program (sometimes denoted BES-I). This subsection presents selected results from STAR BES-I.

1.3.1 Signatures of QGP Formation

Many signatures of QGP formation have been proposed. Certain measurements at the full energy of RHIC ($\sqrt{s_{NN}} = 200$ GeV) have been argued to be evidence of QGP [20–24]. Generally speaking, one signature alone is not highly compelling, but the combined weight of several signatures has in practice been considered to be reasonably strong evidence of QGP. One of the goals of the BES-I program was to map-out the evolution of some of the $\sqrt{s_{NN}} = 200$ GeV QGP signatures as the beam energy drops, step-by-step, down to 7.7 GeV. A few such signatures are discussed in the subsections below.

Table 1.1: Beam energy scan results from various particle accelerators, converted to μ_B and T_{ch} values using a thermal model. For RHIC energies below 7.7 GeV, the points are interpolations, and cover energy points that are on track to be investigated using the STAR experiment in fixed target mode in 2019 and 2020. The values are extracted from Ref. [17–19]

	$\sqrt{s_{NN}}$ (GeV)	Baryon Chemical Potential (μ_B)	Temperature T_{ch} (MeV)
LHC	2760.0	2	166
RHIC	200.0	24	165.9
RHIC	130.0	36	165.8
RHIC	62.4	73	165.3
RHIC	39.0	112	164.2
RHIC	27.0	156	162.6
RHIC	19.6	206	160.0
SPS	17.3	229	158.6
RHIC	14.5	262	156.2
SPS	12.4	299	153.1
RHIC	11.5	316	151.6
SPS	8.8	383	144.4
RHIC	7.7	422	139.6
SPS	7.7	422	139.6
SPS	6.4	476	131.7
RHIC	4.9	562	118
AGS	4.7	573	114.6
RHIC	4.5	589	111
AGS	4.3	602	108.8
RHIC	3.9	633	101
AGS	3.8	638	100.6
RHIC	3.5	666	93
AGS	3.3	686	88.9
RHIC	3.0	721	76
AGS	2.7	752	70.4
SIS	2.3	799	55.8

1.3.1.1 Elliptic Flow Measurements

Collective flow deduced from azimuthal anisotropy in heavy-ion collisions can provide insight into the equation of state (EOS) of the produced medium. The plane formed by the beam axis and the vector connecting the centers of the two colliding nuclei is called the reaction plane. The azimuthal anisotropy of emitted particles with respect to the the azimuth of the reaction plane can be expressed in Fourier harmonics. Elliptic flow, v_2 , is the second harmonic coefficient in the Fourier expansion.

For light and strange hadrons at the top beam energy of RHIC, a large magnitude of v_2 is observed and the values are consistent with hydrodynamic calculations for deconfined quarks and gluons [25, 26].

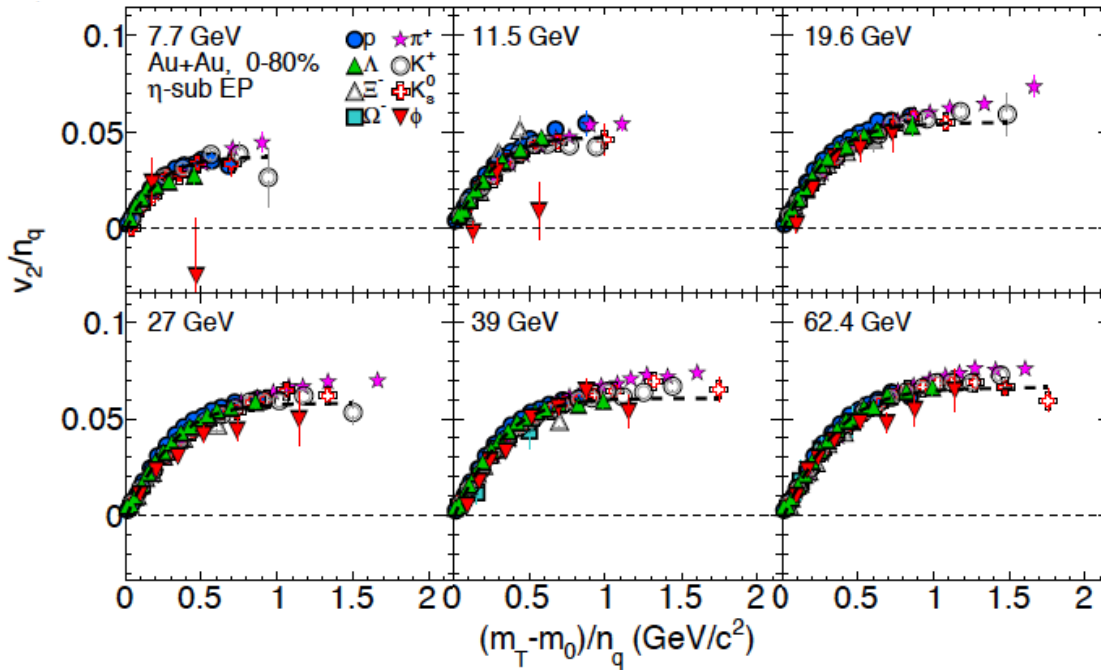


Figure 1.5: STAR's measurement of v_2 as a function of transverse kinetic energy $(m_T - m)$, both scaled by n_Q , for 0-80% central Au+Au collisions at six beam energies. This figure is reproduced from Ref. [27].

When interpreting elliptic flow for various identified particle species, an important scaling quantity is n_Q , the number of constituent quarks in that particle type. Thus, $n_Q = 2$ for mesons

and $n_Q = 3$ for baryons. Figure 1.5 shows v_2 as a function of transverse kinetic energy, both scaled by n_Q , for 0-80% central Au+Au collisions at 7.7, 11.5, 19.6, 27, 39 and 62.4 GeV. Over the studied range of transverse kinetic energy at the higher beam energies, the unscaled v_2 curves for mesons and baryons are quite different, yet the mesons and baryons are seen to line-up closely (within $\sim 10\%$) on a common curve over a wide range of transverse kinetic energy [27]. This scaling behavior is consistent with a picture where the elliptic flow is imposed on the excited matter while it is still in a deconfined partonic phase, i.e., it is imposed when deconfined quarks rather than baryons and mesons are the relevant degrees of freedom. However, this interpretation might be an oversimplification [28].

At top RHIC energies, particles and antiparticles show similar behavior in plots where n_Q scaling is tested, but at lower energies, particles and antiparticles diverge, while each separately follows the scaling behavior. The ϕ meson, which has a relatively small hadronic interaction cross section and whose mass is typical of a baryon, shows a v_2 that is consistent with zero and lies below that of other hadrons at 7.7 and 11.5 GeV. A possible interpretation is that hadronic rather than partonic interactions become dominant at these lower energies. Unfortunately, the ϕ -meson statistics are very poor, casting any interpretation into doubt.

1.3.1.2 Jet Quenching

Particles at high transverse momentum, p_T , are associated with very energetic (hard) scattering of partons. Such processes often result in the emission, within a narrow solid angle, of several energetic particles — a jet. To conserve momentum, two back-to-back jets (dijets) are normally created. In $p + p$ collisions, this dijet pattern is consistently observed. However, in heavy-ion collisions, a common geometric arrangement results in one of the jets in a dijet traversing the volume where a QGP exists, where it is absorbed or greatly attenuated, while the other jet, escaping in the opposite direction, is unimpeded by any nuclear matter. This phenomenon is called jet quenching in partonic matter [29] and is one of the important signatures of QGP.

One of several ways to detect jet quenching uses an observable called the nuclear modification factor,

$$R_{CP} = \frac{\langle N_{\text{bin}}^{\text{peri}} \rangle d^3 N_{AA}^{\text{cen}} / d\eta d^2 p_T}{\langle N_{\text{bin}}^{\text{cen}} \rangle d^3 N_{AA}^{\text{peri}} / d\eta d^2 p_T},$$

where N^{peri} and N^{cen} correspond to particle yields in peripheral and central collisions, respectively, while $N_{\text{bin}}^{\text{peri}}$ and $N_{\text{bin}}^{\text{cen}}$ are the number of expected binary collisions for peripheral and central collisions, respectively, commonly estimated from a model. If there is no jet quenching effect in central heavy-ion collisions, then $R_{CP} \sim 1$ should always be observed.

Figure 1.6 shows R_{CP} for charged hadrons as a function of transverse momentum for 7.7, 11.5, 19.6, 27, 39 and 62.4 GeV Au+Au collisions measured by STAR [16]. The results show, for $p_T > 2.0$ GeV/c, that there is strong enhancement relative to unity at lower beam energies, and then we observe a smooth transition to strong suppression at higher beam energies.

Suppression of R_{CP} at higher energies is related to the opacity of a deconfined medium of quarks and gluons, which leads to one of the better signatures of the formation of QGP, while the observed enhancement at lower energies could be due to hadronic interactions. At the lower energies, there is no apparent evidence for suppression at high p_T , but this could be simply a consequence of statistics running out before reaching the relevant region of p_T . The proposed increased statistics in BES-II will again help us to reach a more conclusive interpretation.

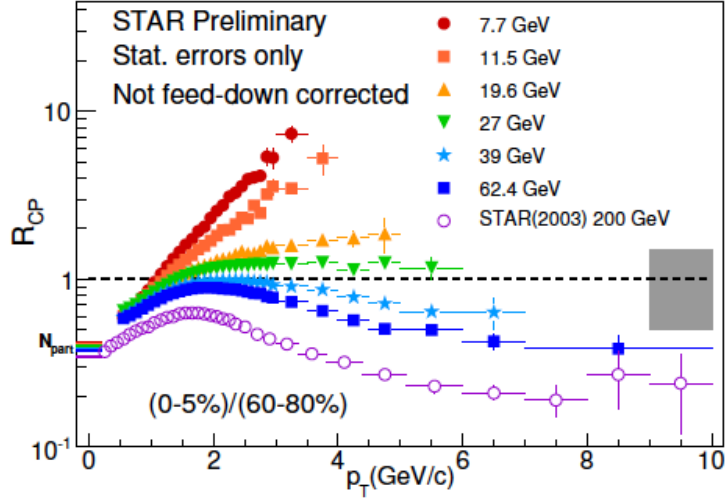


Figure 1.6: Nuclear modification factor (R_{CP}) as a function of transverse momentum for charged hadrons produced in Au+Au collisions at STAR. This figure is reproduced from Ref. [16].

1.3.2 Search for Critical Point

Various moments of conserved quantities, such as net-charge (Q), net-baryons (B), net-strangeness (S), ought to show large fluctuations or non-monotonic behavior near a critical point. Correlation length (ξ) is a measure of how ordered a thermal system is, and is very sensitive to critical point fluctuations. In heavy-ion collisions at RHIC, theory suggests that ξ can be 2-3 fm [30]. Higher moments of the distribution of conserved quantities are of particular interest. Theory suggests that the higher moments $\langle(\delta N)^3\rangle \sim \xi^{4.5}$ and $\langle(\delta N)^4\rangle \sim \xi^7$ are more sensitive to critical point fluctuations than the variance ($\sigma^2 = \langle(\delta N)^2\rangle$), due to stronger dependence on ξ [31]. In addition, models show that the moments of net-baryon distributions are related to baryon number susceptibilities, allowing direct comparisons to lattice QCD [32].

Lattice QCD calculations imply that the product kurtosis ($\kappa = \langle(\delta N)^3\rangle$) times variance (σ^2), which is proportional to the ratio of the fourth order baryon number susceptibilities to the second order, shows large deviations from unity near a critical point [33]. Therefore, $\kappa\sigma^2$ for net protons and net charge in STAR data are used to search for possible fluctuations arising from

a critical point. Measuring event-by-event net-baryon number is difficult, but theory suggests that the net-proton number is a useful proxy for net baryons [34].

Figure 1.7 shows the beam energy dependence of net-proton $\kappa\sigma^2$ for 0-5% and 70-80% central Au+Au collisions [35]. Net-proton $\kappa\sigma^2$ shows a weak hint of non-monotonic behavior at BES energies.

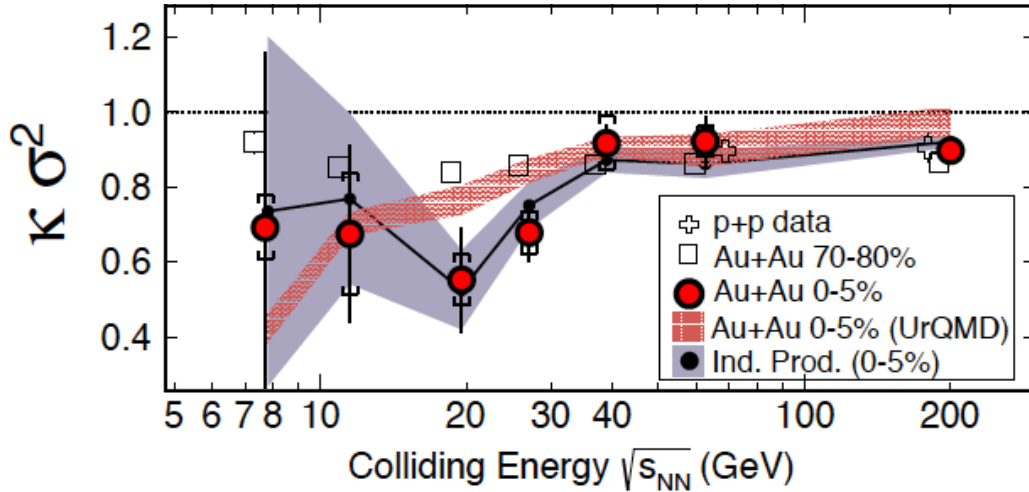


Figure 1.7: $\kappa\sigma^2$ for net protons as a function of beam energy for 0-5% and 70-80% central Au+Au collisions. This figure is from [35].

1.3.3 Search for First-Order Phase Transition

Lattice QCD predicts a first-order phase transition below a critical temperature, T_C [36]. Possible softening of the equation of state has been predicted to be visible in directed flow, v_1 , and past measurements at STAR support this picture. Directed flow measurements and the search for a possible first-order phase transition are the main topics of this dissertation, and I will discuss this in depth in Chapter 2.

1.4 Dissertation Outline

This dissertation emphasizes the search for a possible first-order phase transition from hadronic matter to QGP and back again, using azimuthal anisotropy measurements. The studied data

are Au+Au collisions from Phase-I of the RHIC Beam Energy Scan program at center-of-mass energy per nucleon pair of ($\sqrt{s_{NN}}$) 7.7, 11.5, 14.5, 19.6, 27 and 39 GeV. In this dissertation, I present the first measurement of directed flow near mid-rapidity for several identified particles types, namely Λ , $\bar{\Lambda}$, K_s^0 and K^\pm . In addition, the first centrality dependence of directed flow is presented for Λ , p , π^\pm , K_s^0 , and K^\pm .

The rest of this dissertation is organized as follows. The second chapter describes the measurement of anisotropy of produced particles in heavy-ion collisions, and summarizes recent theoretical literature on the topic of possible phase transitions and directed flow. In the third chapter, I discuss the experimental facility used for heavy-ion experiments, and the STAR detector and its subsystems. The fourth chapter describes analysis methods, and the fifth chapter presents results. In chapter six, I summarize the results and the outlook for future research in this area of nuclear collisions.

CHAPTER 2

DIRECTED FLOW AND THE SEARCH FOR A FIRST-ORDER PHASE TRANSITION

The search for a first-order phase transition via directed flow measurements is one of the primary physics objectives of this dissertation research. In practice, a realistic milestone that can be reached by the end of this dissertation is to make significant progress towards this longer-term physics objective. First, this chapter describes anisotropic flow and flow harmonics. Then I summarize the arguments that motivate the search for a first-order phase transition in the QCD phase diagram via directed flow measurements. Third, some existing directed flow results from experimental measurements and theoretical models are presented.

2.1 Anisotropic Flow

2.1.1 Introduction

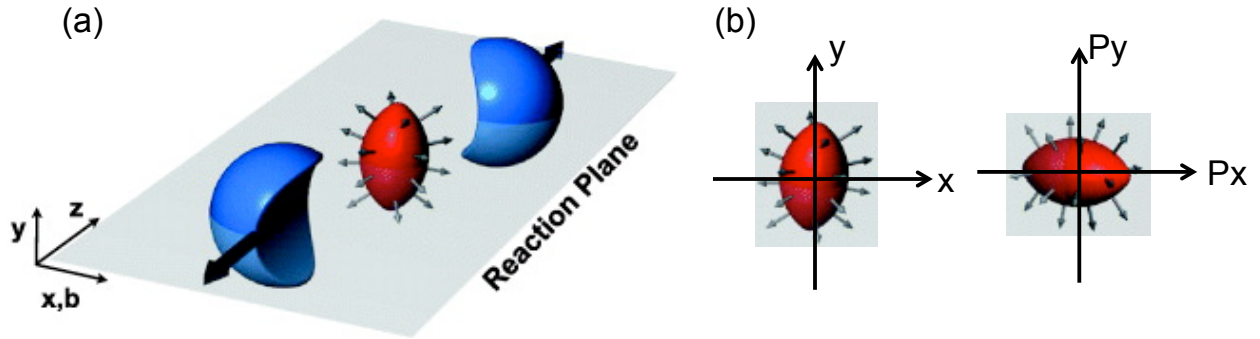


Figure 2.1: The cartoon on the left shows the overlapping (participant) region in a heavy-ion collision. The cartoons on the right illustrate how the initial spatial anisotropy of the participants in the xy plane is transferred to the final-state momentum anisotropy in the $p_x p_y$ plane.

The hot and dense matter formed in heavy-ion collisions rapidly expands and cools down, and the particles created during this process move collectively outward due to the high pressure in the system. Particle detectors measure the flow of these particles a long time after the interaction process has ended. By convention, the beam direction is denoted as the z axis, while in models, the perpendicular axis in which the centers of the two nuclei are separated is by convention always denoted as the x axis. The xz plane is known as the reaction plane, and the impact parameter, b , is the x separation between the centers of the two colliding nuclei before the interaction begins. However, in experiment, the x direction is fixed in the laboratory, and therefore the reaction plane is randomly oriented.

In a non-central heavy-ion collision, the almond-shaped overlap (participant) region has a larger pressure gradient along the x axis, due to the geometry of the collision. This pressure gradient causes particles to re-scatter and convert the initial spatial anisotropy into momentum-space anisotropy. Figure 2.1(a) is a cartoon representing the almond-shaped participant region in a heavy-ion collision and (b) illustrates the early spatial anisotropy on the left, with

the final-state momentum anisotropy, after re-scattering of particles, illustrated on the right. Models indicate that the spatial asymmetry lasts for very brief time (less than $2 \text{ fm}/c$ at the full energy of RHIC), and the resulting momentum-space anisotropy is imparted at an early stage of the evolution. Therefore, anisotropic flow can probe transport properties and can provide information about the equation of state (EOS) of the medium created in heavy-ion collisions.

2.1.2 Fourier Expansion

The azimuthal anisotropy of produced particles with respect to the reaction plane is conventionally expanded in a Fourier series [37]

$$E \frac{d^3 N}{dp^3} = \frac{1}{2\pi} \frac{d^2 N}{p_T dp_T dy} \left(1 + \sum_{n=1}^{\infty} 2v_n \cos n(\phi - \Psi_{\text{RP}}) \right) \quad (2.1)$$

where ϕ is the azimuthal angle of a particle, Ψ_{RP} is the azimuth of the reaction plane, and the coefficients v_n are called the flow harmonics. In a mass-symmetric system like Au+Au, which is the only case studied in this dissertation, sine terms in the Fourier expansion vanish due to reflection symmetry with respect to the reaction plane. In an experiment, the azimuth Ψ_{RP} can only be estimated, and the finite resolution associated with the estimated reaction plane (usually called the event plane), biases the extracted flow harmonic measurements v_n towards smaller values unless corrected. The flow signal itself is used to calculate the azimuth of the event plane, and there is a separate event plane Ψ_m corresponding to each harmonic of order m . The event plane angle for the m^{th} harmonic covers the range $0 \leq \Psi_m \leq 2\pi/m$. A flow measurement v_n can be evaluated for any event plane harmonic provided that $n \geq m$. In this dissertation analysis, the measurement of flow and the calculation of the event plane harmonic and its resolution is confined to the case $n = m = 1$, and specific details are explained in Section 4.3.

2.1.3 Flow Harmonics

Normalizing Eq. (2.1) gives us the observed Fourier coefficients for the flow harmonics

$$v_n(p_T, y) = \langle \cos n(\phi_i - \Psi_n) \rangle \quad (2.2)$$

where angle brackets denotes an average over all particles in all events. For a given collision centrality, the coefficients v_n are functions of rapidity (y) and transverse momentum (p_T). In some experiments, v_n might be averaged over rapidity and transverse momentum. Here, the index n is the Fourier (or flow) harmonic. The first harmonic ($n = 1$) is called directed flow (v_1), the second harmonic ($n = 2$) is called elliptic flow (v_2) and the third harmonic ($n = 3$) is called triangular flow (v_3). An example of imposing different flow harmonics on an isotropic azimuthal distribution is illustrated in Figure 2.2. Directed flow is similar to a sideward bounce of the two colliding nuclei. Elliptic flow deforms the azimuthal emission pattern in a way that is similar to the deviation of an ellipse from a circle.

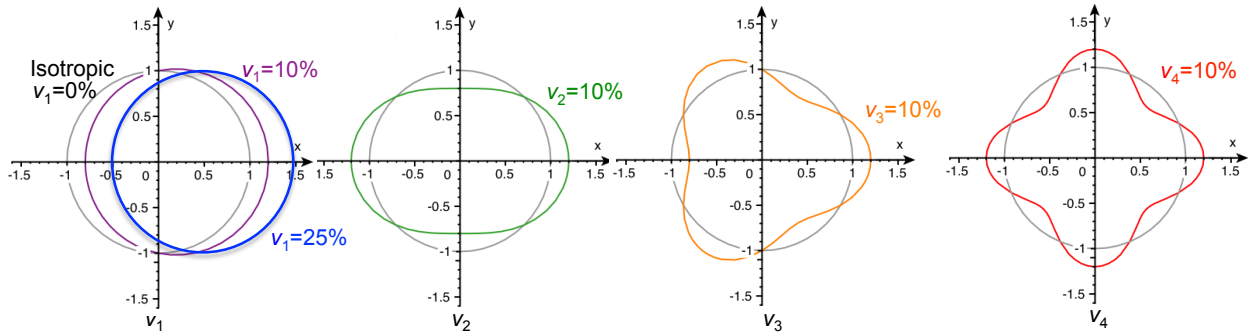


Figure 2.2: Visualization of the contribution from each flow harmonic to the deviation from isotropic azimuthal emission of final-state particles.

2.1.3.1 Directed Flow

The main anisotropy of interest in this dissertation is directed flow, the first harmonic in the Fourier expansion, and the first-order reaction plane Ψ_1 is the only relevant reaction plane: $v_1 = \langle \cos(\phi_i - \Psi_1) \rangle$. During a heavy-ion collision, the dense matter in the participant region

causes a repulsive sideward deflection in the reaction plane of the participant matter and, to a much smaller extent, the spectator matter. This deflection resembles a sideward bounce. Figure 2.3 is a cartoon that illustrates this strong sideward “kick” to the nucleons in the participant zone. The early literature often used the alternative name sideward flow.

Directed flow is sensitive to details of the collision process during the passage time of the two nuclei, $2R/\gamma \sim 0.1 \text{ fm}/c$ [38, 39], where R is the nuclear radius and γ is the usual relativistic factor. Therefore, directed flow is especially suitable for probing the collision process at very early times. The magnitude of the deflection can reveal information on the compressibility of the matter in the overlap region. In a fixed-target nucleus-nucleus collision, positive v_1 is defined as the direction of projectile spectator fragments, which always undergo repulsive scattering in the reaction plane at relativistic energies. The same convention is used in collider experiments for historical reasons.

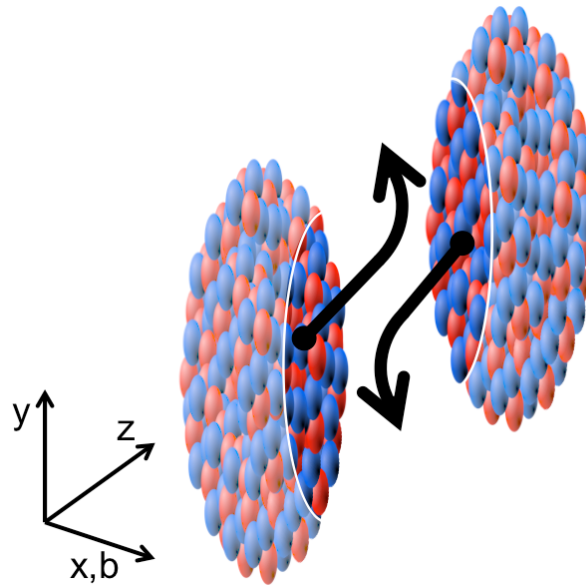


Figure 2.3: Schematic cartoon of Directed flow.

2.1.3.2 Elliptic Flow

Elliptic flow, $v_2 = \langle \cos 2(\phi_i - \Psi) \rangle$, is the second harmonic in the Fourier expansion of the azimuthal distribution relative to the reaction plane. If the observed $v_2 > 0$, then it is in-

plane elliptic flow (parallel to the reaction plane) and if $v_2 < 0$, then it is out-of-plane elliptic flow (perpendicular to the reaction plane). Elliptic flow has the same sign on both sides of midrapidity ($y = 0$), unlike directed flow. Hydrodynamic calculations indicate that in-plane elliptic flow develops at the same time as the system becomes thermalized, and it is a signature of collective expansion of the dense and excited matter formed in heavy-ion collisions. The elliptic flow tends to increase in magnitude as the beam energy increases in the RHIC energy region.

2.1.3.3 Higher Harmonics

Higher harmonics of anisotropic flow can offer more insights into the structure of the azimuthal anisotropy. The third harmonic, v_3 , is called triangular flow. In the first couple of decades of the study of v_1 and v_2 , it was assumed that symmetry properties always required $v_3 = 0$. Then in 2010, it was pointed out that initial-state geometry fluctuations were large enough to cause a measurable v_3 signal, and such fluctuations are of considerable physics interest and importance [40]. Similarly, harmonics four (v_4) and six (v_6) can provide further details about the shape of the azimuthal anisotropy.

2.2 Directed Flow and a Possible First-Order Phase Transition

If an equation of state has a point where the ratio of pressure to energy density (P/ε) has a local minimum, this minimum is known as a “softest point”. For certain conditions, model calculations predict a softening of the equation of state near the QGP-hadron phase boundary, and in several papers, possible evidence for a first-order phase transition is presented and discussed [8, 9, 41–43]. The quasi-particle models suggest that for $\mu_B = 0$, the softest point is not pronounced, but inclusion of a first-order phase transition shows a pronounced softest point at larger μ_B [44, 45]. Also, lattice QCD calculations indicate that at top RHIC energies ($\sqrt{s_{NN}} = 200$ GeV, $\mu_B \sim 0$), the transition from QGP to hadron gas is a smooth crossover [3–

7]. At lower energies, lattice QCD and other models suggest that the phase transition becomes discontinuous, implying a first-order phase transition [8, 9] between QGP and hadronic gas.

Publications dating from 1995-2005 based on hydrodynamic models around $\sqrt{s_{NN}}$ of a few GeV predict a minimum in baryon directed flow, possibly involving a double sign-change in directed flow for net baryons, as a function of $\sqrt{s_{NN}}$ [43, 45]. This phenomenon was proposed to be a signature of a first-order phase transition between QGP and the hadron gas phase [43, 45]. Negative directed flow slope near midrapidity is called “anti-flow” [46] or “third flow component” [47] or “wiggle” [39, 43, 48]. Hydrodynamical calculations with a QGP equation of state show negative dv_1/dy slope for nucleons [46, 47], and it has been argued that such a signal, if observed for baryons, would be a QGP signature [43]. Near midrapidity, pions also show negative dv_1/dy [49], but this is attributed to shadowing by nucleons [50]. Negative dv_1/dy at sufficiently high energies in microscopic hadronic transport models can be explained as a geometric effect [48, 51, 52]. In a purely hadronic system, the expansion of a highly compressed source in the shape of a tilted disk can give rise to a wiggle structure. For the beam energies produced by the Brookhaven AGS fixed-target accelerator and below, where it is believed that the energy is too low to produce a QGP, dv_1/dy is positive at all rapidities, in both models and experiment.

There is a good deal of detailed information present in the rapidity dependence of directed flow $v_1(y)$ over the one to two units of y where STAR has acceptance. In order to reduce these details to a single number that reflects the overall strength of the directed flow signal, the slope dv_1/dy , averaged over $y < 0.8$, is chosen to quantify this strength.

2.3 Selected Directed Flow Results

In this section, I review experimental and theoretical aspects of directed flow related to the QGP-hadron gas phase transition.

2.3.1 Experimental Measurements

2.3.1.1 NA49

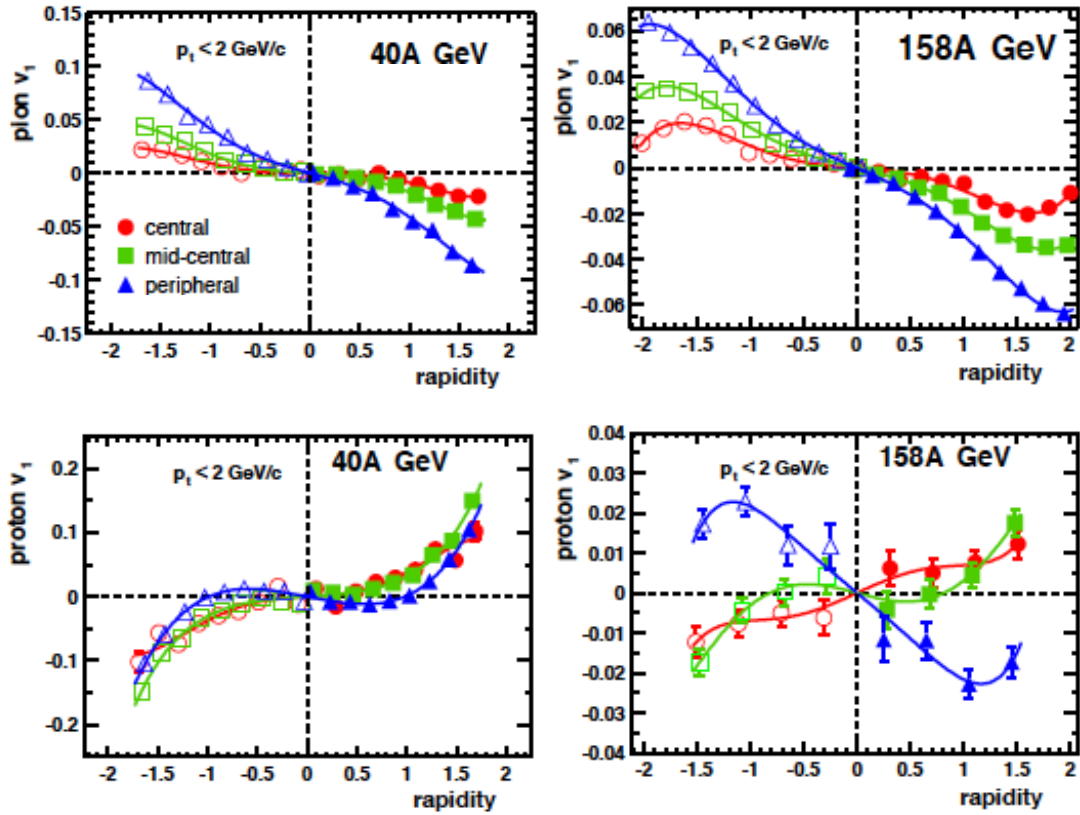


Figure 2.4: Directed flow of protons and charged pions as a function of rapidity for 40A and 158A GeV Pb+Pb collisions. Data points are mirrored at negative rapidity. This figure is reproduced from Ref. [53] published by the NA49 collaboration at CERN. Note that fixed-target experiments normally give the kinetic energy of the beam ions per nucleon in the laboratory frame, which is not the same convention as $\sqrt{s_{NN}}$ defined earlier.

The NA49 energy scan experiment at the CERN SPS fixed-target accelerator took data during 1994-2002. Figure 2.4 shows proton and charged pion v_1 in three centrality classes for 40A and 158A GeV Pb+Pb collisions [53]. Charged pion v_1 shows similar magnitude near midrapidity for both energies. Proton v_1 near midrapidity is small in magnitude, but increases steeply towards the projectile and target rapidity region. Near midrapidity at 40A GeV, protons show the first signs of antiproton flow. At 40A GeV, protons have opposite slope dv_1/dy compared to pions.

At $158A$ GeV protons show hints of opposite slope dv_1/dy compared to pions in central and mid-central collisions, but error bars are too large to make a conclusive statement. A hadronic model with a momentum-dependent mean field shows better agreement with NA49 data than without the mean field [54], but does not show negative slope dv_1/dy .

2.3.1.2 AGS-E895

The E895 energy scan experiment at the AGS fixed-target accelerator at Brookhaven National Lab took data in 1995 and 1996 for 2, 4, 6 and $8A$ GeV Au+Au collisions. Figure 2.5 shows the slope of proton directed flow ($p_x \sim v_1 p_T$) for beam energies 2, 4, 6 and $8A$ GeV [55]. Proton directed flow shows positive slope for all E895 energies, and the slope significantly decreases with increasing beam energy. Extrapolations of the results are consistent between E895 [56] energies and maximum AGS energy in the E877 experiment at $11.5A$ GeV [57]. Similar to NA49 data, a hadronic model with a momentum-dependent mean field shows better agreement with E895 measurements [54]. A hydrodynamic model [43] predicted that the softest point would lie at AGS energies, but E895 did not find any dip in proton directed flow.

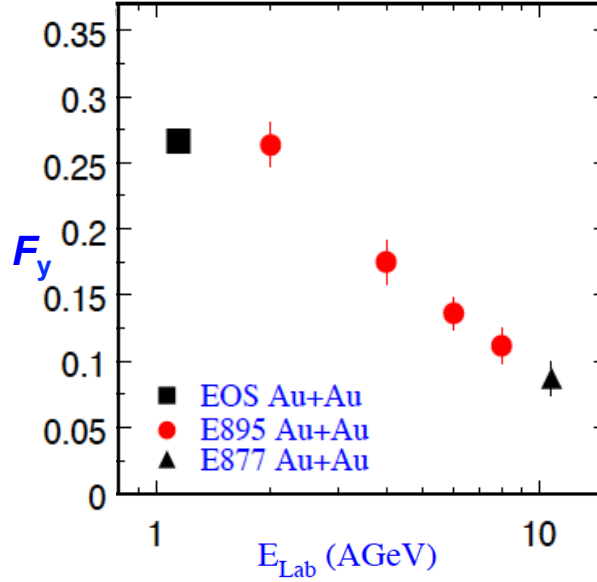


Figure 2.5: Beam energy dependence of the slope of $\langle p_x(y) \rangle$ for 1.2, 2, 4, 6, 8 and 11.5A GeV Au+Au fixed-target collisions. The linear term F in a cubical fit function, $Fy + Cy^3$, is used to extract the slope. This analysis is based on normalized rapidity, where the projectile and target are always at ± 1 by definition. This figure is reproduced from Ref. [55].

Figure 2.6 shows Λ directed flow results from the E895 collaboration. The left side shows $\langle p_x(y) \rangle$ for both Λ and proton, where both particles have a similar trend. The magnitude of $\langle p_x(y) \rangle$ for Λ s always lies below the same for protons. The right side of Figure 2.6, top panel, shows a linear fit of “Flow” = $d\langle p_x \rangle / dy$ to the data near midrapidity. According to the quark counting rule [58], Λ s interact through non-strange quark constituents, and therefore the ratio of “Flow” for Λ relative to proton is expected to be $\sim 2/3$. The right side of Figure 2.6, bottom panel, shows this ratio to be consistent with $2/3$ at 2A GeV, but deviates significantly at 4 and 6A GeV.

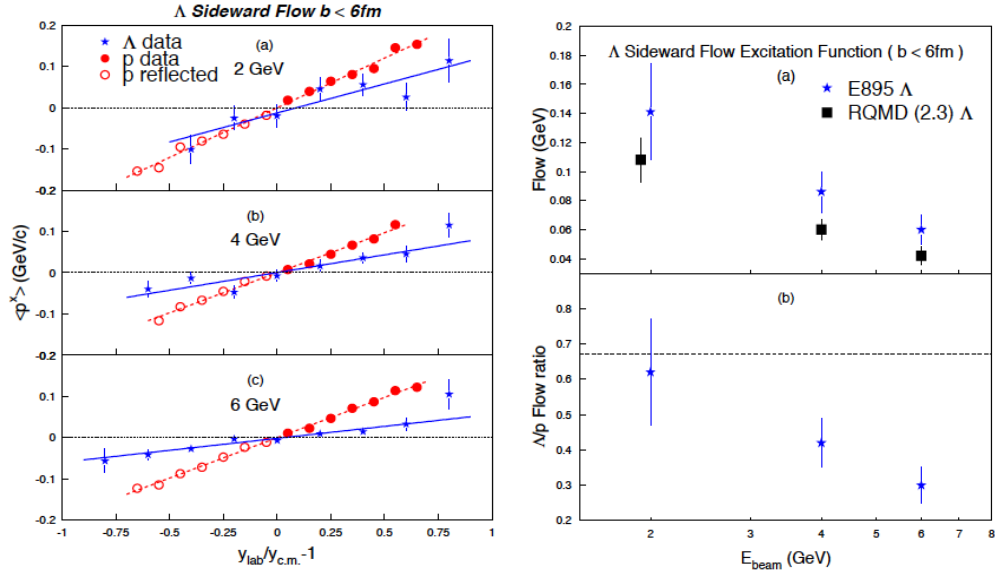


Figure 2.6: The left side shows an older definition of directed flow (average p_x) for protons and Λ s as a function of normalized center of mass rapidity in 2, 4, 6 and 8 A GeV Au+Au fixed-target collisions. The open circles shows reflected data points. On the right side, panel (a) shows the slope of $\langle p_x(y) \rangle$ as a function of beam energy using a linear fit. Panel (b) shows this slope, in the form of a ratio for Λ over proton, as a function of beam energy. This figure is reproduced from Ref. [59].

2.3.1.3 STAR-BES Phase-I

Figure 2.7 shows the beam energy dependence of the slope dv_1/dy near mid-rapidity for protons, antiprotons and charged pions from the STAR experiment [49]. The slope is the linear term in the cubic fit function $v_1(y) = Fy + Cy^3$ for intermediate centrality (10-40%) Au+Au collisions. The proton slope decreases with increasing energy, reaches a minimum between 11.5 GeV and 19.6 GeV, and then remains negative and small. The STAR results show good agreement with NA49 measurements [53] and are consistent with smooth extrapolations down to E895 energies [55]. Charged pion and antiproton v_1 shows negative slope for all the measured energies. The minimum seen in the data for protons lies at a higher beam energy than the 2005 hydrodynamic prediction from the Frankfurt group [43].

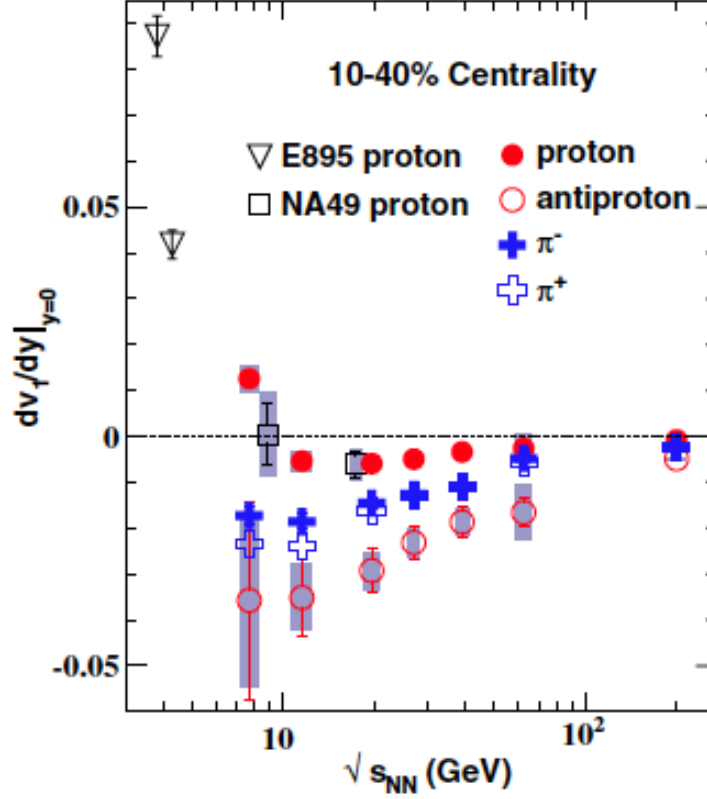


Figure 2.7: Directed flow slope, dv_1/dy , near midrapidity for 7.7, 11.5, 19.6, 27, 39, 62.4 and 200 GeV 10-40% central Au+Au collisions for protons, antiprotons and π^\pm . Measurements from NA49 [53] and E895 [55] with comparable but not identical cuts are also plotted. This figure is reproduced from Ref. [49].

2.3.2 Models With Relevance to Directed Flow

2.3.2.1 Hadronic Transport Model (UrQMD)

The UrQMD (Ultrarelativistic Quantum Molecular Dynamics) [60, 61] model is a microscopic transport model for Monte Carlo simulation of $p + p$, $p + \text{nucleus}$ and $\text{nucleus} + \text{nucleus}$ collisions. In UrQMD, and in other similar microscopic transport models, the full space-time evolution of all partons and produced particles is calculated from the initial state to the final freeze-out. Even though UrQMD implicitly assumes a hadronic phase of matter throughout the collision process, and does not include a QGP phase, the fact that it models the space-time evolution of all partons and particles still offers insights into QGP signatures.

Panels (a) and (b) of figure 2.8 show the slope of directed flow from the UrQMD model at RHIC BES energies [49] for antiprotons and protons, respectively. For antiprotons, UrQMD shows qualitative agreement with STAR data at higher energies, but strongly deviates at lower energies. For protons, the UrQMD model shows a sign change, but at much higher energy than what STAR has measured, and UrQMD does not have a minimum (a possible softest point) like the data. Overall, the UrQMD model does not reproduce the non-monotonic behavior of protons measured at STAR in the range $\sqrt{s_{NN}} = 7.7$ to 200 GeV and qualitatively differs from STAR measurements.

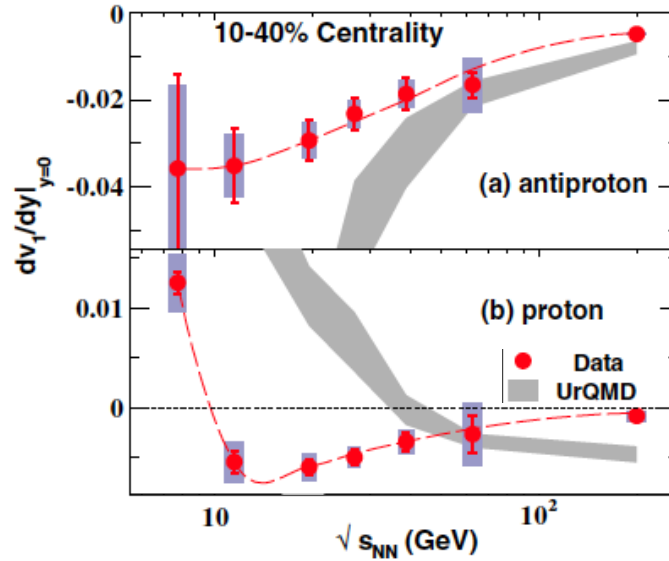


Figure 2.8: Directed flow from the UrQMD model, compared with STAR BES measurements.

2.3.2.2 Ideal Hydrodynamics with Isochronous Freeze-Out

In an ideal three-fluid hydrodynamic model with isochronous freeze-out [62], a sharp dip, including a double sign change, is predicted in the directed flow — an effect termed “softest point collapse” [43]. This prediction only happens for an EOS that features a first-order phase transition. The predicted position of the minimum is at $\sqrt{s_{NN}} \sim 4$ GeV. The qualitatively similar signal measured by STAR has a much smaller magnitude of directed flow at all energies (not

easily seen from this plot, due to the fact that the standard v_1 observable is not used), and the minimum measured by STAR occurs at a higher beam energy [49].

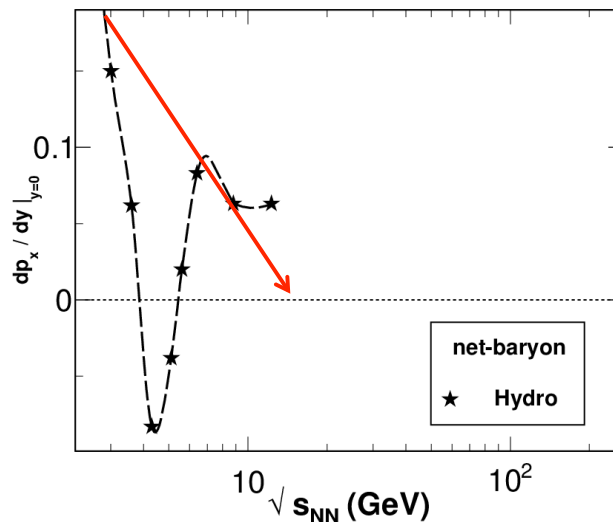


Figure 2.9: Ideal three-fluid hydrodynamic calculation of directed flow for net baryons from Au+Au collisions at intermediate centrality. Star markers correspond to EOS with the assumption of a first-order phase transition. The red arrow indicates the trend of directed flow assuming an EOS without a phase transition. This figure is based on calculations reported in Ref. [43].

2.3.2.3 Frankfurt Hybrid Model

Hydrodynamic models have been remarkably successful in describing many aspects of heavy-ion collisions, even though there are strong reasons to doubt the basic hydro assumption that the medium throughout the interaction can be described by fluid cells in at least local thermal equilibrium. In the hybrid approach of the Frankfurt group, the initial stage before equilibrium, and the later stages when the QGP phase has ended and hadronic scattering, decays and freeze-out occur, are both modeled by a microscopic Boltzmann transport code. Thus, fluid dynamics is used only for the intermediate high-density stage when EOS effects are most important, and the assumption of local equilibrium is justified.

Figure 2.10 shows proton directed flow results from this hybrid approach, and for comparison, two cases of “pure” hydrodynamics are also plotted. The blue triangles are pure hydro

with isochronous (IC) freeze-out, while the red circles are pure hydro with freeze-out at constant energy density (IE), which is considered to be more realistic than the IC assumption [63]. The black square markers show the hybrid calculation, while the experimental measurements are in green. It is important to note that the vertical scale on this plot is about two orders of magnitude wider than figure 2.8, and therefore the STAR points are all consistent with zero in this plot, and the STAR error bars are vastly smaller than the plotted marker size. One conclusion from these model comparisons is that pure hydro, both IC and IE, as well as the hybrid model, all predict a directed flow signal for protons that is far too large. Furthermore, only the unrealistic IC case of pure hydro predicts a pattern of directed flow that is qualitatively similar to experiment. Another noteworthy conclusion is that pion directed flow from the hybrid model, which unlike baryons is not very sensitive to the QCD equation of state, shows better agreement with experimental measurements.

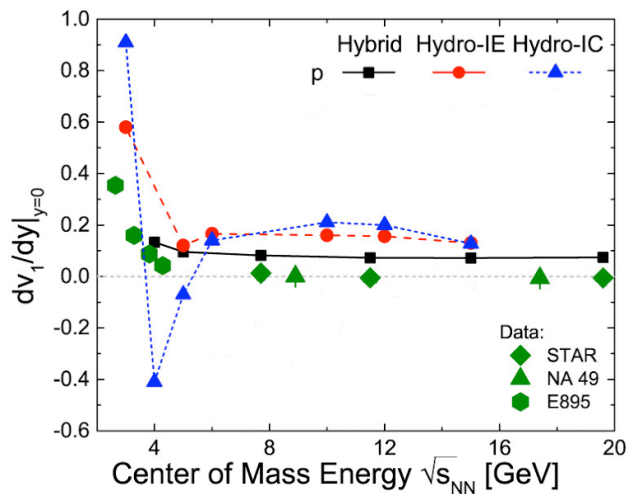


Figure 2.10: Proton v_1 slope from the hybrid model, and from the hybrid code with Boltzmann transport turned off, in order to show two cases of pure hydrodynamics. Experimental results are shown as green markers. This figure is reproduced from Ref. [63].

2.3.2.4 Parton-Hadron-String Dynamics Model

Parton-Hadron-String Dynamics (PHSD) is a microscopic off-shell transport approach, which addresses partonic degrees of freedom. The PHSD model includes initial hard scatterings and

string formation through a dynamical deconfinement phase transition to quark-gluon plasma. In the calculations reported so far, only a crossover transition between hadron gas and QGP is implemented. The model completes the full evolution of the heavy-ion collision by describing hadronization and the subsequent interactions in the hadron gas phase. The PHSD code has a mode of operation called Hadron-String Dynamics (HSD) which is purely hadronic, with no QGP. Below a critical energy density ($\sim 0.5 \text{ GeV}/\text{fm}^3$), PHSD always operates in HSD mode.

The slope of v_1 is shown in Figure 2.11 for protons, antiprotons and π^- in intermediate-centrality Au+Au collisions, with experimental results also plotted. The proton slope in the model qualitatively resembles trend of data at lower energies, but shows larger values, and the sign change in the model occurs at a higher beam energy. For antiprotons, PHSD/HSD qualitatively resembles experimental data, but strongly deviates at the lowest energies. Negative pions from the model show good agreement with experiment above 11.5 GeV. Overall, the larger deviations at lower beam energies demonstrate that heavy-ion dynamics is not yet understood within the parton-string/hadron picture under these conditions.

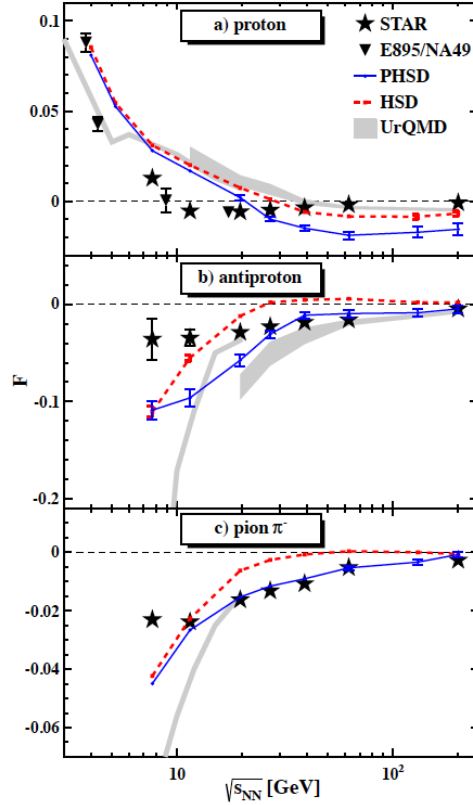


Figure 2.11: Directed flow slope $F = dv_1/dy$ near midrapidity as a function of beam energy for protons, antiprotons, and π^- in intermediate-centrality Au+Au collisions. Experimental measurements from STAR [49], NA49 [53], and E895 [55] are also shown. Shaded bands show UrQMD results from Ref. [49]. This figure is reproduced from Ref. [64].

2.3.2.5 Jet AA Microscopic (JAM) Transport Model

In this latest theoretical calculation, a microscopic transport model JAM [65] is modified so that the standard stochastic two-body scattering does not contribute to generating pressure in the system. The same idea was used two decades ago to model directed flow at much lower energies [66]. Pressure in a two-body system is enhanced with a repulsive potential and suppressed with an attractive potential, and thus attractive potentials simulate a softening of the EOS [67]. In Ref. [68], the JAM model is modified by requiring an attractive potential for each two-body scattering to represent the effect of a softening of the EoS. Figure 2.12 compares STAR data [49] with the standard and modified JAM models. For protons, the standard

JAM model agrees with experiment at 7.7 GeV, but shows much larger v_1 at 11.5 and 19.6 GeV. At 27 GeV, standard JAM shows negative slope and comes back into reasonable qualitative agreement with data, but the negative slope at this energy is due to geometric reasons. The attractive JAM model strongly deviates from STAR data at 7.7 GeV, but shows reasonable qualitative agreement above 10 GeV. The authors of Ref. [68] conclude that their findings “strongly support the conclusion that the minimum of dv_1/dy is a result of the softening of the EoS which may be caused by the first-order phase transition”.

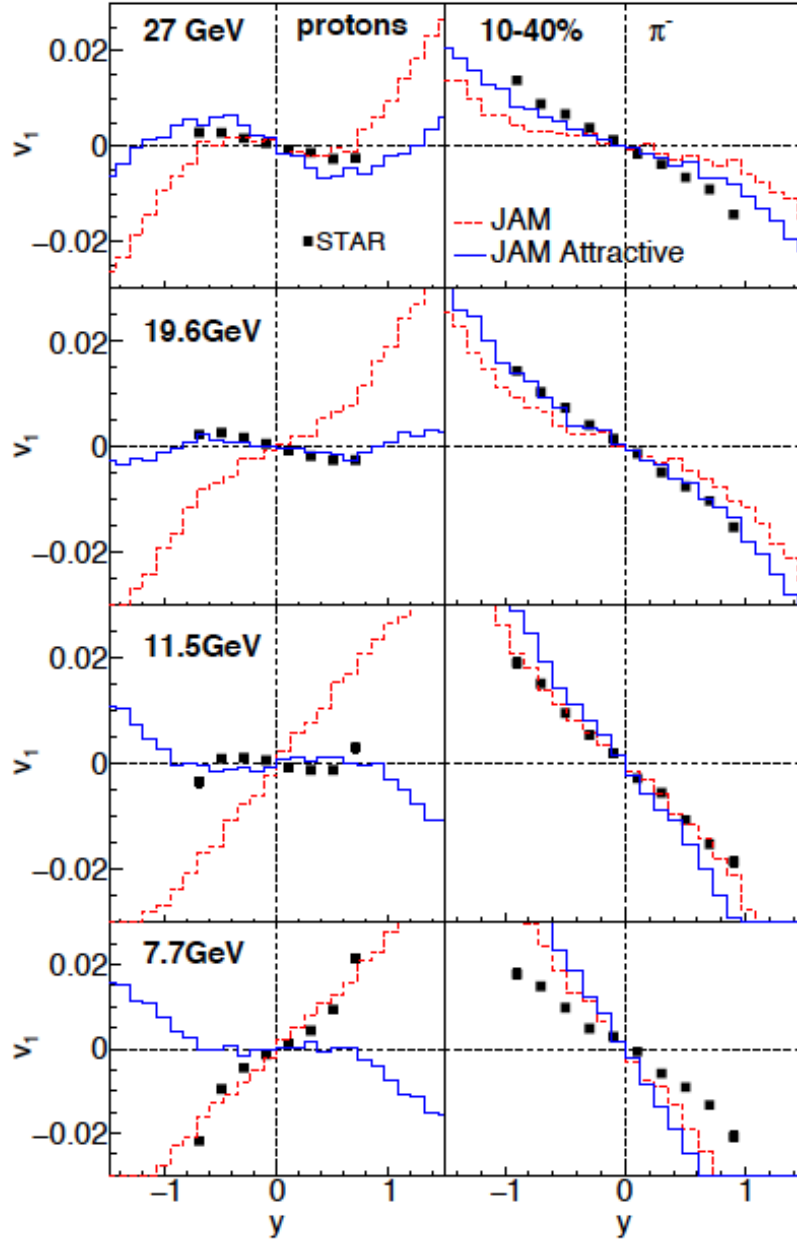


Figure 2.12: Proton and π^- directed flow in 10-40% central Au+Au collisions at $\sqrt{s_{NN}} = 7.7 - 27$ GeV. Standard JAM and attractive JAM models are compared with STAR measurements [49]. This figure is reproduced from Ref. [68].

CHAPTER 3

EXPERIMENTAL SETUP

Data used in this dissertation were collected by the STAR (Solenoidal Tracker at RHIC) experiment at the Relativistic Heavy Ion Collider (RHIC) facility. This chapter describes the operation of RHIC, of the STAR experiment, and of the subsystems at STAR which are primarily used for the analysis in this dissertation.

3.1 The Relativistic Heavy Ion Collider

The Relativistic Heavy-Ion Collider (RHIC) at Brookhaven National Laboratory (BNL) is the first of its kind in heavy-ion physics and the only spin-polarized proton collider in the world. At RHIC, the accelerated particle species range from protons to uranium nuclei, and they can be accelerated to nearly 99.995% of the speed of the light — 100 GeV per nucleon in each of the two beams. The current Au+Au average luminosity is about $5 \times 10^{27} \text{ cm}^{-2}\text{s}^{-1}$. RHIC can collide non-symmetric particle pairs, such as p +Au and d +Au. In this section, I explain the acceleration arrangement for colliding gold + gold ions. For other species of ion, the details might be slightly different.

Figure 3.1 shows the acceleration scheme for gold ions at RHIC. The Electron Beam Ion Source (EBIS) facility combines a modern ion source and linear pre-accelerator, supplying a range of possible ion species at a kinetic energy of 2 MeV per nucleon. Gold ions from EBIS, which are typically in a +32 charge state, are then injected into a Booster Synchrotron. When the ions exit this Booster Synchrotron, their energy is raised to ~ 100 MeV per nucleon. Next, the beam passes through a thin stripper foil, which provides a good yield of gold ions in the

+77 charge state. Then ions are transferred to the Alternating Gradient Synchrotron (AGS), a machine which has been in continuous operation in a variety of modes since 1960. Gold ions are accelerated to 9.8 GeV per nucleon in the AGS, and are fully stripped at the exit of this machine. The AGS delivers beam to RHIC for the final phase of acceleration. The RHIC accelerator consist of two quasi-circular side-by-side rings which are 3.8 km in circumference. Each of the two rings of RHIC is capable of accelerating ions up to 100 GeV per nucleon and spin-polarized protons up to 250 GeV. In addition, the RHIC rings can decelerate ions when lower energies are needed for scanning a range of collision energies. The accelerated or decelerated beams can be stored in RHIC for periods up to several hours without needing further injection from the AGS. The clockwise ring of RHIC (viewed from above) is called the 'blue ring' and the counter-clockwise ring is called the 'yellow ring'. These rings intersect at six locations, and the beams can be steered either to maximize the collision rate at any given intersection region (IR) or to dial-in any desired lower rate. At four of these IRs, experiments BRAHMS, PHOBOS, PHENIX and STAR are located. An overview of all experiments in RHIC can be found in Ref. [69]. One of the remaining IRs is used for the RHIC radio frequency system. The BRAHMS experiment [70] was build for momentum spectroscopy studies in a narrow solid angle, and completed data-taking in 2006. The PHOBOS experiment [71] had the largest pseudorapidity coverage but limited particle identification, and was designed for bulk particle measurements. It completed data-taking in 2005. PHENIX [72] is designed for measuring rare hard probes such as electrons, muons and photons, to study the medium formed in heavy-ion and proton-proton collisions, and is still in operation. The STAR [73] experiment is at the core of this dissertation research, and is described in the next subsection.

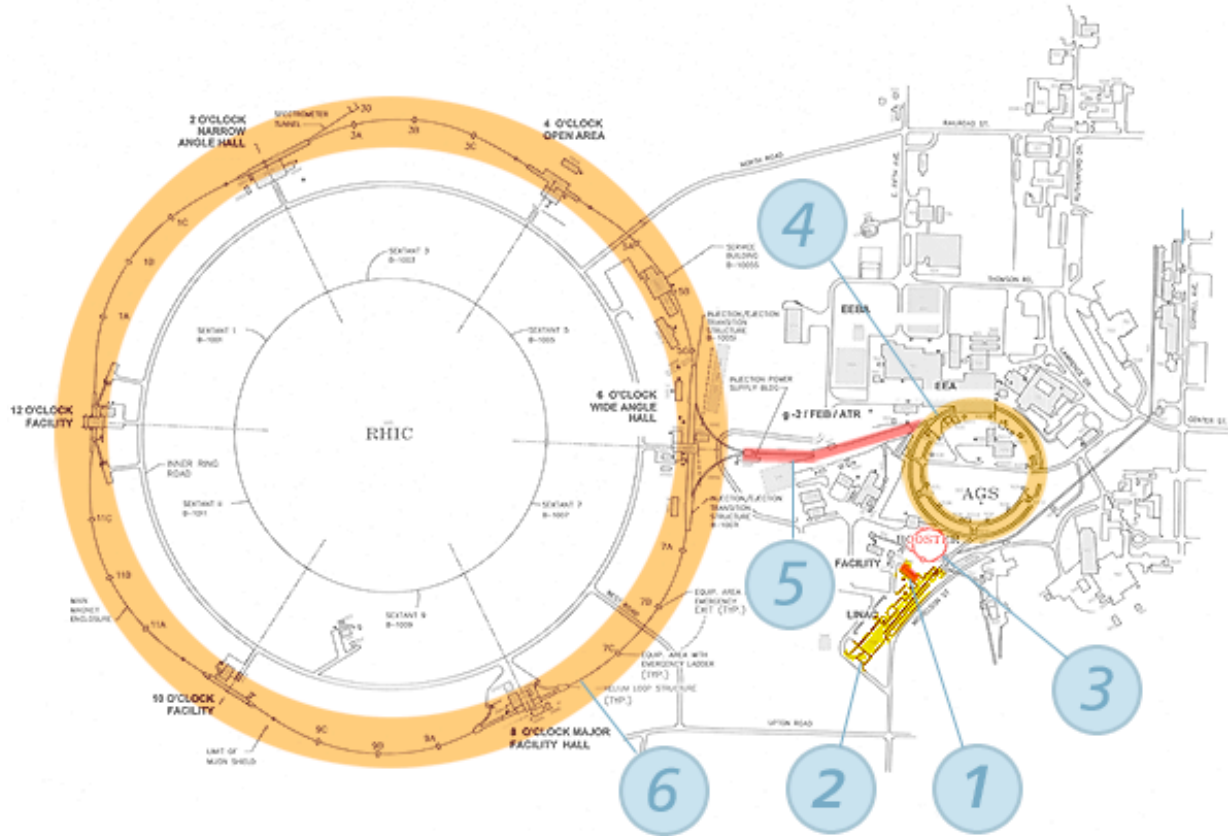


Figure 3.1: The gold ion acceleration scheme at RHIC. In the figure (1)–EBIS, (2)–Linac, (3)–Booster, (4)–AGS, (5)–AGS to RHIC transfer line, (6)–RHIC rings. This figure is reproduced from Ref. [74].

3.2 The STAR Experiment

The Solenoidal Tracker At RHIC (STAR) is located at the six o'clock (most southerly) position of the RHIC ring. A room-temperature solenoidal magnet can be used at its full field, 0.5 T, or at half-field, 0.25 T. The magnet weighs 1100 tons and consumes 3.5 MW at full field. The magnetic field is parallel to the beam, and its main purpose is for momentum measurements. The z axis lies along the beam and points to the east side of the detector. The y axis points vertically up. Figure 3.2 shows the principal subsystems of the STAR experiment. Some of the subsystems at STAR are geared to a specific area of physics analysis. This chapter describes only the subsystems that have relevance for this dissertation study.

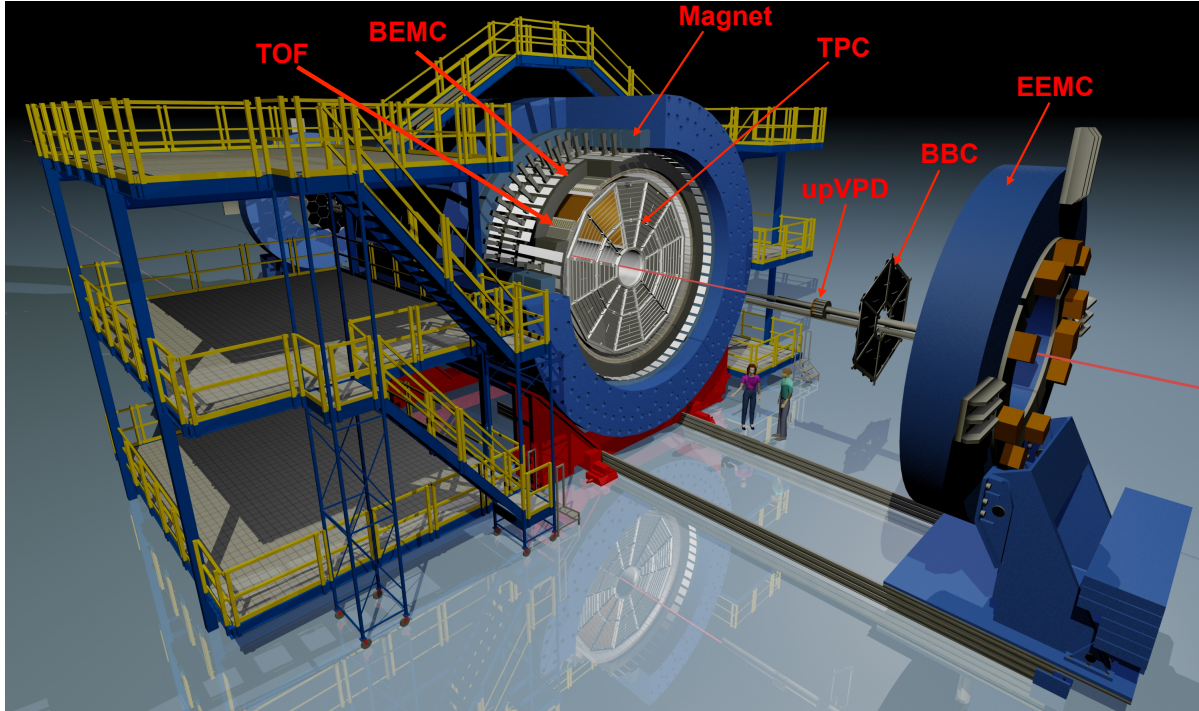


Figure 3.2: Diagram of the STAR experiment and some of its subsystems. The end-cap electromagnetic calorimeter (EEMC) is pulled back in this diagram, allowing more of the internal details of STAR to be viewed.

3.2.1 The Time Projection Chamber

The Time Projection Chamber (TPC) is the core detector for the STAR experiment, and plays an essential role in every analysis. This gas-filled tracking chamber is 4.2 m long and 4 m in diameter, and is installed inside the STAR magnet. The STAR TPC has full 2π acceptance in azimuth, and has full tracking capability for particles emitted at a polar angle $45^\circ < \theta < 135^\circ$ relative to the z axis. In terms of rapidity, the acceptance is roughly ± 1.1 units. Online software can reconstruct more than 3000 tracks per event in real time. In addition to tracking, the TPC also measures ionization energy loss for charged particle identification.

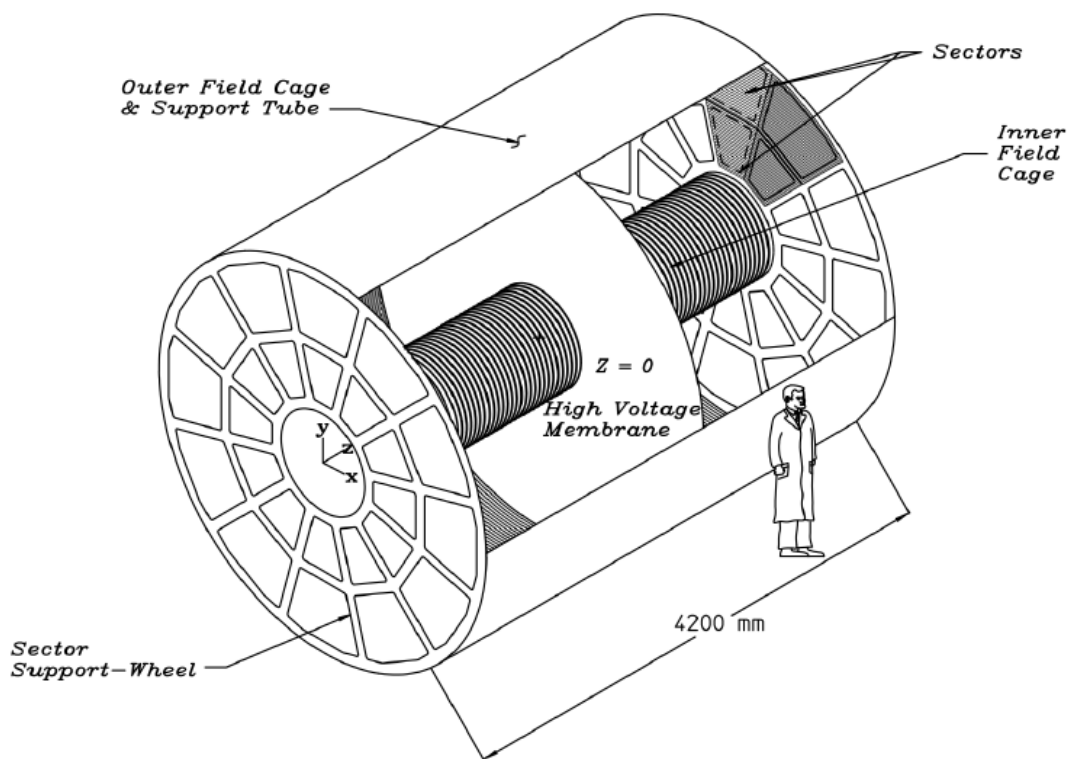


Figure 3.3: The STAR Time Projection Chamber (TPC). This figure is reproduced from Ref. [75].

Figure 3.3 shows a schematic view of the STAR TPC. The central high voltage membrane (cathode) is operated at 28 kV. The endcaps are grounded Multi-Wire Proportional Chambers (MWPC). The voltage gradient between anode and cathode creates an axial electric field of ~ 135 V/cm. The inner and outer field cages are a series of conductive rings on a kapton cylinder, separated by resistors that provide an equipotential surface to ensure that the axial electric field is uniform. The chamber is filled with P10 gas which is composed of 90% argon and 10% methane. The gas pressure is regulated at about 2 millibar above atmospheric pressure [76]. This pressure differential is optimum for minimizing leaking of the gas and suppresses contamination from atmospheric oxygen. The P10 gas and electric field strength are chosen so that important characteristics of the chamber, like ionization drift velocity, are not sensitive to small variations in atmospheric pressure and temperature. Charged particles passing through the chamber ionize the gas. Electrons from the ionization drift towards the

endcaps at a constant velocity of $\sim 5.5 \text{ cm}/\mu\text{s}$, resulting in a maximum drift time of $\sim 40 \mu\text{s}$. Every couple of hours during normal operation, the drift velocity and various small spatial distortions are monitored and calibrated via a laser system that sends about 500 UV beams throughout the chamber [77].

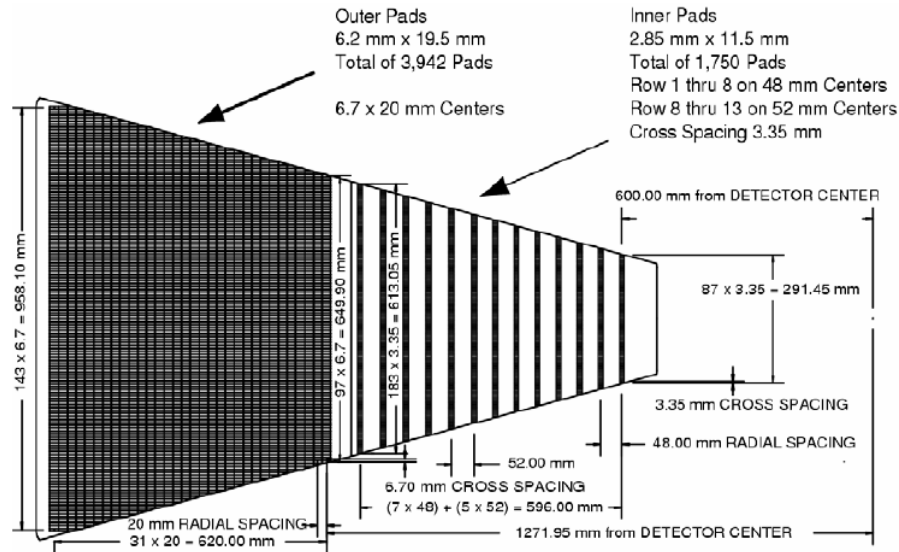


Figure 3.4: One of the TPC pad plane sectors. This figure is reproduced from Ref. [75].

An important part of the endcap MWPCs is the read-out plane, comprised of rectangular copper pads. Above the pad plane, there are three planes of wires: an anode grid, a ground grid and a gating grid. The pad planes and wire grids are located at each endcap of the TPC, and each endcap is made up of 12 inner and 12 outer sectors. Figure 3.4 shows the TPC pad plane geometry for an outer and inner sector. The outer and inner pad planes have a different arrangement of pads, in order to optimize track reconstruction for a fixed investment in readout electronics. Continuous pad coverage is chosen for the outer subsector, in order to achieve the best resolution for each track's ionization energy loss per unit distance (dE/dx), based on the magnitude of the pad signals. The inner sectors encounter higher track density than the outer sectors, and therefore the inner pads are optimized for better two-track resolution. The inner sectors use smaller pads than the outer sectors, and there are gaps between pad rows only

in the inner sectors. The latter arrangement improves momentum resolution but marginally compromises the dE/dx resolution.

The anode wires, located just above the pad plane, are responsible for amplification of drift electrons from primary ionization. The anode wires of the inner and outer sectors are typically held at 1170 V and 1390 V, respectively, resulting in a gas gain of one to three thousand. Each electron avalanche creates a temporary image charge on the pads. When a track crosses a row of pads, the induced image charge is usually detectable on two or more pads in that row, thus allowing the position along the row to be determined with better resolution than would be possible if only one pad gave a signal.

The next wire plane is a grounded grid which terminates the drift field region for primary ionization, and provides RF shielding for the pad plane. When driven by a pulser, this plane is also used to calibrate the pad plane electronics.

The topmost wire plane above the pads is the gating grid. The gating grid controls the the passage of ionization between the drift region of the TPC and the MWPC amplification region. It is normally in the closed configuration, and is opened only when a desired event is to be read out. When closed, it blocks drift electrons from entering the MWPC, and also blocks positive ions produced in the MWPC from entering drift region where they could distort the drift field. Positive ions are slow to escape during the open time, and are neutralized when the gate is closed. When the gating grid is open, all wires are at -110 V, and when closed, adjacent wires are set to ± 75 V. A detailed description of the operation of the TPC can be found in Ref. [75].

The outer pad plane sectors consist of 32 pad rows, and the inner sectors consist of 12 pad rows. This allows a charged particle to have up to 45 coordinates in the xy plane. Together with the z coordinate derived from the drift time of ionization electrons, space points for each track in the TPC can be calculated in three dimensions. The track momentum vectors and the sign of the track's electric charge are obtained from the helical path of the particles in the field of the STAR magnet. Deviations from a helix due to energy loss in the gas are negligible for the tracks of interest in this analysis. The position of the heavy-ion collision vertex is found

by extrapolating the tracks to a point of convergence inside the beam pipe. Figure 3.5 shows TPC tracks for a gold-on-gold event, reconstructed in real time.

Specific particle identification techniques are discussed in Section 4.2.

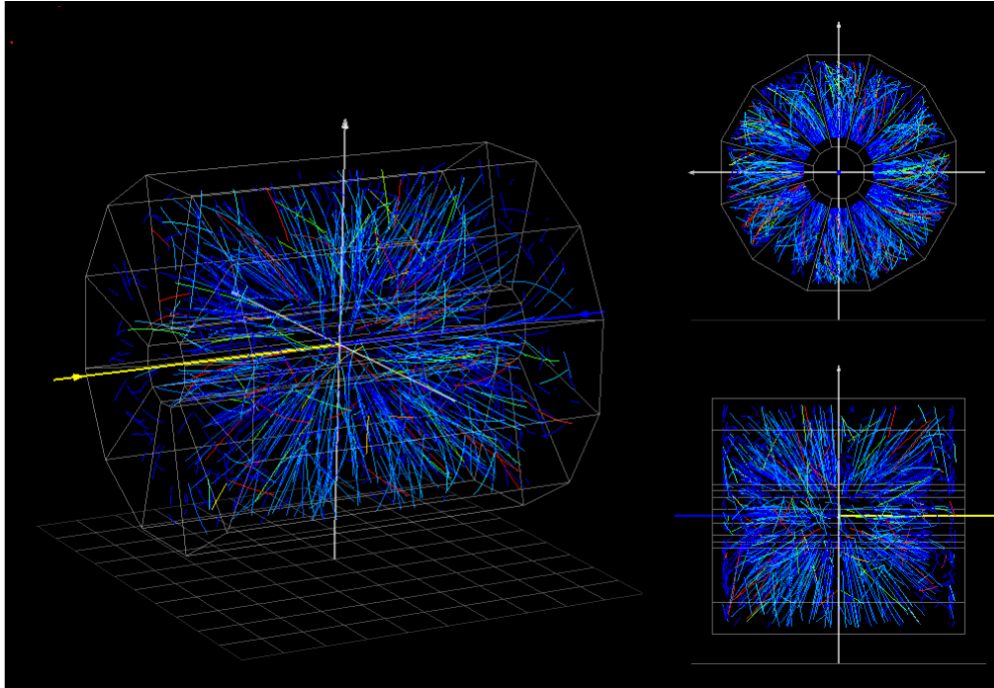


Figure 3.5: Real time event display for a gold+gold event reconstructed in the TPC. When all tracks are projected onto a single plane as in these examples, the density of tracks appears to be very high.

3.2.2 Time of Flight detector

The barrel Time Of Flight (TOF) detector is positioned just outside the TPC detector, and inside the STAR magnet. The TOF covers 360° in azimuthal and $45^\circ < \theta < 135^\circ$ in polar angle relative to the z axis. TOF uses Multigap Resistive Plate Chamber (MRPC) technology to measure the arrival time of particle hits. MRPC modules are filled with 95% 1,1,1,2-Tetrafluoroethane (R-134a) and 5% isobutane. The MRPC has better than 100 picosecond timing resolution and more than 95% detection efficiency for minimum ionizing particles. This performance allows the TOF detector to typically separate pions, kaons and protons up to $\sim 1.8 \text{ GeV}/c$, and sepa-

rate protons from pions and kaons up to $\sim 3 \text{ GeV}/c$. These upper limits are much higher than the limits associated with particle identification from only dE/dx in the TPC.

Figure 3.6 shows a single MRPC module. The TOF barrel is made up of 120 trays covering the full circumference of the barrel, and each tray contains 32 MRPC modules. A detailed description of the TOF-MRPC assembly and operation can be found in Ref. [78–80].

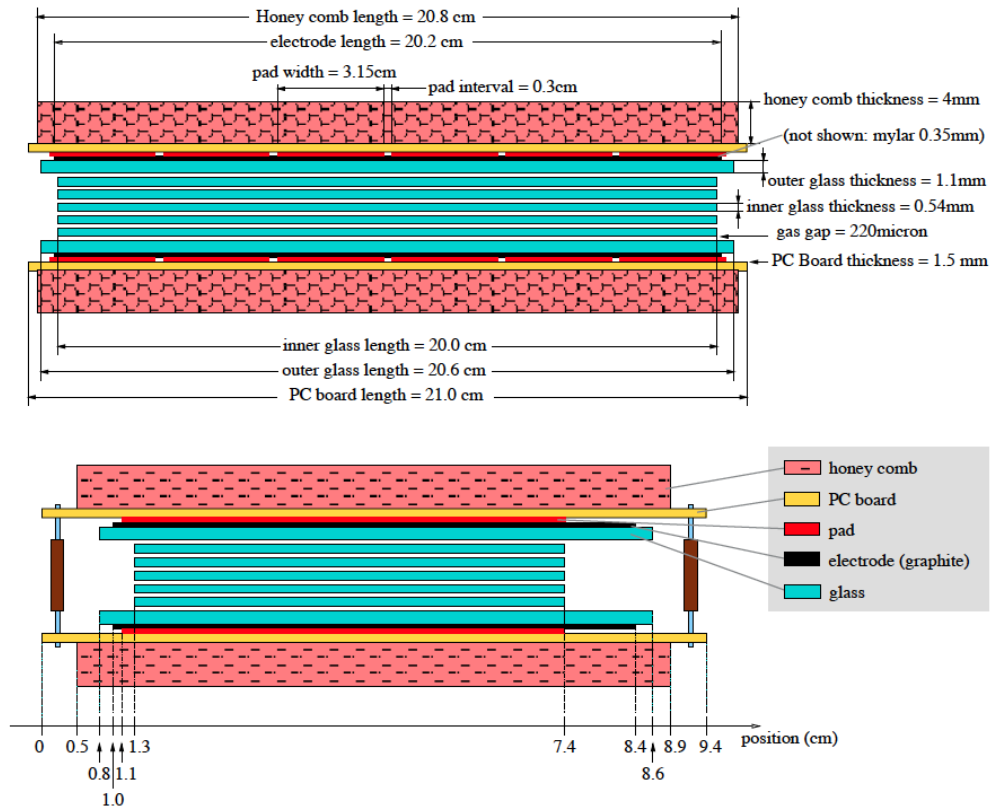


Figure 3.6: Side and end view of a TOF multigap resistive plate chamber (MRPC) module. This figure is reproduced from Ref. [78].

TOF uses the Vertex Position Detector (VPD) [80] to mark the start time of each collision. A VPD module is located on both the east and west sides of the center of STAR, at a distance of 5.6 m along the z axis. Figure 3.7 shows the positions of VPD and TOF detectors, relative to the TPC and the beam pipe. A ~ 24 picosecond timing resolution is obtained from the VPD. The TOF detector measures the end time for track segments, using the synchronized clock signal from the VPD. Below $\sqrt{s_{NN}} = 39 \text{ GeV}$, VPD signals are not reliable, so a modified technique is used, with TOF stop time and start time calculated from clearly identified particles

in both TPC and TOF. Hits in a TOF module are associated with TPC tracks to provide path length (L) and momentum (p) for tracks. Then the mass of the particle is calculated from

$$m = p\sqrt{(\Delta t/L)^2 - 1},$$

where Δt is the time of flight. Specific particle identification techniques for the particles used in this dissertation analysis are described in detail in Section 4.2.

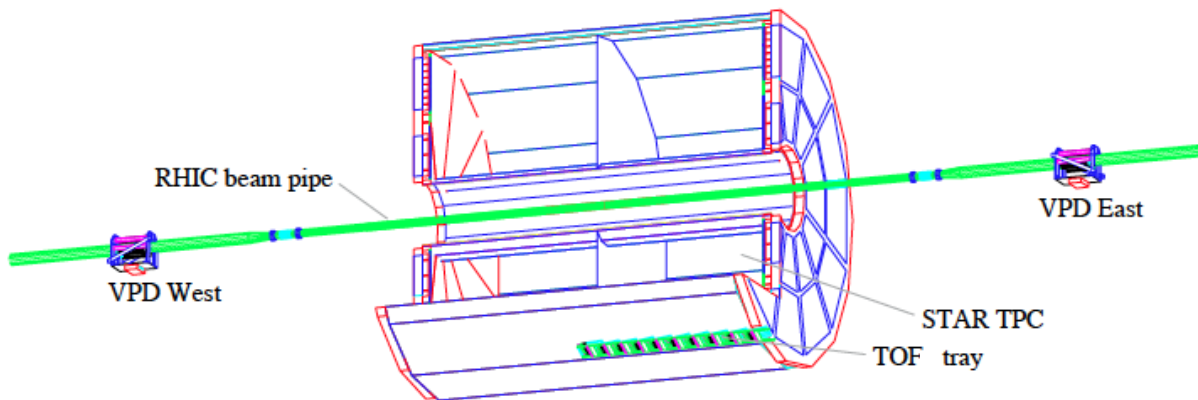


Figure 3.7: Illustration of the relative positions of TPC, VPD and TOF detectors with respect to the beam pipe. A single tray of TOF MRPC modules is indicated. This figure is reproduced from Ref. [80].

3.2.3 Beam Beam Counters

The beam-beam counters (BBC) consist of two arrays of scintillator tiles surrounding the beam pipe, as illustrated in figure 3.8. The two arrays are mounted outside the east and west poletips of the STAR magnet, 3.75 m away from the center of the TPC. Each BBC detector contains two inner rings and two outer rings of hexagonal scintillator tiles, as shown in figure 3.8. The two inner rings, which cover pseudorapidity $3.3 < |\eta| < 5.2$, are a primary tool for most of this dissertation analysis. The BBC is a relatively fast detector, and therefore it is used to trigger events, especially at lower beam energies, and in $p + p$ collisions where there are no spectators. The timing difference between the two BBC modules helps define the location of

CHAPTER 4

ANALYSIS

This chapter describes the analysis techniques used in this dissertation. The first part of this chapter describes the quality assurance selections (cuts) imposed on the available data. Second, centrality selection and event plane estimation are discussed. Third, particle identification techniques are discussed. Finally, I explain the directed flow calculation methods and conclude with systematic uncertainty estimation.

4.1 Data

During the Beam Energy Scan program, the STAR experiment successfully recorded data from Au+Au collisions for center of mass energies ($\sqrt{s_{NN}}$) 7.7, 11.5, 14.5, 19.6, 27 and 39 GeV. The data consist of information about each gold on gold collision (event) and associated trigger information, and about the signals recorded in various detector sub-systems. These data are pre-processed using generic software which identifies the tracks and hence the momentum vectors of the produced particles in each event, and stores this higher level information in so-called microDST files for physics analysis.

4.1.1 Event Selection

When RHIC and its experiments (STAR and PHENIX) are fully functional, data are recorded continuously for typically around twenty weeks per year. During data-taking, events are recorded in files, where each file corresponds to one 'run'. A run can last for as little as a second or two, or as long as many tens of minutes. Due to the extended period of some runs, the conditions

of the beam or the detector setup may deteriorate. For example, a poorly focused beam can cause high background rates, or an important part of a detector might stop working. Runs from such periods are normally flagged and removed. The mean interaction rates, the mean transverse momentum, the mean vertex position, and the mean multiplicity of events are among the quantities monitored closely for the purpose of quality assurance.

After removing bad runs, the good events in each retained run are selected for the analysis using a so-called “minimum-bias” trigger, where minimum bias means that an effort is made to accept all centralities (i.e., all impact parameters), up to and including peripheral collisions. A minimum-bias trigger at BES energies requires a coincidence between the east and west Zero Degree Calorimeters (ZDC), and/or between the east and west Vertex Position Detectors (VPD), and/or between the east and west Beam Beam Counters (BBC). Due to the large beam emittance, especially at lower beam energy, Au ions may sometimes collide with the beam pipe (2.00 cm inner radius at 14.5 GeV and 3.81 cm inner radius at all other beam energies) rather than with another Au ion. To eliminate these events, we require the primary vertex of events to lie within 1 cm from the beam axis at 14.5 GeV, and within 2 cm at the other beam energies. At 14.5 GeV, the beam axis was offset from the center of the beam pipe according to $(x, y) = (0, -0.89)$ cm. The z -position of the vertex was optimized during the data taking using the online High Level Trigger (HLT). Then, from offline studies, z -vertex cuts are applied to ensure the quality of events. This z -vertex cut also ensures that the acceptance for tracks in an event between the east and west sides of detectors is consistent.

The term pileup refers to an event where particles from more than one single collision are recorded in that event. This can happen, for example, if luminosity is high and trigger criteria are loose. Since some tracks belong to a non-triggered event, these tracks do not have valid TOF information. Requiring each event to have at least 5 TOF hits can eliminate these events. In addition, we also require the reconstructed charged particle multiplicity in each events to be greater than 5, and we allow at most 5 primary vertices in an event. To further remove background events, we require 15 or more summed ADC counts in each of the east and

west BBC detectors for 7.7, 11.5 and 19.6 GeV, and at least 75 counts for 14.5, 27, and 39 GeV. After applying these event quality cuts, the available good events for further analysis are summarized in Table 4.1 along with the other beam-energy-dependent cuts and parameters.

Table 4.1: Statistics and energy-dependent cuts and parameters.

$\sqrt{s_{NN}}$ (GeV)	Events (10^6)	Minimum-biase Trigger ID	$ V_z $ (cm)	BBC ADC sum
7.7	4	290001, 290004	70	15
11.5	12	310004, 310014	50	15
14.5	20	440005, 440015	50	75
19.6	36	34000, 340011, 340021	50	15
27	70	360001, 360002	50	75
39	130	280001, 280002	40	75

4.1.2 Centrality Selection

The degree of overlap between the two nuclei in a nucleus-nucleus collision is called centrality, and it is an experimental proxy for the impact parameter (b). Impact parameter, which cannot be measured experimentally, is the distance between the two colliding nuclei at their closest point, assuming the nuclei follow straight-line trajectories. If the two nuclei are fully overlapped ($b = 0$, a head-on collision), this is called a central collision. This type of collision is expected to produce a hotter and denser medium than a peripheral collision, where nuclei only partly overlap. In a central collision, a large particle multiplicity is expected and a larger fraction of the available energy is deposited in the transverse direction. The nucleons in the overlapping region are called participants and these nucleons interact through inelastic collisions. Since the properties of the medium formed after the collision depends not only on the energy of the initial nucleons, but also depends on the centrality, we study the available data in bins of centrality.

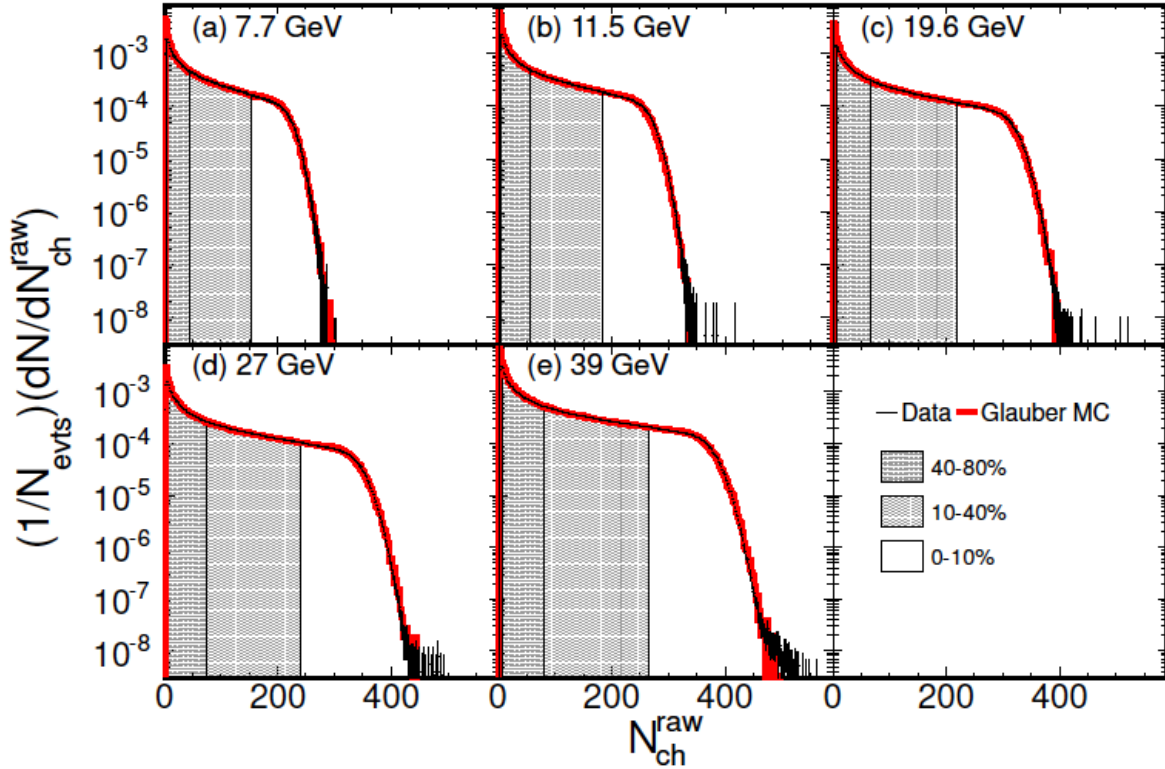


Figure 4.1: Black data points shows normalized $\frac{dN_{\text{events}}}{dN_{\text{ch}}^{\text{raw}}}$ distributions for BES energies. The three shaded bands shows the centrality classes for central (0-10%) intermediate (10-40%) and peripheral (40-80%) collisions. The red histogram shows Monte Carlo Glauber simulations. This figure is reproduced from Ref. [81].

The collision centrality is calculated based on uncorrected charged particle multiplicity distributions, $\frac{dN_{\text{events}}}{dN_{\text{ch}}^{\text{raw}}}$. Reconstructed charged particle multiplicity, $N_{\text{ch}}^{\text{raw}}$ (known as reference multiplicity) is calculated in the TPC for $|\eta| < 0.5$ and track DCA less than 3 cm. The former selection ensures uniform acceptance regardless of the primary vertex position along the z direction, while the latter largely eliminates tracks from weak decay vertices. Another noteworthy factor in relation to $N_{\text{ch}}^{\text{raw}}$ is the TPC reconstruction efficiency. Especially during BES data taking, there were periods when at least one of the TPC sectors was not working, which requires a correction to the reconstructed charged multiplicity (known as corrected reference multiplicity). Since a dead sector only affects one side of the TPC at a time, the reconstructed track efficiency varies with the z -coordinate of a collision vertex. The TPC efficiency is calculated from

the data as a function of the z -coordinate, and raw multiplicity is weighted accordingly. The observed charged particle multiplicity distribution is well described by Glauber Monte Carlo (MC) simulations. Figure 4.1 shows $N_{\text{ch}}^{\text{raw}}$ distributions for BES data and the associated results from Glauber MC simulations with a two-component model [82] fit to the simulated multiplicity distribution.

The biggest disagreement in multiplicity simulations arises due the trigger inefficiency for very peripheral events. Such events have very few tracks and do not provide a reliable event vertex. These inefficiencies are corrected by weighting particle yields by the ratio of simulations to data. Glauber MC calculations and details of fitting the multiplicity distributions are explained in reference [83]. When a MC Glauber fit is available, collision centrality can be determined from the fit to the Cumulative Distribution Function (CDF) for a given reference multiplicity. Table 4.2 shows the reference multiplicity values for BES data in nine centrality bins for the narrowest bin size used in this analysis.

Table 4.2: $N_{\text{ch}}^{\text{raw}}$ for nine centrality bins at BES energies.

Centrality	BES energies($\sqrt{s_{NN}}$) GeV					
percentile	7.7	11.5	14.5	19.6	27	39
5%	185	221	239	263	288	326
10%	154	184	200	220	241	285
20%	106	127	138	152	168	199
30%	72	86	93	102	114	135
40%	46	56	59	66	74	88
50%	28	34	36	40	45	54
60%	16	19	20	23	26	30
70%	8	10	11	12	13	16
80%	4	5	5	6	6	7

4.1.3 Track Selection

Several cuts are applied to reconstructed charged particle tracks to ensure data quality. In this section, I explain each cut in detail. First, to eliminate false tracks formed by hits belonging to many different particles, the number of fit points in the TPC is required to be greater than 15. Then to avoid track splitting (where one long track is reconstructed as two shorter tracks), we require $\frac{\text{number of TPC fit points}}{\text{maximum number of possible fit points}} \geq 0.52$. Pileup tracks are identified during data production and flagged with an ID greater than 1000. I require all tracks to have $0 < \text{flag} < 1000$. These are the basic track quality cuts used during track selection; I discuss track selection criteria for particle identification and V0 reconstruction in the following sections.

4.2 Particle Identification

4.2.1 π^\pm , K^\pm and $p(\bar{p})$ Identification

Long-lived charged particles are identified using both energy loss information from the TPC and time of flight information from the TOF barrel. Some particles are identified using the ionization energy loss, dE/dx , in the gas of the TPC. The left panel of Figure 4.2 shows an example. For a minimum ionizing particle (MIP) that produces a single track with the maximum possible number of TPC pad rows crossed (45), the dE/dx resolution is found to be about 6 to 8% [75]. At lower momenta ($0.3 \leq p_T \leq 0.6 \text{ GeV}/c$), the energy loss bands show clear separation between particle types. The energy loss bands decrease with increasing momentum, reaches a minimum near $\beta\gamma \sim 3$ for every particle type, and then increase again due to relativistic rise. For the STAR TPC, the Bichsel function [84] is a good approximation for predicting the center of dE/dx bands. The normalized energy loss can be written [85]

$$n\sigma_{\text{particle}} = \ln \left(\frac{dE/dx_{\text{particle}}}{\langle dE/dx \rangle_{\text{Bichsel}}} \right) / \sigma_{\text{particle}} \quad (4.1)$$

where σ_{particle} is the TPC dE/dx resolution. The criterion $|n\sigma| \leq 2$ along with the other PID cuts gives a reasonably good separation between pions, kaons and protons.

Particle identification based on dE/dx in the TPC is further refined using TOF hit information. The squared mass (m^2) of the track is calculated from the time of flight and momentum information from the TPC:

$$\text{TOF mass}_{\text{track}}^2 = p_{\text{tot}}^2 \left(\frac{1}{\beta^2} - 1 \right) \quad (4.2)$$

where p_{tot} is the particle's total momentum, $\beta = l/(ct_{\text{TOF}})$, and in turn, l is the particle's path length, c is the speed of light, and t_{TOF} is the time of flight.

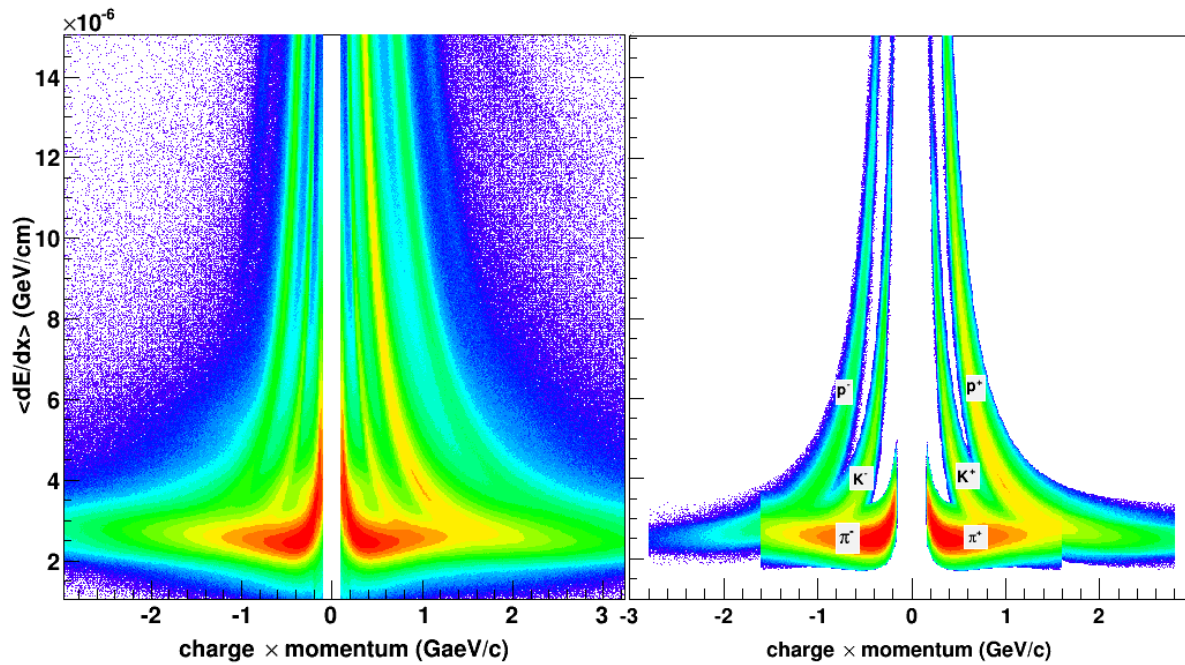


Figure 4.2: The plot on the left shows energy loss (dE/dx) for all particles as a function of electric charge times momentum in the TPC detector. The plot on the right shows dE/dx after particle identification cuts based on information from both TOF and TPC.

Without any particle identification cuts, the squared mass distribution for charged particles is shown in Figure 4.3. We select π^\pm , K^\pm and $p(\bar{p})$ based on the following m^2 selections:

$$\pi^\pm : -0.01 < m^2 < 0.10 \text{ GeV}^2/c^4$$

$$K^\pm : 0.20 < m^2 < 0.35 \text{ GeV}^2/c^4$$

$$p(\bar{p}) : 0.8 < m^2 < 1.0 \text{ GeV}^2/c^4$$

A small negative value for pions m^2 chosen to avoid cutting on the $n\sigma$ band. To further improve the purity of particle identification, the following cuts were also imposed on p_T and p_{tot} :

$$\pi^\pm : 0.2 \text{ GeV}/c \leq p_T \text{ and } p_{\text{tot}} \leq 1.6 \text{ GeV}/c$$

$$K^\pm : 0.2 \text{ GeV}/c \leq p_T \text{ and } p_{\text{tot}} \leq 1.6 \text{ GeV}/c$$

$$p(\bar{p}) : 0.4 \text{ GeV}/c \leq p_T \leq 2.0 \text{ GeV}/c \text{ and } p_{\text{tot}} \leq 2.8 \text{ GeV}/c$$

In addition, to exclude tracks from secondary vertices, we require a distance of closest approach to the primary vertex (DCA) of 3 cm or less. After imposing all of the above charged particle identification cuts, the resulting dE/dx distribution is shown in the right panel of Figure 4.2. To maintain consistency across published results, this study uses the same cuts for protons and pions as in a published STAR paper on directed flow for protons and pions [49].

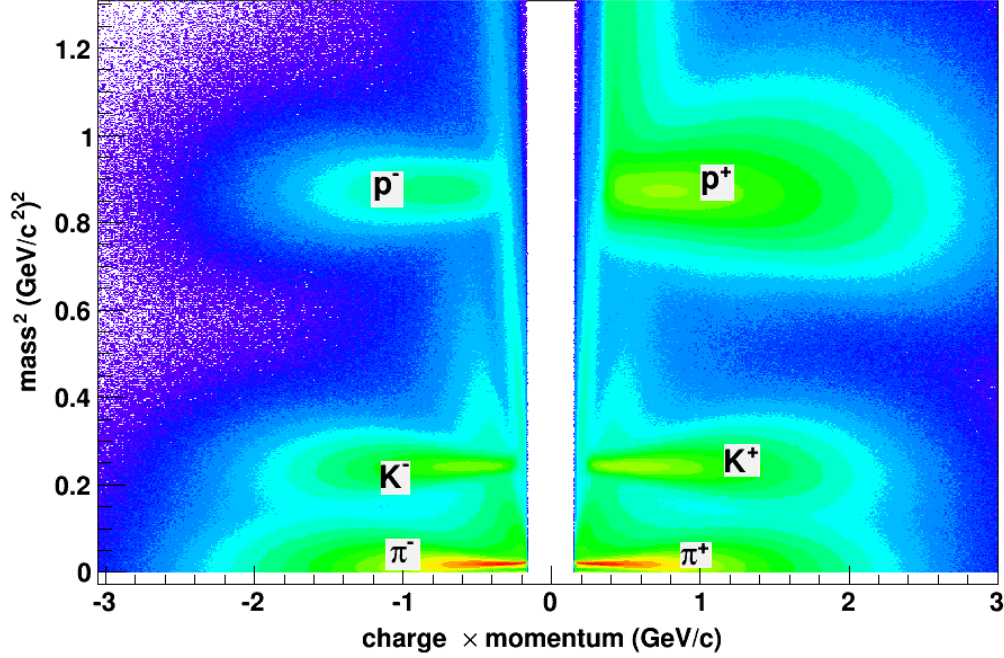


Figure 4.3: The mass^2 distribution from the TOF detector without any cuts for particle identification.

4.2.2 Reconstructing Λ , $\bar{\Lambda}$, K_S^0 and yields

The secondary vertices in a nuclear collision can be categorized into three groups:

- Kink vertices: a charged particle decays into a charged and neutral daughter.
- $V0$ vertices: a neutral particle decays into two charged daughters.
- Cascade vertices: a charged particle decays into a charged plus neutral daughter, and then the neutral particle decays into two charged particles.

In this dissertation, I am interested in the weakly-decaying neutral strange particles Λ , $\bar{\Lambda}$ and K_S^0 , all of which can be detected via their $V0$ topology (two oppositely charged daughters at a secondary vertex) as follows [86, 87]:

- Λ ($1115.68 \text{ MeV}/c^2$) \longrightarrow p^+ ($939.56 \text{ MeV}/c^2$) + π^- ($139.57 \text{ MeV}/c^2$) (63% branching fraction)

- $\bar{\Lambda}$ (1115.68 MeV/c²) \longrightarrow p^- (939.56 MeV/c²) + π^+ (139.57 MeV/c²) (63% branching fraction)
- K_S^0 (497.614 MeV) \longrightarrow π^+ (139.57 MeV/c²) + π^- (139.57 MeV/c²) (69% branching fraction)

Figure 4.4 shows a topological map of a $V0$ decay. Here the tracks P^+ and P^- are positive and negative charged decay daughters, respectively, PV denotes the primary vertex, and DCA denotes distance of closest approach. The coordinates of the positive and negative tracks are combined at the mid-point of the DCA between the two daughter tracks (DCA P^+ to P^- in the diagram) to form the parent particle decay vertex. The 4-momentum and other kinematic variables of the parent particle is obtained from the daughter momentum vectors at this same DCA [88]. If the reconstructed decay vertex passes the selection criteria (discussed in the next section), then the invariant mass of the parent particle is calculated using the mass hypothesis

$$m = \sqrt{\left(\sqrt{m_+^2 + P_+^2} + \sqrt{m_-^2 + P_-^2}\right)^2 - (P_+^2 + P_-^2)} \quad (4.3)$$

where m_+ and m_- are the appropriate daughter particle masses, as listed above.

There is a combinatoric background arising from unrelated pairs of particles from the primary vertex accidentally having an invariant mass near that of the relevant particle. This combinatoric background was reduced by directly identifying the decay daughters from dE/dx and/or m^2 information using the TPC and/or TOF. Since only 65% of the tracks have valid TOF information, m^2 cuts are not applied at all $V0$ vertices. A $|n\sigma| \leq 3$ cut is applied to normalized dE/dx for all particles, while an m^2 cut is applied to tracks which have TOF hit information. To compensate for the missing TOF information, tighter topological cuts are applied to tracks which have only TPC information. Several topological cuts are chosen from the helix parameters of reconstructed TPC tracks, such as DCA between daughter tracks, DCA to daughter tracks from primary vertex, DCA between the $V0$ vertex and the primary vertex, and the decay length of the $V0$ particle. These cuts are used in all STAR $V0$ analyses and are optimized

for maximum significance by systematically varying the cuts [27]. The selection criteria for V_0 vertices are summarized in table 4.3.

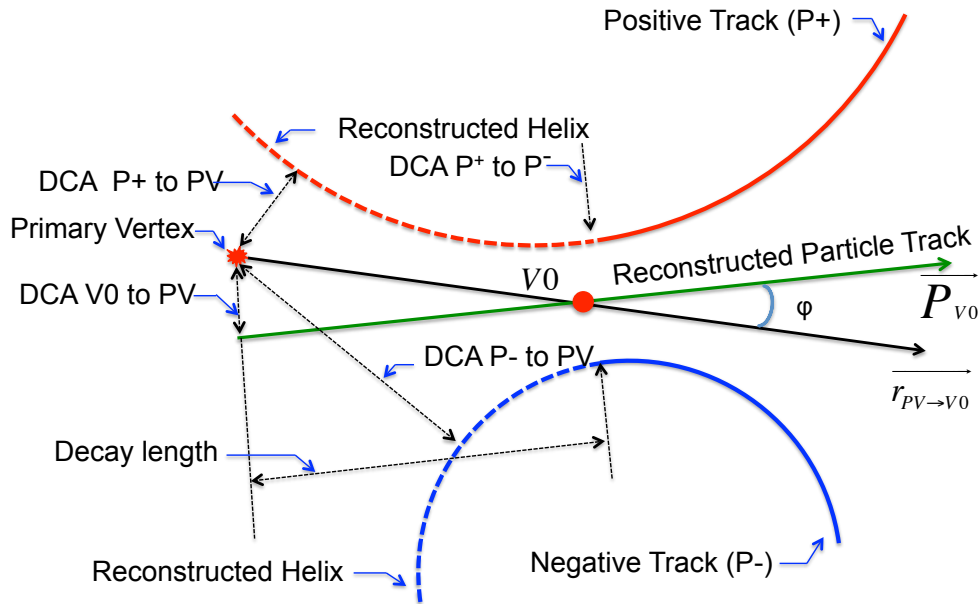


Figure 4.4: V_0 decay topology diagram.

Table 4.3: V_0 topological cuts for Λ and K_S^0 particles. A momentum-dependent lower mass cut for pions is selected to reject contamination from electron misidentification. All lengths are in centimeters and all masses are in GeV/c^2 .

V_0 cuts	$\Lambda(\bar{\Lambda})$				K_S^0
	Protons & pions have TOF	Only Protons have TOF	Only Pions have TOF	Neither have TOF	Independent of TOF
$n\sigma_{\text{Pion}}$	< 3.0				
$n\sigma_{\text{Proton}}$	< 3.0				-
TOF mass^2 Proton	$0.5 < m^2 < 1.5$				-
TOF mass^2 Pion	$(0.017 - 0.013 \times p_{\text{tot}}) < \text{mass}^2 < 0.04$				
DCA daughters	<1.00				
DCA Protons to PV	>0.1	>0.15	>0.5	>0.6	-
DCA Pion to PV	>0.7	>0.8	>1.5	>1.7	>0.7
DCA V_0 to PV	>1.3	>1.2	>0.75	>0.75	>0.8
Decaylength	>2.0	>2.5	>3.5	>4.0	>3.0

4.2.2.1 Mixed Event Background Estimation

The combinatoric background from uncorrelated particles is removed using the mixed-event technique. A temporary buffer of events is constructed using only the event and track parameters needed to form $V0$ vertices. Mixed events are chosen to have the same global properties as real events, which in the present case means centrality, vertex position along the z -axis (V_z) and event plane azimuth (Ψ_{RP}). Available events are divided into nine bins of centrality, ten bins for V_z and 30 bins for Ψ_{RP} , which makes a total of 2700 event classes. For each event class, five mixed events are built on the fly for each BES energy, except for 7.7 GeV. Because of the limited number of good positive and negative tracks in a mixed event class for the later case, 15 mixed events are built to increase the probability of a $V0$ vertex being reconstructed. After the required number of mixed events for a particular event class is acquired and $V0$ vertices are reconstructed, the corresponding event buffer class is deleted.

When a particular buffer of an event class is filled, each positive track in a selected event is combined with each negative track in the remaining events to reconstruct the $V0$ vertex. The above procedure for choosing positive tracks in a event is repeated for the remaining events in the buffer. Event mixing always results in a large number of reconstructed mixed events, and thus results in a larger number of reconstructed $V0$ background candidates than in the real event sample. Therefore, the mixed event background is normalized away from the mass region of the peak. The normalization region is chosen for Λ ($\bar{\Lambda}$) on the high-mass side of the peak, and for K_S^0 , both sides of the mass peak are used. This procedure is illustrated in Figure 4.5 for Λ . Panel (a) shows the reconstructed Λ candidates (signal + background) as a red histogram, and the mixed event background is the grey shaded area. In panel (b), the mixed event background is normalized, and in panel (c), the normalized background has been subtracted from the $V0$ candidates.

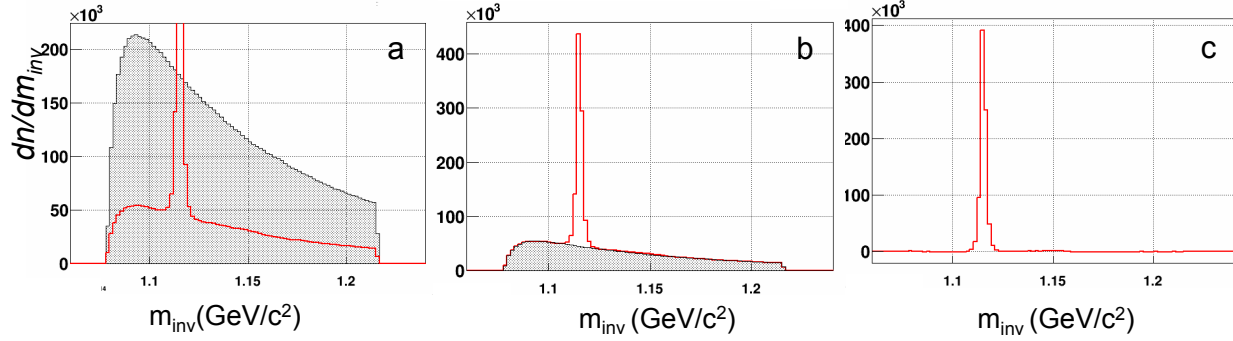


Figure 4.5: Illustration of mixed $V0$ event background estimation for Λ at $\sqrt{s_{NN}} = 11.5$ GeV for 10-40% centrality. Panel (a) shows the signal+background and the mixed event background; panel (b) shows the same after the background is normalized; and panel (c) presents the invariant mass peak for Λ after background subtraction.

4.2.2.2 Side Band Background Estimation

In addition to the mixed-event method, a side band method is also used to crosscheck the results. Figure 4.6 shows results of this method, where the background is estimated from an average of the signal+background in a region just below and just above the observed peak in the signal+background. Here we assume that the background linearity is good. Regions B_1 and B_2 are chosen each to be half the width of region B_0 . So B_0 can be approximated as $(B_1 + B_2)$. Further, we assume $S_1 \approx B_1$ and $S_2 \approx B_2$. Then the corrected yield is $S_0 - (S_1 + S_2)$. The results show excellent agreement between the mixed-event method and the side band method.

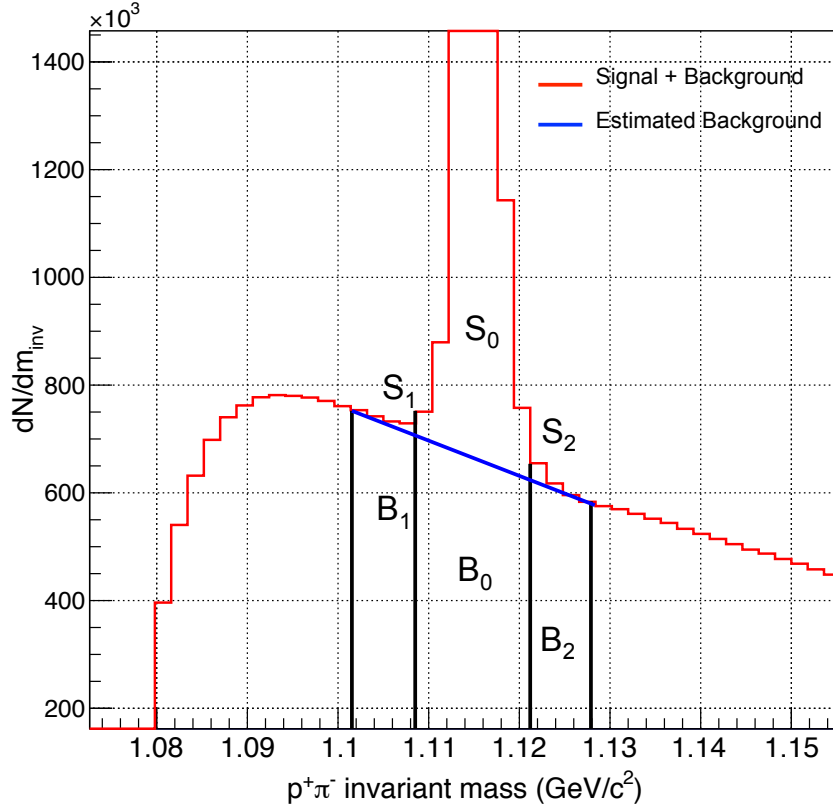


Figure 4.6: This plot illustrates the side band method in the case of the Λ signal. Vertical and horizontal axes are truncated for better clarity. S_0 , S_1 , and S_2 are signal + background entries, while B_0 , B_1 , and B_2 are background entries.

4.2.2.3 Rotational Background Estimation

This method is used for background estimation in many heavy-ion studies, and was the first method explored when I started this dissertation analysis. But this method can have a serious bias when used for V_0 flow [89]. In the rotational background method, one of the daughter tracks (protons, in my tests) is rotated by 180° in the transverse plane, and the resulting tracks are used to reconstruct the V_0 background. Rotation of protons causes the background v_1 to have the opposite sign from the signal v_1 , since the daughter proton carries most of the momentum of the parent Λ . This highly undesirable back-to-back correlation between signal and background is clearly seen when the rotational background method is investigated.

4.3 BBC Event Plane Calculation

The plane formed by the beam axis and the impact parameter is known as the reaction plane. Experimentally, it is impossible to find the true reaction plane in any given collision [37], so we approximate it with the observed event plane calculated from the anisotropy of produced particles. At $\sqrt{s_{NN}}$ up to 39 GeV, the BBC detectors offer a reasonably good event plane resolution. The inner two rings of the east and west BBC are used to calculate the event plane. The BBC and TPC + TOF are separated by a large η gap. This η gap ensures there is minimal non-flow contribution to the flow calculations in $|\eta| \leq 1.0$. The n^{th} harmonic event plane vector, \vec{Q}_n , is defined by the equations

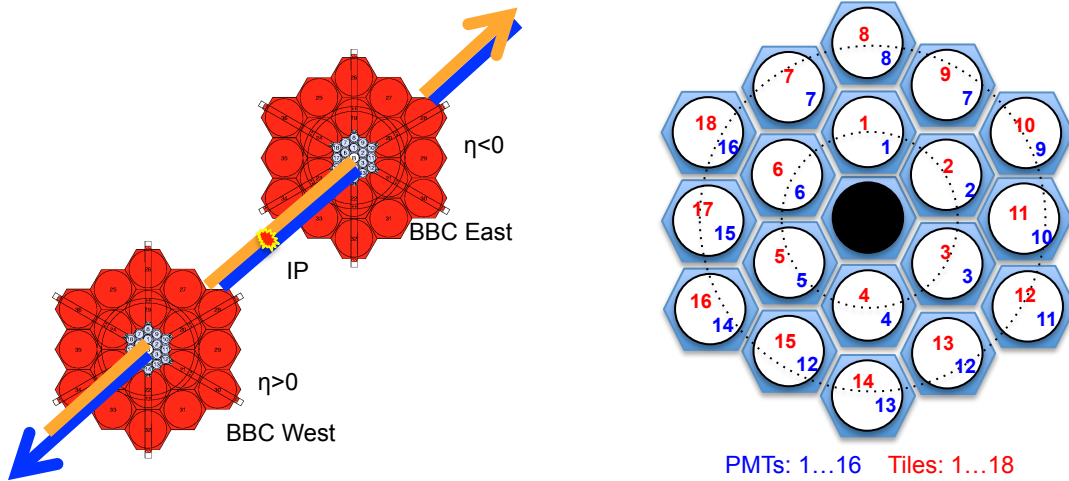


Figure 4.7: On the left is shown the west and east BBC detectors, for positive and negative η , respectively. On the right is shown the inner two rings of the BBC. The red numeral is tile number and blue numeral is the PMT number; these two are not always the same, since the read-out of tiles 7 and 9, and of 13 and 15, are coupled together.

$$Q_{n,x} = \sum_i w_i \cos(n\phi_i) = Q_n \cos(n\Psi_n) \quad (4.4)$$

$$Q_{n,y} = \sum_i w_i \sin(n\phi_i) = Q_n \sin(n\Psi_n) \quad (4.5)$$

$$w_i = \frac{A_i}{\sum A_i} \quad (4.6)$$

Here, ϕ_i is the azimuth of the center of the i^{th} tile of the BBC, and w_i the normalized and gain-corrected ADC value (the equivalent of energy deposition) in the i^{th} tile. The normalization for the east and west sides of the BBC is set independently.

The event plane angle Ψ_n for the n^{th} harmonic is calculated using

$$\Psi_n = \frac{\tan^{-1}(Q_{n,y}/Q_{n,x})}{n} \quad (4.7)$$

The imperfect azimuthal symmetry of the TPC (affected by imperfections such as sector boundaries, non-uniform efficiency, temporarily dead channels, etc.) makes the reconstructed event plane distribution non-uniform (not-flat), and could bias flow measurements if not corrected [90]. Figure 4.8 shows a 1st-order raw event plane distribution for BES energies. To correct this non-uniformity, three methods are widely used, namely phi weighting, re-centering, and shifting. In this dissertation, the shifting method is used.

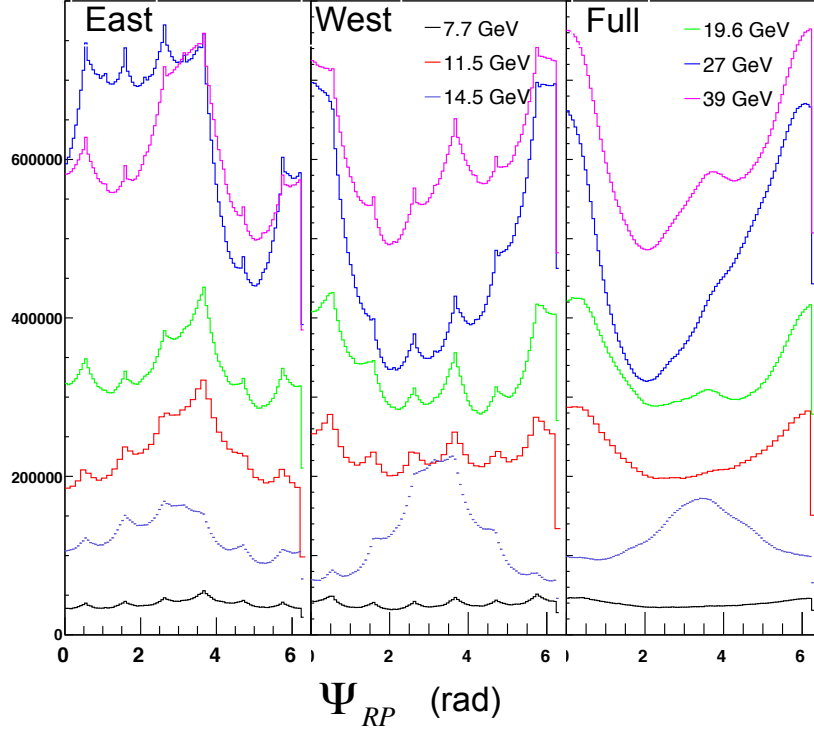


Figure 4.8: Raw event plane distribution for east, west and full event plane calculations.

4.3.0.1 Shift Correction

In the shift correction method [91], a correction term is chosen to force the n^{th} Fourier harmonic in the raw event plane distribution, Ψ , to become flat. The raw event plane distribution can be expanded in a Fourier series as follows:

$$\frac{dN}{d\Psi} = \frac{a_0}{2} + \sum_n (a_n \cos n\Psi + b_n \sin n\Psi) \quad (4.8)$$

where coefficients a_n and b_n are

$$a_n = \frac{1}{\pi} \int_{-\pi}^{\pi} \frac{dN}{d\Psi} \cos n\Psi d\Psi, \quad n = 0, 1, 2, \dots \quad (4.9)$$

$$b_n = \frac{1}{\pi} \int_{-\pi}^{\pi} \frac{dN}{d\Psi} \sin n\Psi d\Psi, \quad n = 0, 1, 2, \dots \quad (4.10)$$

Then the corrected event plane Ψ' can be written

$$\Psi' = \Psi + \Delta\Psi \quad (4.11)$$

where $\Delta\Psi$ is the correction term and can be written in the form

$$\Delta\Psi = \sum_n (A_n \cos n\Psi + B_n \sin n\Psi) \quad (4.12)$$

By imposing the condition of a flat distribution on Eq. 4.11 (requiring the n^{th} Fourier harmonic to vanish), it is found that

$$\frac{dN}{d\Psi'} = \frac{N}{2\pi} = \frac{a_0}{2} \quad (4.13)$$

Now we can re-arrange Eq. 4.8

$$\frac{dN}{d\Psi} = \frac{dN}{d\Psi'} \frac{d\Psi'}{d\Psi} = \frac{a_0}{2} \left[1 + \sum (-nA_n \sin n\Psi + nB_n \cos n\Psi) \right] \quad (4.14)$$

Comparing the above with Eq. 4.8, we find the coefficients A_n and B_n and the new corrected event plane distribution:

$$\Psi' = \Psi + \sum \frac{1}{n} (-\langle \sin 2n\Psi \rangle \cos 2n\Psi + \langle \cos 2n\Psi \rangle \sin 2n\Psi) \quad (4.15)$$

Here, the angle brackets mean the average over a large number of events. To get a reasonably flat event plane distribution, it is necessary to repeat the calculation of the correction term multiple times, first to initialize the parameters, and then to find the correction terms. Also, in this analysis, we use up to the 20th harmonic to flatten the raw distribution. Figure 4.9 shows such a shift-corrected 1st-order event plane distribution for BES energies.

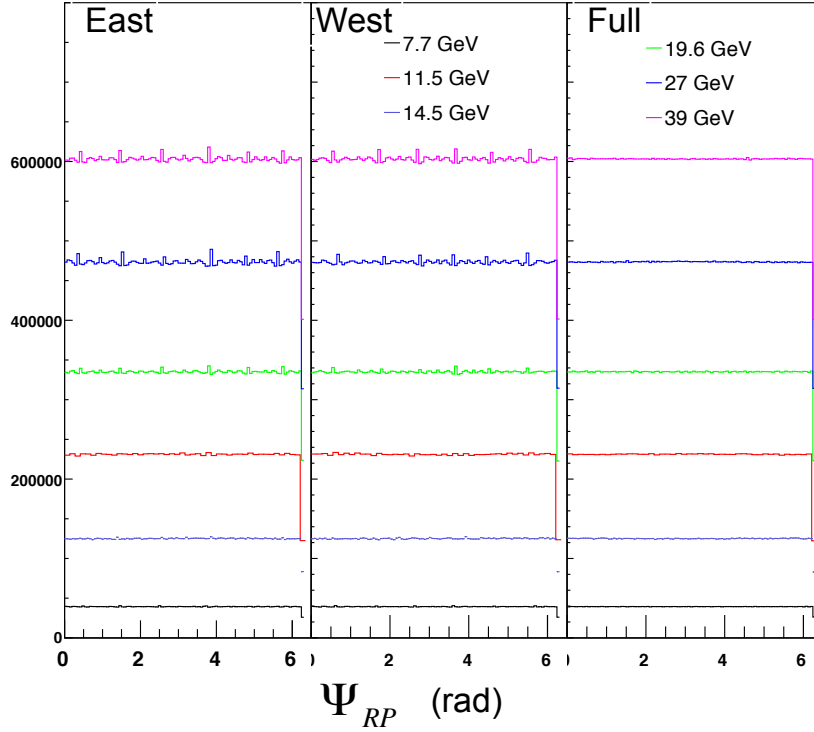


Figure 4.9: The shift-corrected event plane distribution for east, west and full event plane calculations. The distributions for 27 GeV and 39 GeV are scaled by factors of 0.75 and 0.5, respectively.

4.3.0.2 Event Plane Resolution

The event plane resolution depends on several factors, including the multiplicity of the particles used in the determination of the event plane. The event plane resolution for each harmonic is given by [37]

$$R_n = \langle \cos n(\Psi_n - \Psi_{RP}) \rangle \quad (4.16)$$

Here, angle brackets mean the average over large number of events. The resolution of the event plane strongly depends on centrality, so these corrections should be applied in small centrality bins (in our analysis, 10% centrality increments). East and west BBC detectors are

independent; therefore the correlation between two event planes can be written

$$\langle \cos n (\Psi_{\text{east}} - \Psi_{\text{west}}) \rangle = \langle \cos n (\Psi_{\text{east}} - \Psi_{\text{RP}}) \rangle \langle \cos n (\Psi_{\text{west}} - \Psi_{\text{RP}}) \rangle \quad (4.17)$$

If we assume that the two sub-detectors (east and west) have similar event plane resolution, then the sub-event plane resolution can be written

$$R_{n,\text{sub}} = \sqrt{\langle \cos n (\Psi_n^{\text{east}} - \Psi_n^{\text{west}}) \rangle}. \quad (4.18)$$

The first-order event plane has poor resolution. A full event plane analysis deals with twice the particle multiplicity as a sub-event plane analysis [37, 92]. Therefore we can approximate the full event plane resolution using

$$R_{\text{full}} \approx \sqrt{2} R_{\text{sub}}. \quad (4.19)$$

Figure 4.10 shows the 1st-order event plane resolution. This resolution improves at lower energies due to the strong v_1 signal near beam rapidities, which increasingly overlaps with the BBC acceptance as the beam energy drops.

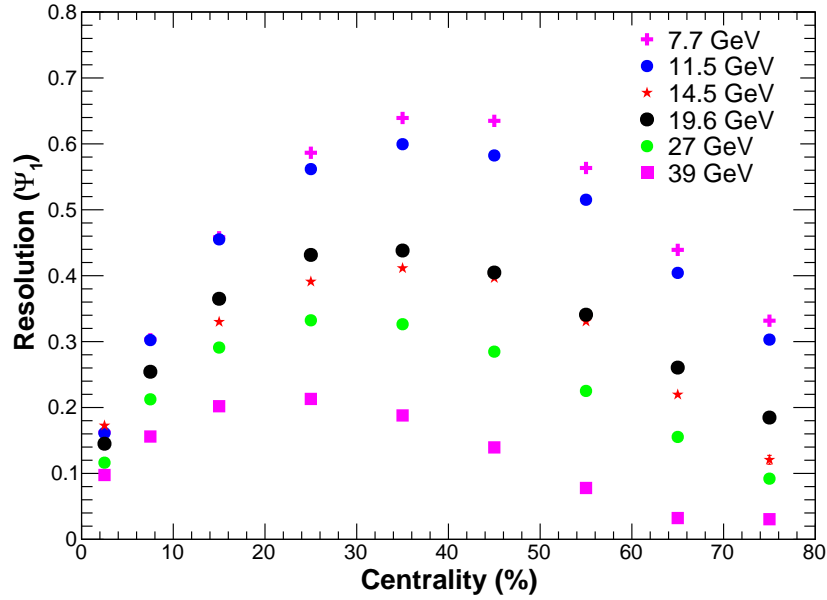


Figure 4.10: First order event plane resolution for all BES energies.

4.4 Directed Flow Measurements

The full event plane reconstructed using the east and west BBC is used to measure directed flow of particles produced in the TPC acceptance ($|y| \leq 1.0$). Eq. 2.1 shows the azimuthal distribution of produced particle with respect to the reaction plane. The first Fourier coefficient in this equation is the directed flow, v_1 . The directed flow for a given rapidity window, for all p_T , can be written in the form

$$v_1^{\text{obs}}(y_j, \forall p_T) = \langle \cos(\phi_i - \Psi_{\text{RP}}) \rangle \quad (4.20)$$

Here, “obs” means the observed directed flow before correcting for the reaction plane resolution. The angle brackets denote an average over all particles in all events, ϕ_i is the azimuthal angle of particle i , and Ψ_{RP} is the first-order event plane. The true directed flow, corrected for event plane resolution, is

$$v_1 = \frac{v_1^{\text{obs}}}{R_1} \quad (4.21)$$

where R_1 is the first-order event plane resolution. Since, R_1 is a strong function of centrality, this step is implemented in fine centrality bins: 0-5%, 5-10%, 10-20%, 20-30%, 30-40%, 40-50%, 50-60%, 60-70% and 70-80%.

4.4.1 Directed Flow of Charged Particles – $\pi^\pm, K^\pm, p(\bar{p})$

Since $\pi^\pm, K^\pm, p(\bar{p})$ particles were directly identified from TPC and TOF, and no post processing is needed on PID signals, directed flow for these particles is calculated and stored in profile histograms as soon as each particle is identified.

4.4.2 Directed Flow of Neutral Strange Particles – $\Lambda, \bar{\Lambda}, K_S^0$

Directed flow calculation for $V0$ particles is not as simple as for charged particles. After identifying possible $V0$ candidates, it is necessary to remove the background to extract the signal. The steps to extract the signal and then calculate the directed flow for $V0$ particles are explained below.

1. Possible $V0$ candidates (signal+background) and mixed event background candidates are reconstructed as described in 4.2.2.
2. One-dimensional histograms containing invariant masses of both signal+background and background are stored in two separate, three-dimensional arrays, where the three array dimensions are centrality, rapidity, and $\phi - \Psi_{RP}$. Nine centrality bins span the centrality interval 0-80%, 10 rapidity bins cover $|y| \leq 1.0$, and 30 bins of $\phi - \Psi_{RP}$ extend over $[0 - 2\pi]$.

Figure 4.11 shows a two-dimensional histogram of invariant mass and $\phi - \Psi_{RP}$ for Λ at 30-40% centrality and at $0.2 < y \leq 0.4$, based on Au+Au collisions at 19.6 GeV. The plot on the left shows the signal and background, while on the right is the normalized mixed-event background.

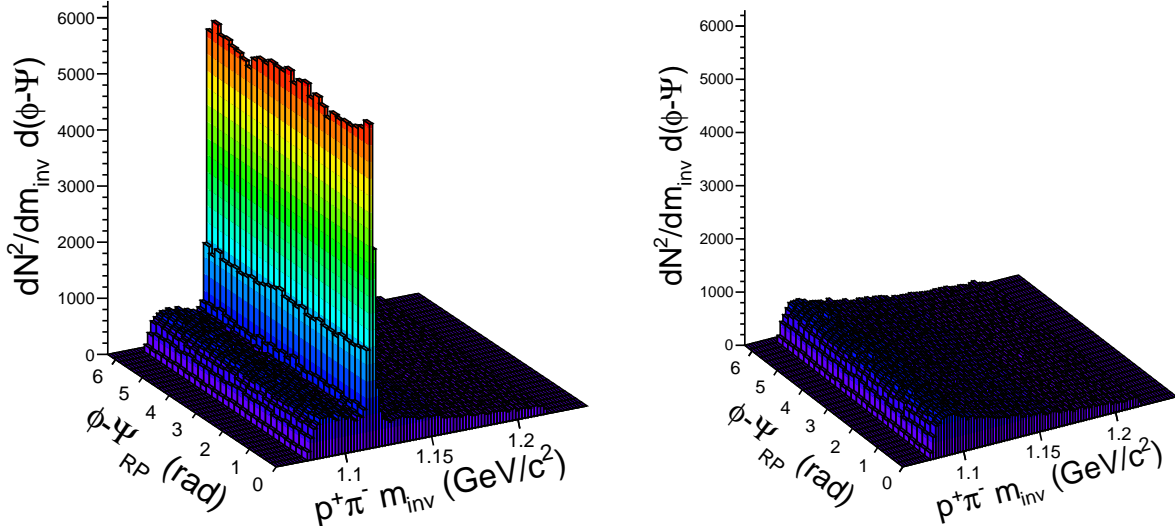


Figure 4.11: Histogram of signal+background (left) and normalized mixed-event background (right) for Λ as a function of invariant mass and $\phi - \Psi_{\text{RP}}$. These histograms are for 30-40% centrality Au+Au collisions at $\sqrt{s_{\text{NN}}} = 19.6$ GeV, with rapidity $0.2 < y \leq 0.4$.

3. The available dataset is too large to process all the events at once. This requires the data to be split into groups, each processed separately. At the end, to properly estimate the signal to background, all the groups are combined.
4. For each bin defined in step two above, the V_0 signal is extracted by removing the background. Then the yield is the integral of entries in the defined mass window. For $\Lambda(\bar{\Lambda})$ the mass is 1.1157 ± 0.007 GeV/ c^2 and for K_S^0 , the mass is 0.496 ± 0.024 GeV/ c^2 , which are chosen to agree with values published by the Particle Data Group [86, 87].
5. For each centrality bin (c_i) and each rapidity bin (y_j) for all p_T , directed flow is calculated using equation 4.22:

$$v_1(c_i, y_j, \forall p_T) = \frac{\sum_{k=0}^{29} dn_k \left(\frac{\cos(\phi - \Psi_{\text{RP}})_k}{R_1^i} \right)}{\sum_{k=0}^{29} dn_k} \quad (4.22)$$

where R_1^i is the event plane resolution for the i^{th} centrality bin, and dn_k is the yield in the k^{th} bin of $\cos(\phi - \Psi_{\text{RP}})$.

4.4.3 Systematic Uncertainties

In this section, I discuss possible errors in v_1 calculations due to systematic uncertainties, and explain how the systematic uncertainties are estimated. A detector that is non-symmetric about the along the beam axis can introduce systematic error in v_1 calculations [93]. We have neglected possible error from this type of asymmetry since the STAR detector has desired east-west symmetry for the TPC, TOF and BBC detectors used in this analysis. The large pseudorapidity gap between BBC and TPC allows us to neglect the non-flow contribution in v_1 calculations [37, 94].

Another possible source of systematic error is from the event plane calculation. The number of track hits in BBC tiles and the number of tracks used to reconstruct the event plane can affect the BBC event plane resolution. Therefore, event and track quality cuts can influence the event plane resolution. Directly identifying the systematic error associated with event plane calculations is very challenging. So we estimate the systematic uncertainty by assuming that the difference between the two event plane flattening techniques, the shifting method and the ψ method [95, 96], provides a rough estimate of the systematic uncertainty. This source of systematic error is estimated as less than 1% [81].

v_1 is a measure of the relative yield in small bins of $(\phi - \Psi)$. The assumption here is that the efficiency is constant as a function of centrality and as a function of the angle relative to Ψ . The results are not explicitly corrected for feed-down, although the systematic effect from varying DCA cuts (see below) partially takes care of the contributions from feed-down. In addition, previous studies [97] show that feed-down is significant for pions below $p_T \sim 0.4$ GeV/c, while for other particles, feed-down corrections are negligible.

In addition, different p_T cuts are also studied, but such variations are not considered to contribute to the systematic error. Any experimental or theoretical analysis that is compared

with the present results ought to use exactly the same p_T selection. A linear fit is used to find the slope of dv_1/dy , for the rapidity range $|y| \leq 0.8$. The fit range was varied to $|y| \leq 0.6$ in order to test sensitivity to the fit, but again, for the same reason as mentioned immediately above, this variation does not contribute to the final systematic error.

4.4.3.1 Detector Acceptance and Efficiency

Point-by-point systematic errors on parameters used for event selection, track selection, particle identification and topological selections are studied. Most cuts were varied $\pm 20\%$ from the reference values. Some special cuts don't follow the $\pm 20\%$ guideline. For example, I use zero for the lower value of the $\frac{n\text{Hits}}{n\text{HitsPossible}}$ cut, to check the full effect of the cut in the analysis. For all systematic checks, the various cuts are changed one at a time. Next, I explain the procedure followed to identify the point-by-point systematic error using the $\Lambda(\bar{\Lambda})$ as an example:

1. Each cut is varied $+20\%$ and -20% from the default value, which gives a minimum and maximum on either side of the default value.
2. Table 4.4 shows the systematic cuts, and minimum and maximum values used for event and track quality selection for Λ .
3. The last column in this table is a unique identification number assigned to each systematic cut to identify the minimum and maximum cut in the plots that follow.
4. Similarly, Table 4.5 shows $V0$ topological cuts and variations used for systematics.
5. For each variation, rms values are found. There are 26 options, but some identification numbers are not assigned.

$$\text{RMS} = \sqrt{\frac{1}{2} \sum_{i=\text{min,max}} (y_i - y_{\text{default}})^2} \quad (4.23)$$

6. Then the final systematic error is calculated using

$$\text{systematic error} = \sqrt{\sum_{j=0}^N \text{RMS}_j^2} \quad (4.24)$$

where N = the total number of cut variations used for the systematic study.

7. Similarly, Tables 4.6 and 4.7 describe the K_S^0 systematic cuts. Tables 4.8 and 4.9 refer to proton and pion systematic cuts.

Table 4.4: Minimum and maximum event and track cuts used for systematic study of $\Lambda(\bar{\Lambda})$. The cut number is a unique identifier assigned to each minimum and maximum cut value, used later to identify that variation in the plots. All lengths are in centimeters, all momenta are in GeV/ c and all masses are in GeV/ c^2 .

Cut	Default	Minimum	Maximum	Cut Number
Event				
V_z	50	40	60	1,2
Track				
Proton nHits	15	12	18	3,4
Proton $\frac{\text{nHits}}{\text{nHitsPossible}}$	0.52	0.0	0.60	5,6
Proton $n\sigma$	3.0	2.0	3.25	7,8
Proton mass ²	$0.5 \leq m^2 \leq 1.5$	$0.8 \leq m^2 \leq 1.0$	-	9
Pion nHits	15	12	18	11,12
Pion $\frac{\text{nHits}}{\text{nHitsPossible}}$	0.52	0.0	0.60	13,14
Pion $n\sigma$	3.0	2.0	3.25	15,16
Pion mass ²	$0.017 - 0.013 \times p \leq m^2 \leq 0.04$	$-0.01 \leq m^2 \leq 0.1$	-	17

Table 4.5: Minimum and maximum p_T , $V0$ and decay daughter track cuts used to estimate systematic errors for $\Lambda(\bar{\Lambda})$. The cut number is a unique identifier assigned to each minimum and maximum cut, used later to identify that variation in the plots. All lengths are in centimeters, all momenta are in GeV/c and all masses are in GeV/c^2 .

V0 Cuts	$\Lambda(\bar{\Lambda})$								Cut Number
	Proton & Pions have TOF		Only Protons have TOF		Only for Pions have TOF		Neither has TOF		
$V0 p_T$	$0.4 \leq p_T \leq 5.0$				$ p < 2.8 \ \& \ 0.4 \leq p_T \leq 2.0$				19
DCA Proton to PV	Default	Min 0.80	>0.15	0.12	>0.5	0.4	>0.6	0.48	(min)25
	>0.1	Max 0.12		0.18		0.6		0.72	(max)26
DCA Pion to PV	>0.7	0.56	>0.8	0.64	>1.5	1.2	>1.7	1.36	27
		0.84		0.96		1.8		1.24	28
DCA V0 to PV	1.3	1.04	>1.2	0.96	>0.75	0.6	>0.75	0.6	21
		1.56		1.44		0.9		0.9	22
Decaylength	>2.0	1.6	>2.5	2.0	>3.5	2.8	>4.0	3.2	23
		2.4		3.0		4.2		4.8	24
DCA daughters	<1.00				0.8				29
					1.2				30

Table 4.6: Minimum and maximum event and track cuts used to estimate systematic errors for K_S^0 . The cut number is a unique identifier assigned to each minimum and maximum cut, used later to identify that variation in the plots. All lengths are in centimeters.

Cut	Default	Minimum	Maximum	Cut Number
Event				
V_z	50	40	60	1,2
Track				
Pion nHits	15	12	18	3,4
Pion $\frac{\text{nHits}}{\text{nHitsPossible}}$	0.52	0.0	0.6	5,6
Pion $n\sigma$	3.0	2.0	3.25	7,8

Table 4.7: Minimum and maximum p_T , $V0$ and decay daughter track cuts used to estimate systematic errors for K_S^0 . The cut number is a unique identifier assigned to each minimum and maximum cut, used later to identify that variation in the plots. All lengths are in centimeters, and all momenta are in GeV/c.

$V0$	K_S^0		Cut Number
	Independent of TOF		
$V0 p_T$	$0.4 \leq p_T \leq 5.0$	$1.6 \leq p \ \& \ 0.2 \leq p_T$	9
		-	-
DCA pions to PV	> 0.7	0.56	11
		0.84	12
DCA $V0$ to PV	> 0.8	0.64	13
		0.96	14
Decay length	> 3.0	2.4	15
		3.6	16
DCA Daughters	< 1.0	0.8	17
		1.2	18

Table 4.8: Minimum and maximum event and track cuts used to estimate systematic errors for protons. The cut number is a unique identifier assigned to each minimum and maximum cut, used later to identify that variation in the plots. All lengths are in centimeters, all momenta are in GeV/c and all masses are in GeV/c².

Cut	Default	Minimum	Maximum	Cut Number
Event				
V_z	50	40	60	1,2
Track				
nHits	15	12	18	3,4
$\frac{n\text{Hits}}{n\text{HitsPossible}}$	0.52	0.00	0.6	5,6
$n\sigma$	2.0	1.6	2.4	7,8
mass ²	$0.8 < m^2 < 1.0$	$0.72 < m^2 < 1.1$	$0.88 < m^2 < 0.9$	9,10
DCA	3.0	2.4	3.6	11,12
Momentum	$2.8 > p \ \& \ 0.4 \leq p_T \leq 2.0$	$3.36 > p \ \& \ 0.32 \leq p_T \leq 2.4$	$2.24 > p \ \& \ 0.48 \leq p_T \leq 1.6$	13,14

Table 4.9: Minimum and maximum events cuts used to estimate systematic errors for pions and kaons. The cut number is a unique identifier assigned to each minimum and maximum cut, used later to identify that variation in the plots. All lengths are in centimeters, all momenta are in GeV/c and all masses are in GeV/c².

Cut	Default	Minimum	Maximum	Cut Number
Event				
V_z	50	40	60	1,2
Track				
nHits	15	12	18	3,4
$\frac{n\text{Hits}}{n\text{HitsPossible}}$	0.52	0.00	0.6	5,6
$n\sigma$	2.0	1.6	2.4	7,8
pion mass ²	$-0.01 < m^2 < 0.1$	$-0.005 < m^2 < 0.05$	$-0.015 < m^2 < 0.15$	9,10
kaon mass ²	$0.2 < m^2 < 0.35$	$0.2 < m^2 < 0.30$	$0.18 < m^2 < 0.4$	9,10
DCA	3.0	2.4	3.6	11,12
Momentum	$2.8 > p \ \& \ 0.4 \leq p_T \leq 2.0$	$3.36 > p \ \& \ 0.32 \leq p_T \leq 2.4$	$2.24 > p \ \& \ 0.48 \leq p_T \leq 1.6$	13,14

CHAPTER 5

EXPERIMENTAL RESULTS

This chapter presents rapidity-dependent directed flow and centrality-dependent directed flow measurements for all BES energies. Rapidity-dependent directed flow, $v_1(y)$, is presented for particle types Λ , $\bar{\Lambda}$, K_S^0 and K^\pm . Then the centrality dependence of directed flow is presented for particles types p , Λ , π^\pm , K_S^0 and K^\pm . Theoretical model calculations are already presented in Chapter 2. This chapter focuses purely on the experimental results and observations.

5.1 V_0 Invariant Mass Distributions

The invariant mass distribution of Λ baryons is shown in Figure 5.1. It shows the signal + background distribution, and the estimated background distribution from the mixed event technique, for the beam energy 11.5 GeV, for 10-40% centrality Au+Au collisions. Similarly, Figure 5.2 shows the invariant mass distribution for K_S^0 . In directed flow calculations, to ensure that the signal + background V_0 candidates and the background candidates differ only in the way intended, V_0 candidates are grouped into fine bins of centrality, rapidity, and $(\phi - \Psi_{\text{RP}})$ as described in Section 4.4.2. Invariant mass distributions in 30 bins of $(\phi - \Psi_{\text{RP}})$, for each particular centrality and rapidity bin, are shown in Figure 5.3 for Λ and in Figure 5.4 for K_S^0 . These are two typical cases, and all the other mass distributions look similar.

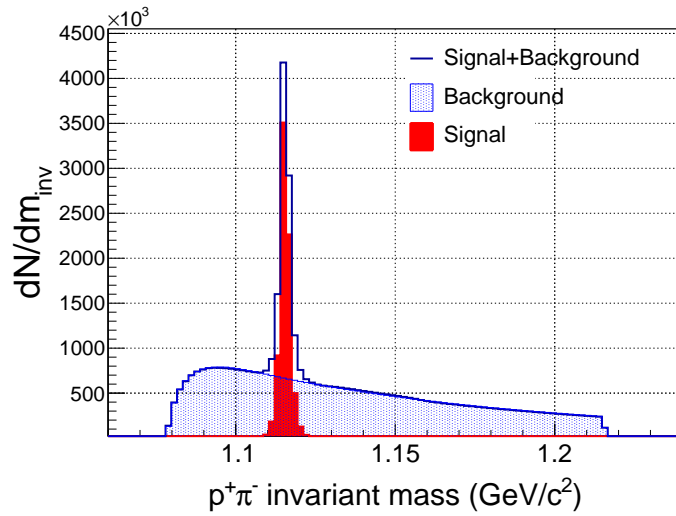


Figure 5.1: Invariant mass distribution of Λ for 10-40% centrality at $\sqrt{s_{NN}} = 11.5$ GeV. The solid blue histogram shows signal + background. The blue shaded area shows the mixed event background. The solid red area shows background-subtracted Λ candidates.

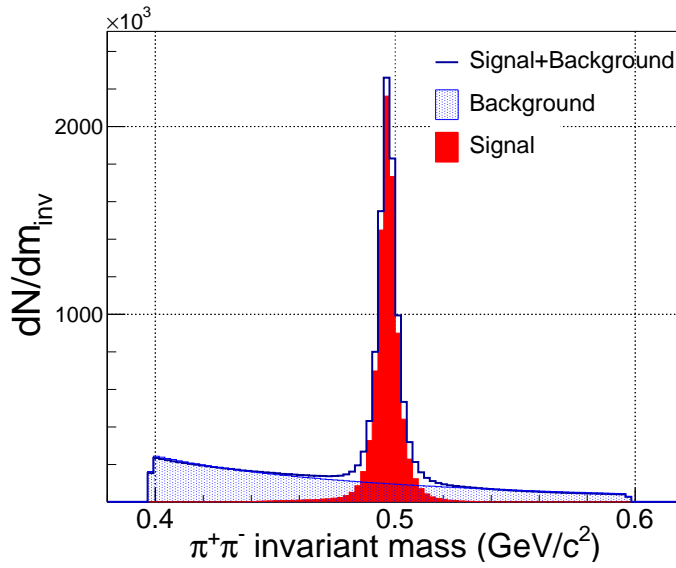


Figure 5.2: Invariant mass distribution of K_S^0 for 10-40% centrality at $\sqrt{s_{NN}} = 11.5$ GeV. The solid blue histogram shows signal + background. The blue shaded area shows the mixed event background. The solid red area shows background-subtracted K_S^0 candidates.

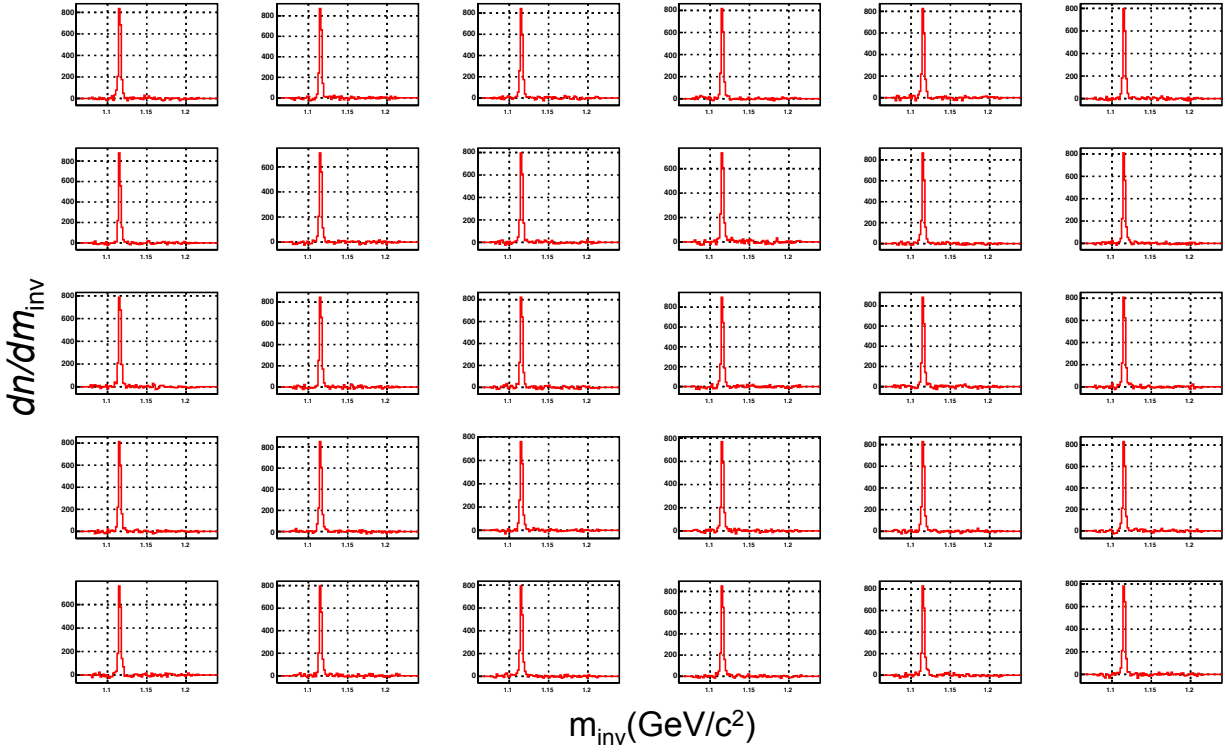


Figure 5.3: Λ invariant mass in thirty bins of $(\phi - \Psi_{\text{RP}})$ is shown for $-0.8 \leq y \leq -0.6$ and 30-40% centrality Au+Au collisions at a beam energy of 11.5 GeV.

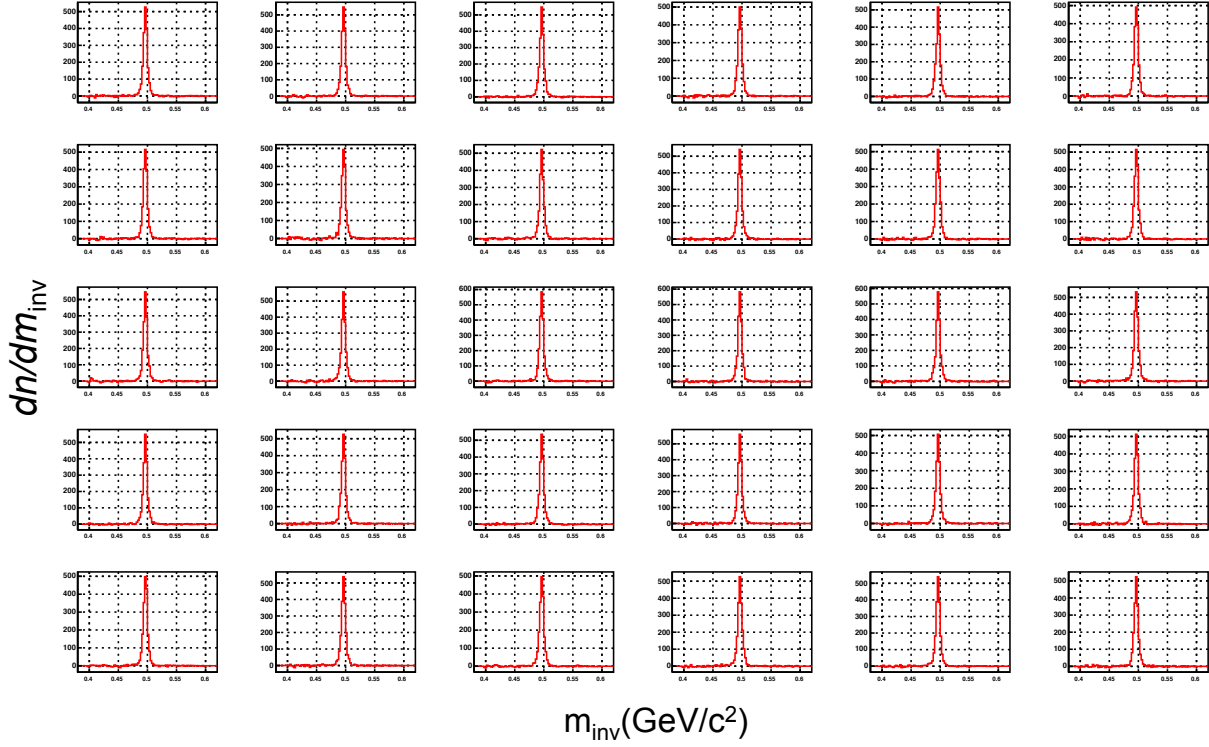


Figure 5.4: K_S^0 invariant mass in thirty bins of $(\phi - \Psi_{RP})$ is shown for $0.4 \leq y \leq 0.6$ and 20-30% centrality Au+Au collisions at a beam energy of 7.7 GeV.

5.2 Rapidity Dependence of Directed Flow

5.2.1 Intermediate Centrality Au+Au Collisions

Anisotropic flow is generally a maximum for intermediate centrality, and drops for both peripheral and central collisions. Because of limited statistics, the first directed flow study at BES energies [49] put its main focus on the intermediate centrality interval 10-40%. In this dissertation, the initial focus is on three key findings for intermediate centrality. First I present v_1 measurements from BES data recorded by the STAR detector. Second, I present similar v_1 calculations from events generated by the UrQMD model. Third, I present net-particle analysis for protons, lambdas and kaons. The results from central (0-10%) and peripheral (40-80%) collisions are presented later in this chapter.

5.2.1.1 BES Data Analysis

Figure 5.5 shows v_1 as a function of rapidity (y) for all BES energies and for nine particle species at 10-40% centrality. Except for 14.5 GeV, results for 4 particle species, namely p , \bar{p} and π^\pm , are already published by STAR [49]. Because the 14.5 GeV energy data are now available, for completeness, the full set of data for p , \bar{p} and π^\pm are presented here. The top row shows results for protons. At 7.7 GeV, proton v_1 has positive slope, then becomes negative at 11.5 GeV, and remains negative and small for the rest of the BES energies. The sign of the v_1 slope is assigned according to a historical convention. Positive v_1 is defined, in a fixed target experiment, as the direction of projectile spectator fragments, which always undergo repulsive scattering in the reaction plane at relativistic energies. The next row shows results for Λ , where v_1 is very similar to proton v_1 . The third and fourth rows show results for \bar{p} and $\bar{\Lambda}$, which have the poorest statistics of the 9 species studied, especially at 7.7 GeV. These particles show negative and large v_1 for all BES energies. Rows five, six and seven show K^+ , K^- and K_S^0 , respectively. Directed flow of these particles remains negative for all BES energies. The last two rows are for charged pions, which also show negative slope for all BES energies.

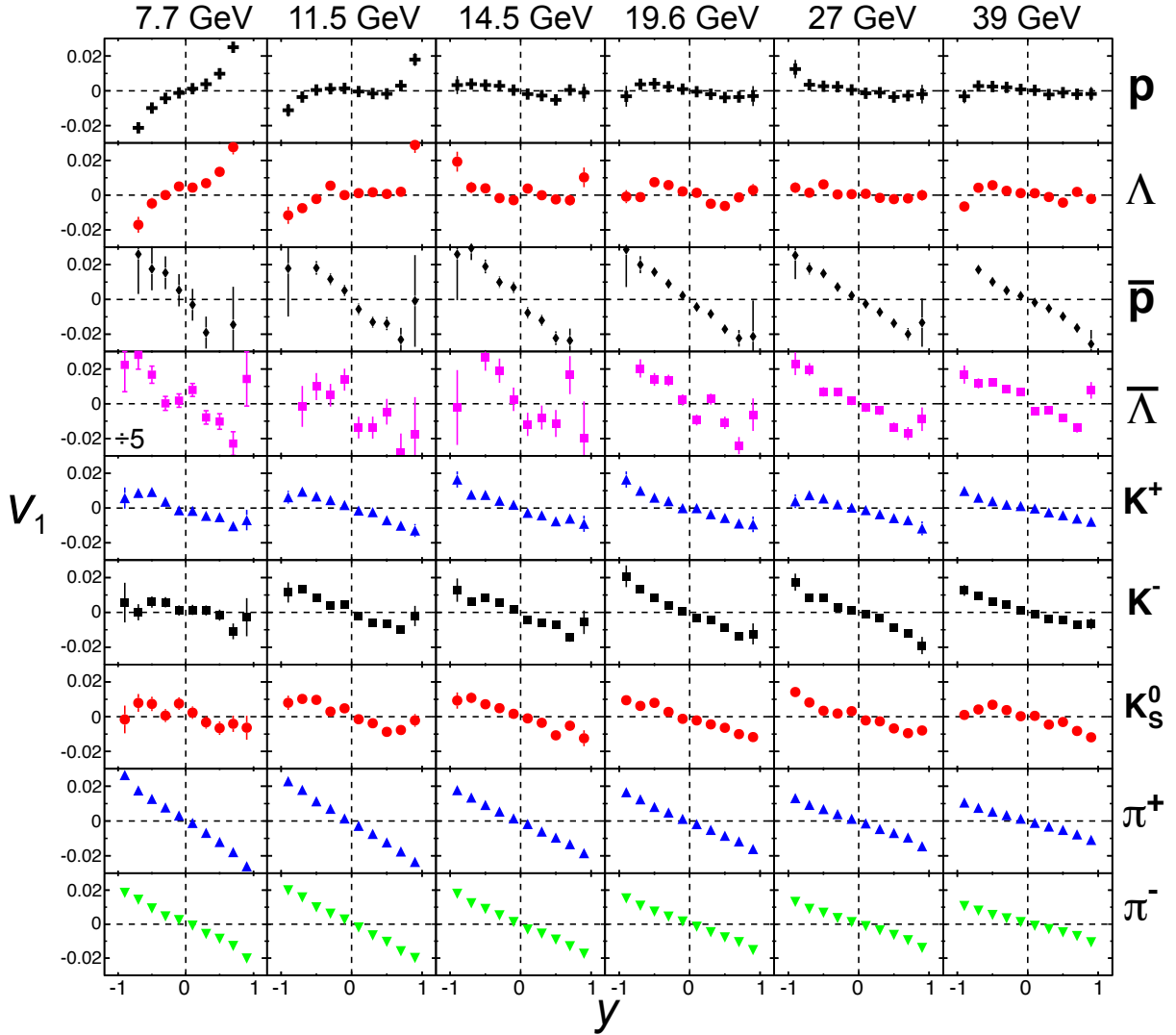


Figure 5.5: Directed flow (v_1) as a function of rapidity for p , Λ , \bar{p} , $\bar{\Lambda}$, K^\pm , K_s^0 and π^\pm for 10-40% centrality Au+Au collisions. Error bars are statistical. The v_1 magnitude is exceptionally large for $\bar{\Lambda}$ at 7.7 GeV, and therefore in that panel only, v_1 and its errors are divided by 5 to fit on the common vertical scale.

The strength of directed flow near midrapidity is quantified by the slope of $v_1(y)$. In this analysis, a linear fit to the data is carried out over the rapidity range $|y| \leq 0.8$. Throughout this dissertation, the term “ v_1 slope” is shorthand for $dv_1/dy|_{y \leq 0.8}$. In the previous STAR analysis of BES v_1 [49], a slightly different definition was used, namely, a cubic fit was carried out as per $v_1(y) = Fy + Cy^3$, and the linear term F was defined as the v_1 slope. When statistics are good, this approach has the advantage of less sensitivity to the fit range. The disadvantage,

and the reason for a different definition in the present dissertation, is that the cubic fit becomes unstable for rarer particle types, because of poorer statistics. The two methods give similar values for the slope when statistics are good, e.g., for protons and pions at energies above 14.5 GeV.

Figure 5.6 shows dv_1/dy for Λ , $\bar{\Lambda}$, p , \bar{p} and π^\pm , as a function of beam energy for 10-40% centrality. As discussed earlier, the v_1 slope for protons shows a positive slope at 7.7 GeV, then at 11.5 GeV it becomes close to zero. Above 11.5 GeV, the v_1 slope for protons remains negative. Protons show a statistically significant minimum in the v_1 slope, as predicted by models with a strong “softening” effect. Within statistical errors, Λ dv_1/dy shows similar results as for protons. Slopes for \bar{p} , $\bar{\Lambda}$ and π^\pm are all negative and large in magnitude compared to p and Λ , for all beam energies. \bar{p} and $\bar{\Lambda}$ are roughly consistent within statistical errors, except at 7.7 GeV, where dv_1/dy for $\bar{\Lambda}$ shows a large deviation from \bar{p} . Of course, both statistical and systematic errors are especially large for antibaryons at 7.7 GeV.

Figure 5.7 shows dv_1/dy versus beam energy for K^\pm and K_S^0 . The dv_1/dy for K^\pm and K_S^0 are negative and similar in magnitude to π^\pm at BES energies. Another noteworthy observation is that at all BES energies, dv_1/dy for K_S^0 is in between K^+ and K^- within errors.

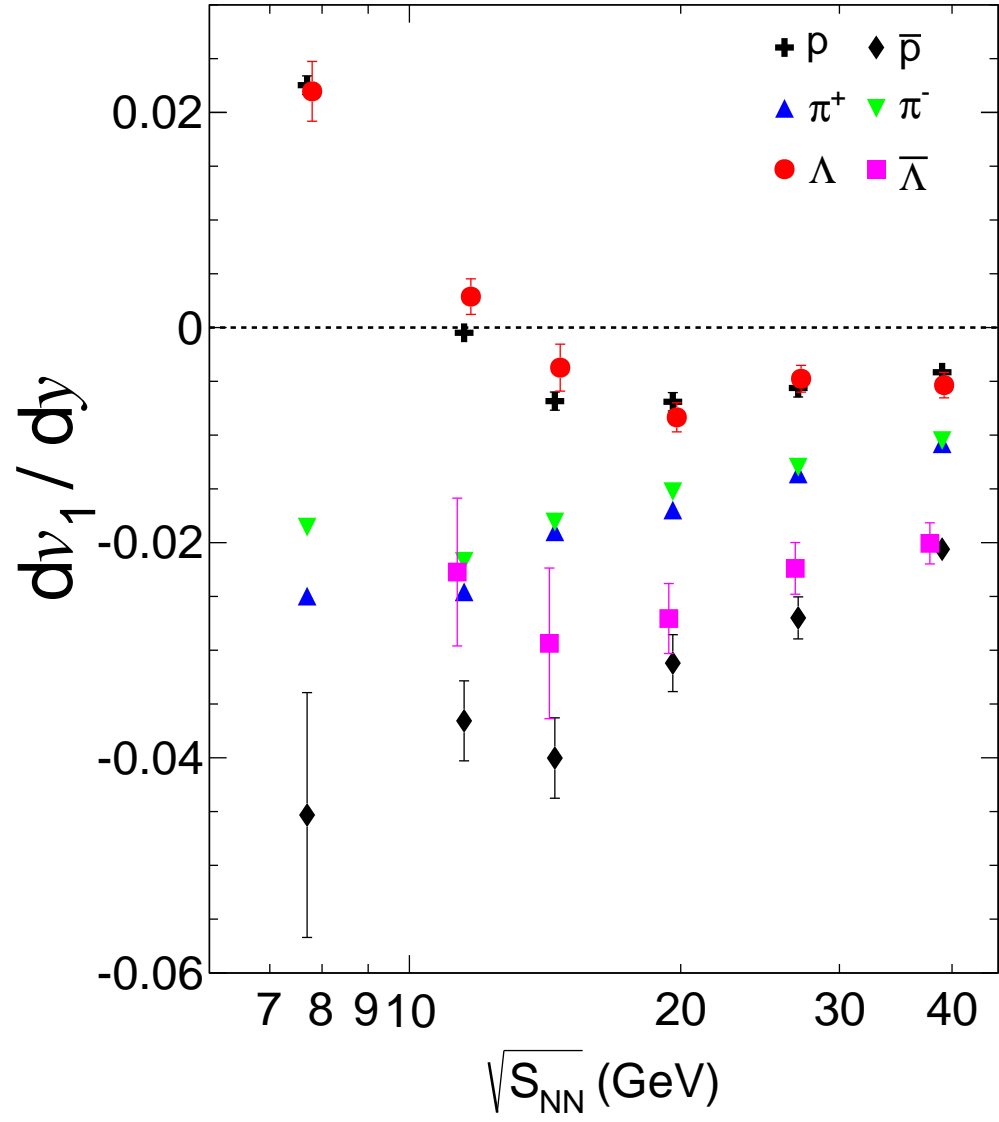


Figure 5.6: dv_1/dy near mid-rapidity as a function of beam energy for p , \bar{p} , π^\pm , Λ and $\bar{\Lambda}$ for 10-40% central Au+Au collisions. The dv_1/dy for $\bar{\Lambda}$ at 7.7 GeV is -0.13 ± 0.02 , which lies off-scale, below the lower end of the vertical axis. Error bars are statistical.

Table 5.1: Summary of the event statistics used in UrQMD simulations. For reference, real event statistics are also shown.

Energy	UrQMD Events ($\times 10^6$)	Real Events ($\times 10^6$)
7.7	0.78	4
11.5	0.76	12
14.5	0.74	20
19.6	0.28	36
27	0.28	70
39	0.28	130

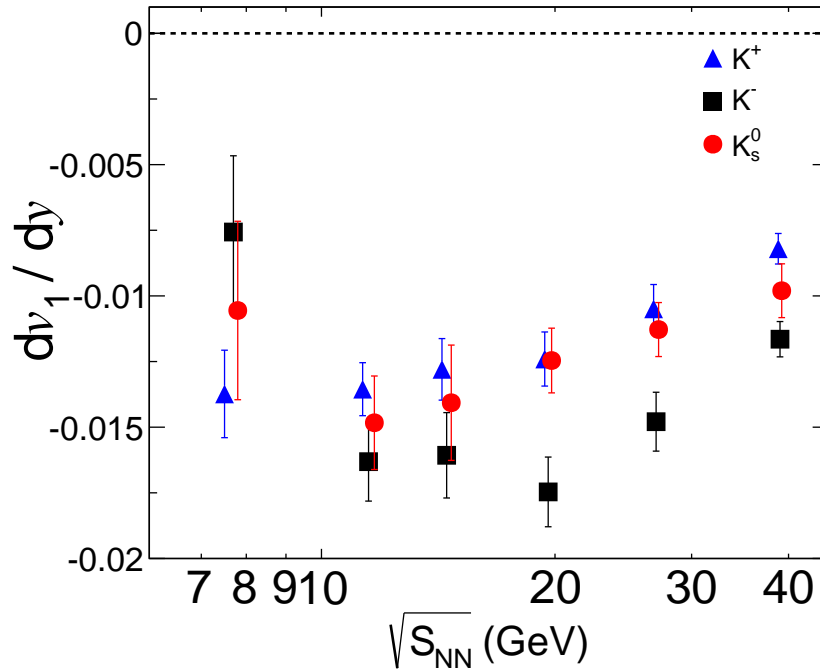


Figure 5.7: dv_1/dy near mid-rapidity as function of beam energy for K^+ , K^- and K_S^0 for 10-40% central Au+Au collisions. Error bars are statistical.

5.2.1.2 UrQMD Model Calculations

In this dissertation, I am using UrQMD version 3.3p2. Table 5.1 summarizes the available UrQMD event statistics, which were generated with default UrQMD settings. Particles are identified using the particle ID provided by UrQMD, without any p_T quality cuts applied. The centrality of UrQMD events is assigned with the aid of particle multiplicity, as in experiment.

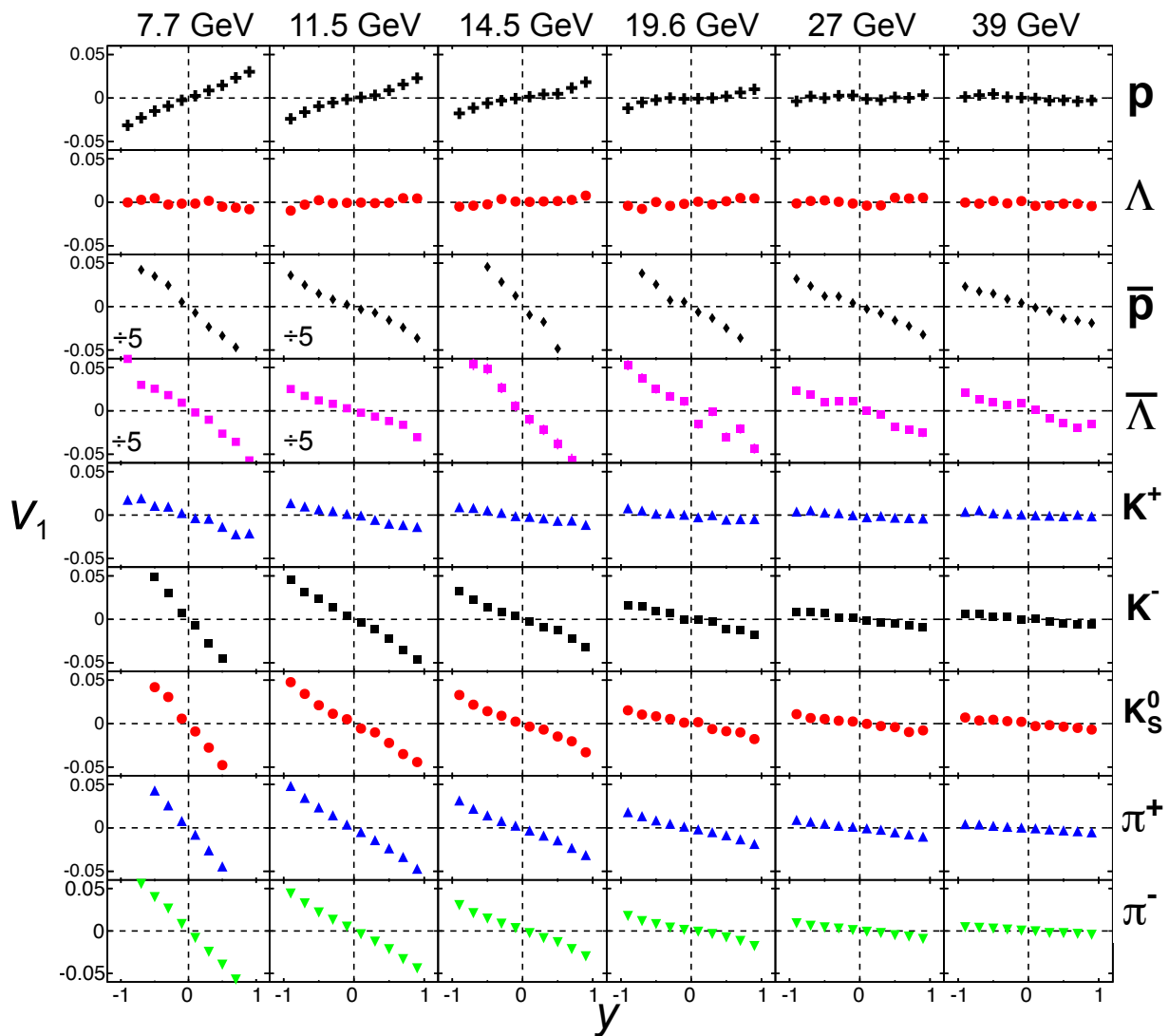


Figure 5.8: Directed flow as a function of rapidity for p , Λ , \bar{p} , $\bar{\Lambda}$, K^\pm , K_s^0 and π^\pm for 10-40% central UrQMD Au+Au collisions. Error bars are statistical. The v_1 magnitude is exceptionally large for \bar{p} and $\bar{\Lambda}$ at 7.7 and 11.5 GeV, and therefore for only for those four panels, v_1 and its errors are divided by 5 to fit on the common vertical scale.

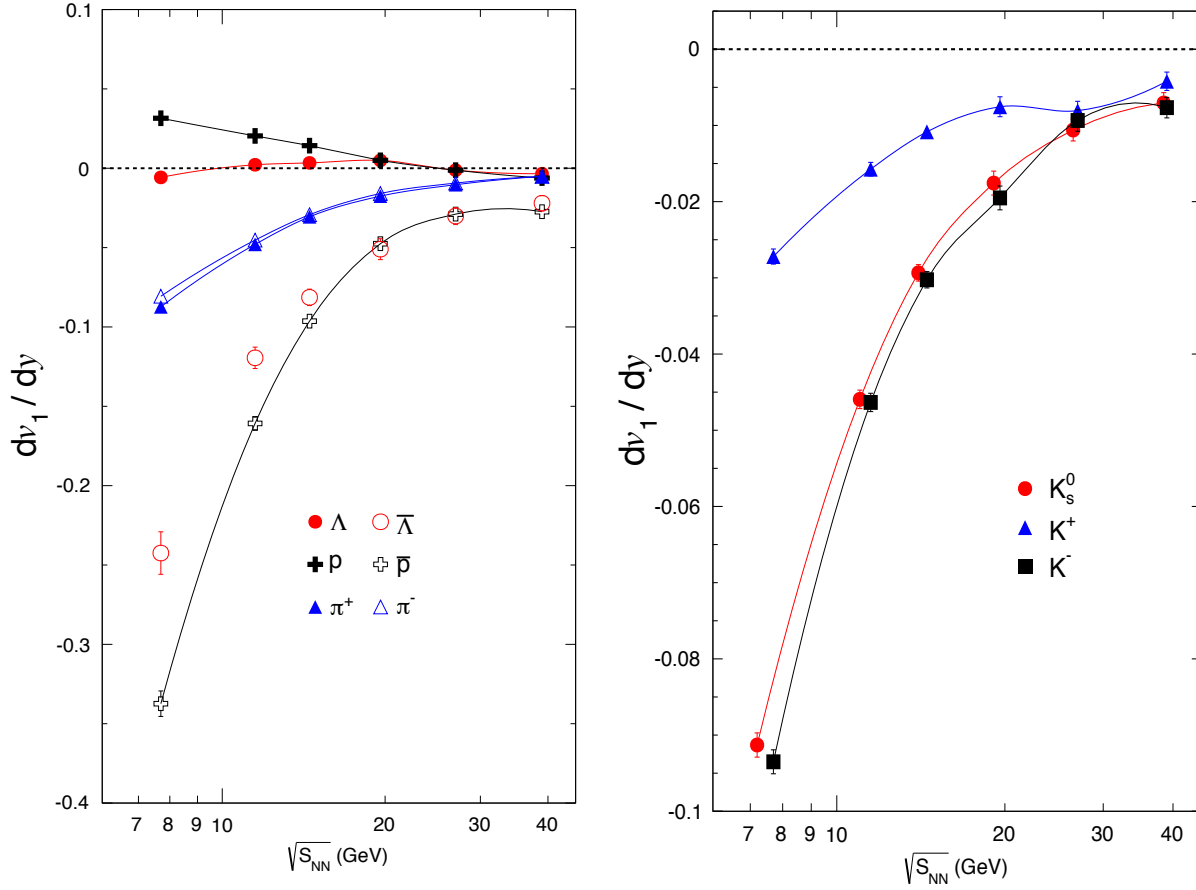


Figure 5.9: The left panel shows dv_1/dy near mid-rapidity as function of beam energy for p , \bar{p} , π^\pm , Λ and $\bar{\Lambda}$ from UrQMD events for 10-40% central Au+Au collisions. Similarly, the right panel is for K^\pm and K_S^0 . Error bars are statistical.

Figure 5.8 shows v_1 as a function of rapidity (y), from UrQMD events at all BES energies and for all nine particle species at 10-40% centrality. The left panel of Figure 5.9 shows dv_1/dy for Λ , $\bar{\Lambda}$, p , \bar{p} and π^\pm , as a function of beam energy for 10-40% centrality, while the right panel shows the same for K^\pm and K_S^0 . In general, UrQMD shows larger v_1 magnitude for all the particles and for all energies. For protons, dv_1/dy shows a sign change, but no minimum is observed as in the data. Λ shows nearly zero dv_1/dy for all energies, while $\bar{\Lambda}$ shows always a strongly negative dv_1/dy . Charged pions and kaons show negative slope for all BES energies, and the slope of K_S^0 is consistent with K^- for UrQMD events.

5.2.1.3 Systematic Uncertainty Study

A detailed explanation of the procedure for study of systematic uncertainties is given in Section 4.4.3. This section presents results from that systematic study. For example, at beam energies of 11.5 and 39 GeV, the systematic error in v_1 versus y is shown in Figures 5.10, 5.11, 5.12 and 5.13 for all nine particle types studied. For 11.5 GeV and the rest of the energies, \bar{p} and $\bar{\Lambda}$ show large systematic error. For the other particle species, systematic errors are comparable to statistical errors. For example, at beam energies of 11.5 and 39 GeV, the variation from the default dv_1/dy arising from various sources of systematic error are presented in Figure 5.14 for Λ , $\bar{\Lambda}$, and K_S^0 . Similarly, for the example of the beam energy of 11.5 GeV, systematic errors for particle types p , \bar{p} , π^\pm and K^\pm presented in Figure 5.14. A unique identifier called “cut number” is assigned to each source of possible systematic error to identify it in the graph. Cut number zero corresponds to the default (optimum) combination of quality cuts. In this study, the effect of varying p_T cuts from the default (optimum) value is also studied, but for reasons explained in Section 4.4.3, this source is not included as part of the total systematic error. The final systematic error and statistical error are indicated by a red data point at the far right side of Figures 5.14 and 5.15. For Λ and $\bar{\Lambda}$, additional contributions from event and track quality cuts and from $V0$ vertex cuts are also separately studied. This study shows that a larger contribution to the final systematic error comes from event and track quality cuts compared to $V0$ vertex selection cuts.

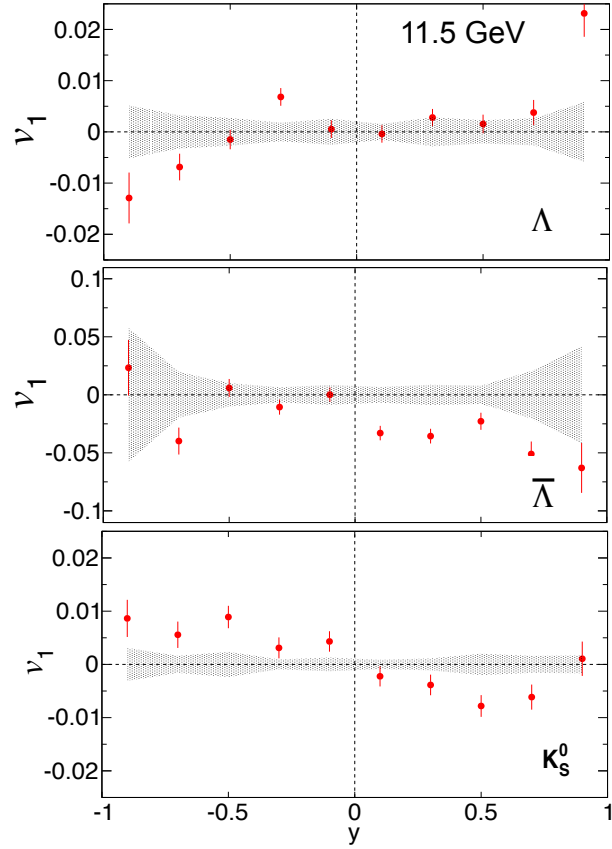


Figure 5.10: Error from systematic variations is shown by the shaded band for v_1 vs. y , for particles Λ , $\bar{\Lambda}$ and K_S^0 , in 10-40% central collisions at a beam energy of 11.5 GeV.

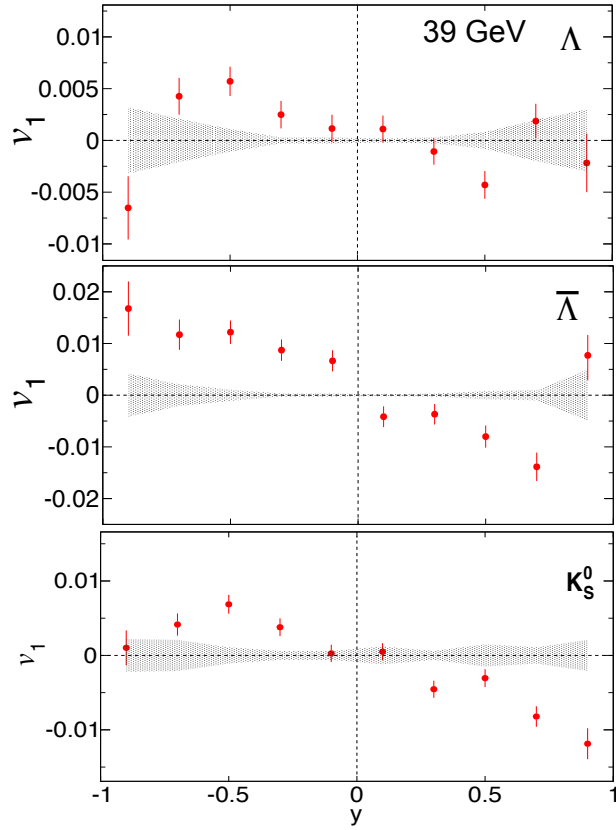


Figure 5.11: Error from systematic variations is shown by the shaded band for v_1 vs. y , for particles Λ , $\bar{\Lambda}$ and K_S^0 , in 10-40% central collisions at a beam energy of 39 GeV.

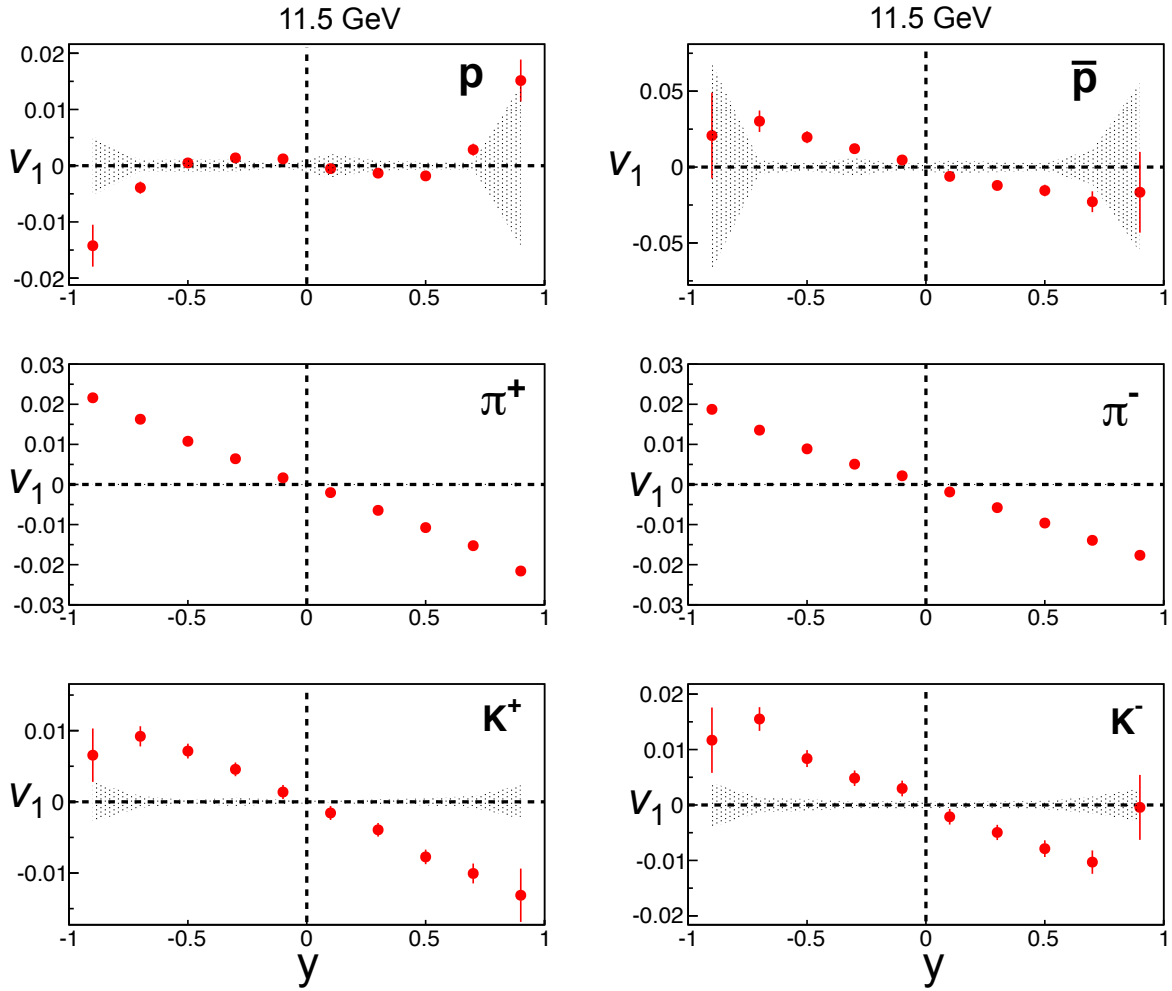


Figure 5.12: Error from systematic variations is shown by the shaded band for v_1 vs. y , for particles p , \bar{p} , π^\pm and K^\pm , in 10-40% central collisions at a beam energy of 11.5 GeV. The systematic error for π^\pm is small and is not visible on the scale of this plot.

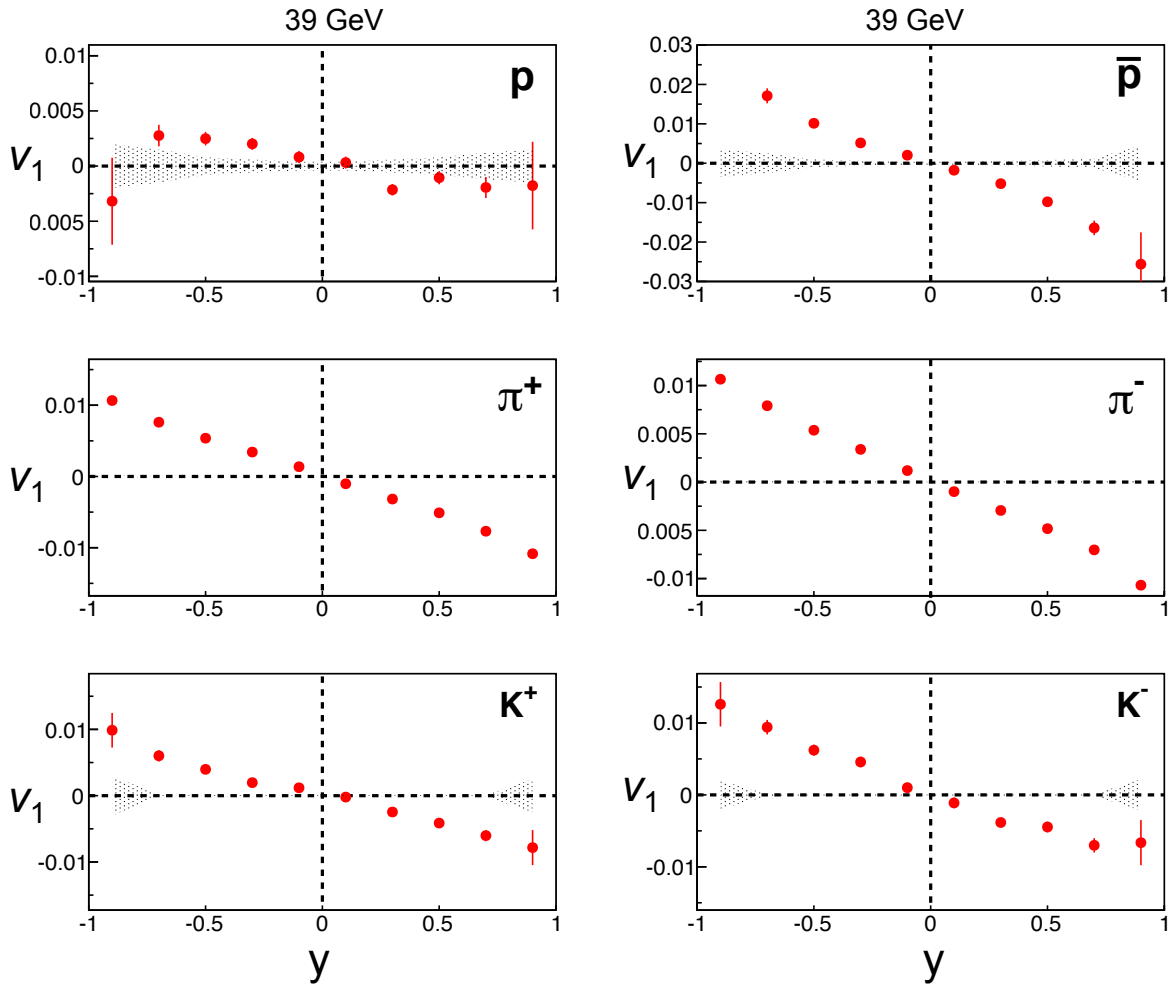


Figure 5.13: Error from systematic variations is shown by the shaded band for v_1 vs. y , for particles p , \bar{p} , π^\pm and K^\pm , in 10-40% central collisions at a beam energy of 39 GeV. The systematic error for π^\pm is small and is not visible on the scale of this plot.

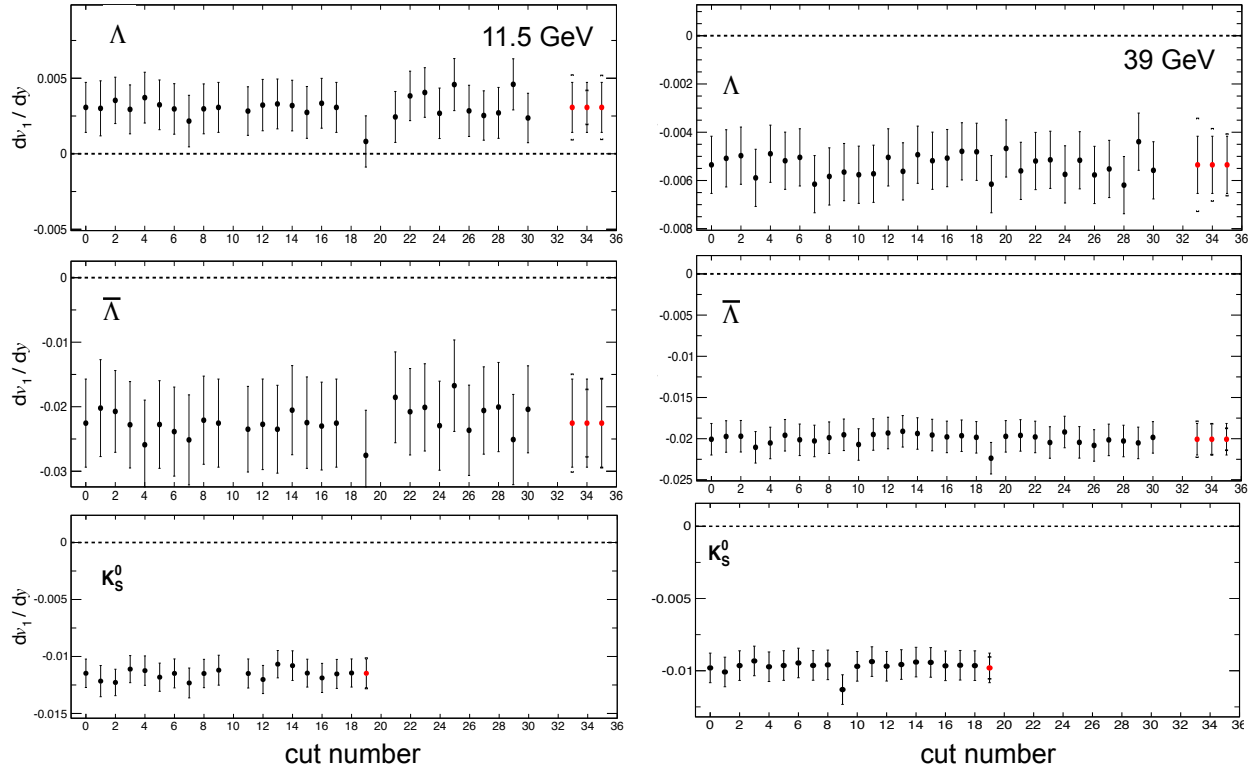


Figure 5.14: The effect from different sources of systematic error is shown for dv_1/dy from 10-40% central collisions at a beam energy of 11.5 GeV on left and of 39 GeV on right. The cut number is defined in Table 4.4 and 4.5 for Λ and $\bar{\Lambda}$ baryons, and in Table 4.6 and 4.7 for K_S^0 . For Λ and $\bar{\Lambda}$, cut number 33 is the final data point with systematic and statistical errors, cut number 34 corresponds to systematic errors from event and track quality cuts, and cut number 35 includes only $V0$ systematic errors. For K_S^0 , cut number 19 is the final data point with systematic and statistical errors.

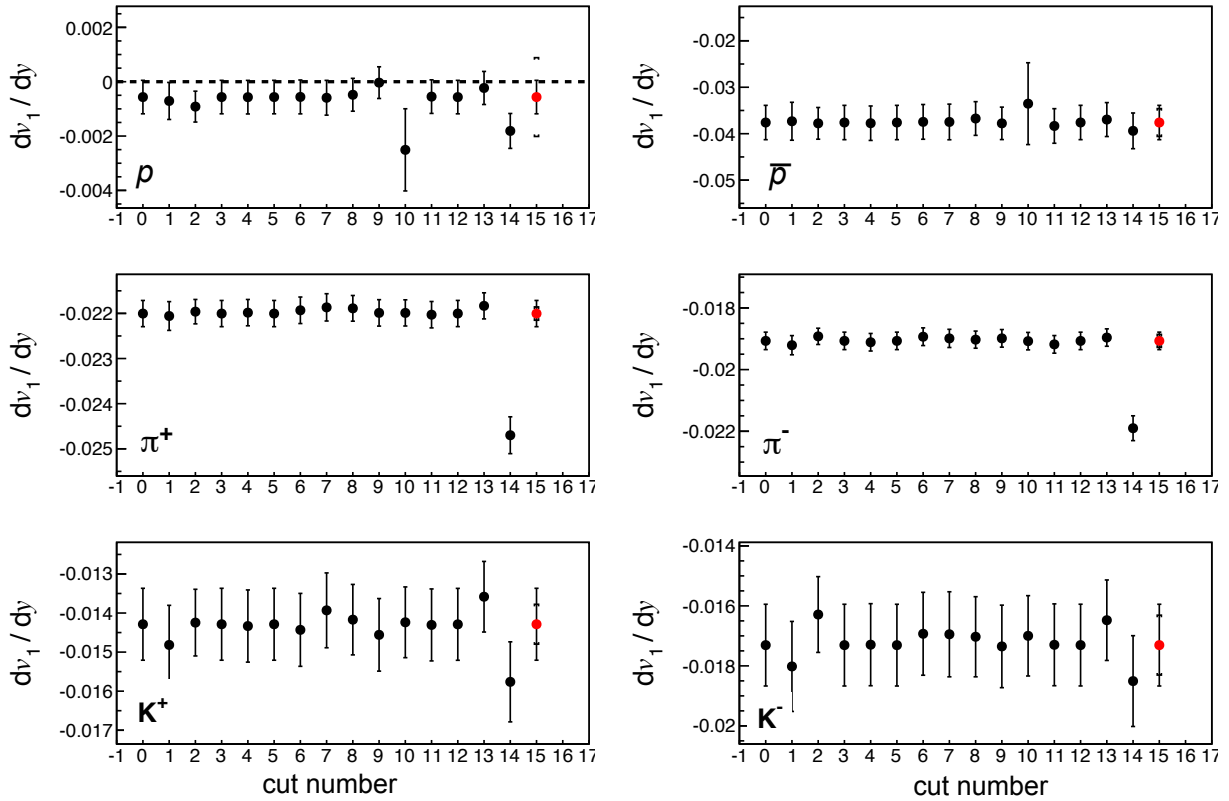


Figure 5.15: The effect from different sources of systematic error is shown for dv_1/dy from 10-40% central collisions at a beam energy of 11.5 GeV. The cut number is defined in Table 4.8 for p and \bar{p} , and in Table 4.9 for π^\pm and K^\pm . Cut number 15 is the final data point with systematic and statistical errors.

5.2.1.4 Net-Particle Directed Flow

Directed flow near midrapidity has contributions both from protons produced as baryon-antibaryon pairs in the hot participant zone, as well from protons associated with conserved baryon number transported from the initial-state nuclei towards midrapidity by the stopping process of the nuclear collision. We want to distinguish between these two distinct mechanisms, and a measurement of net-baryon flow would help us to do that. In our experiment, it is not possible to directly identify net baryons, and therefore net protons are used as a proxy for net baryons. In order to roughly estimate the flow contribution associated with the transported baryon number, we hypothesize that quarks in antiprotons and in produced protons have roughly the same

directed flow. This hypothesis is suggested by the observation that the measured v_1 for π^+ and π^- [49], for K^+ and K^- , for \bar{p} and $\bar{\Lambda}$ are very similar. Therefore, the following definition of net-proton v_1 is our best estimate of a proxy observable for the transported component,

$$[v_1(y)]_p = r(y)[v_1(y)]_{\bar{p}} + (1 - r(y)) [v_1(y)]_{\text{net-}p}, \quad (5.1)$$

where $r(y)$ is the rapidity-dependent ratio of observed antiprotons to protons. Then we define net- Λ and net-kaon v_1 using the same formula, with p and \bar{p} replaced by Λ and $\bar{\Lambda}$ for net- Λ flow and p and \bar{p} replaced by K^+ and K^- for net-kaon flow, respectively. Figure 5.16 shows net-proton, net- Λ and net-kaon results. The net-particle dv_1/dy results are consistent for protons and Λ s, but dv_1/dy for net kaons strongly deviates from the other two cases for beam energies less than 14.5 GeV. The reason for the latter pattern is not yet understood.

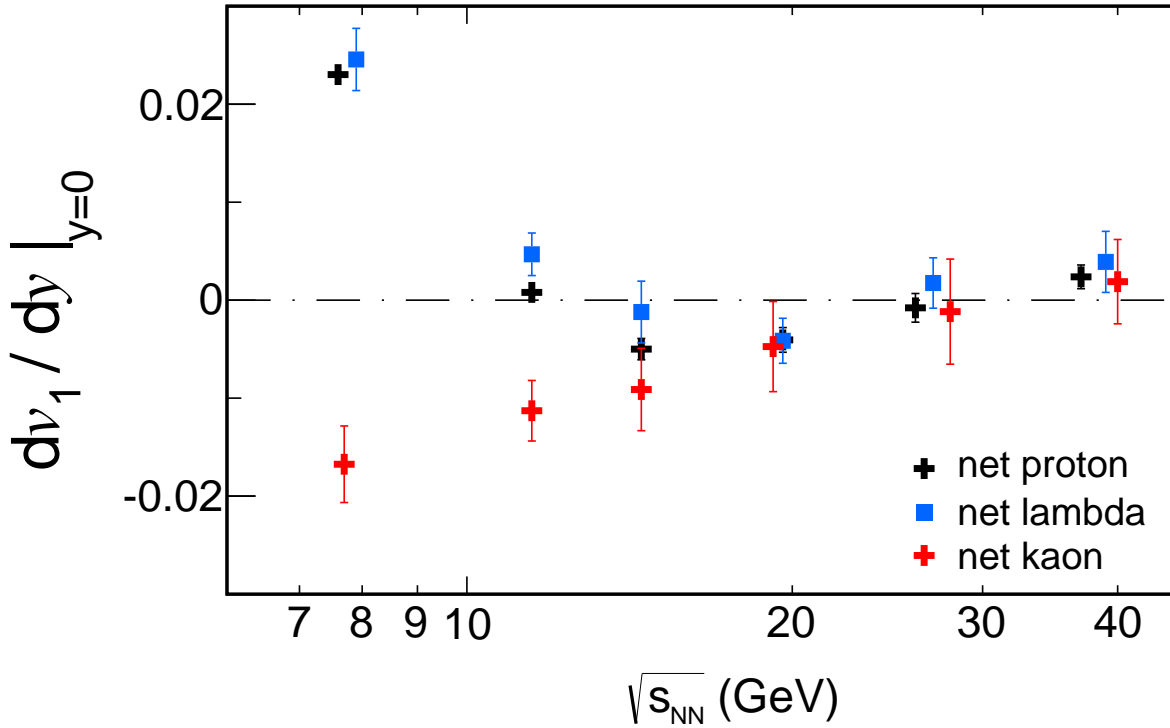


Figure 5.16: dv_1/dy near mid-rapidity at 10-40% centrality for net protons, net Λ s and net kaons.

5.2.1.5 Summary of Intermediate Centrality Results

Figure 5.17 shows the observed dv_1/dy as a function of beam energy as well as UrQMD calculations for p , Λ , \bar{p} , $\bar{\Lambda}$, and π^\pm at 10-40% centrality, with statistical and systematic errors. For p and Λ , UrQMD shows very poor agreement with data, especially at 19.6 GeV and below. UrQMD's v_1 slope for \bar{p} , $\bar{\Lambda}$, and π^\pm shows a qualitatively similar trend as data at higher energies, but strongly deviates at lower energies.

Figure 5.18 shows the same for particles K^\pm and K_s^0 . For K^\pm and K_s^0 , UrQMD's v_1 slope also shows a qualitatively similar trend as data at higher energies, but strongly deviates at lower energies.

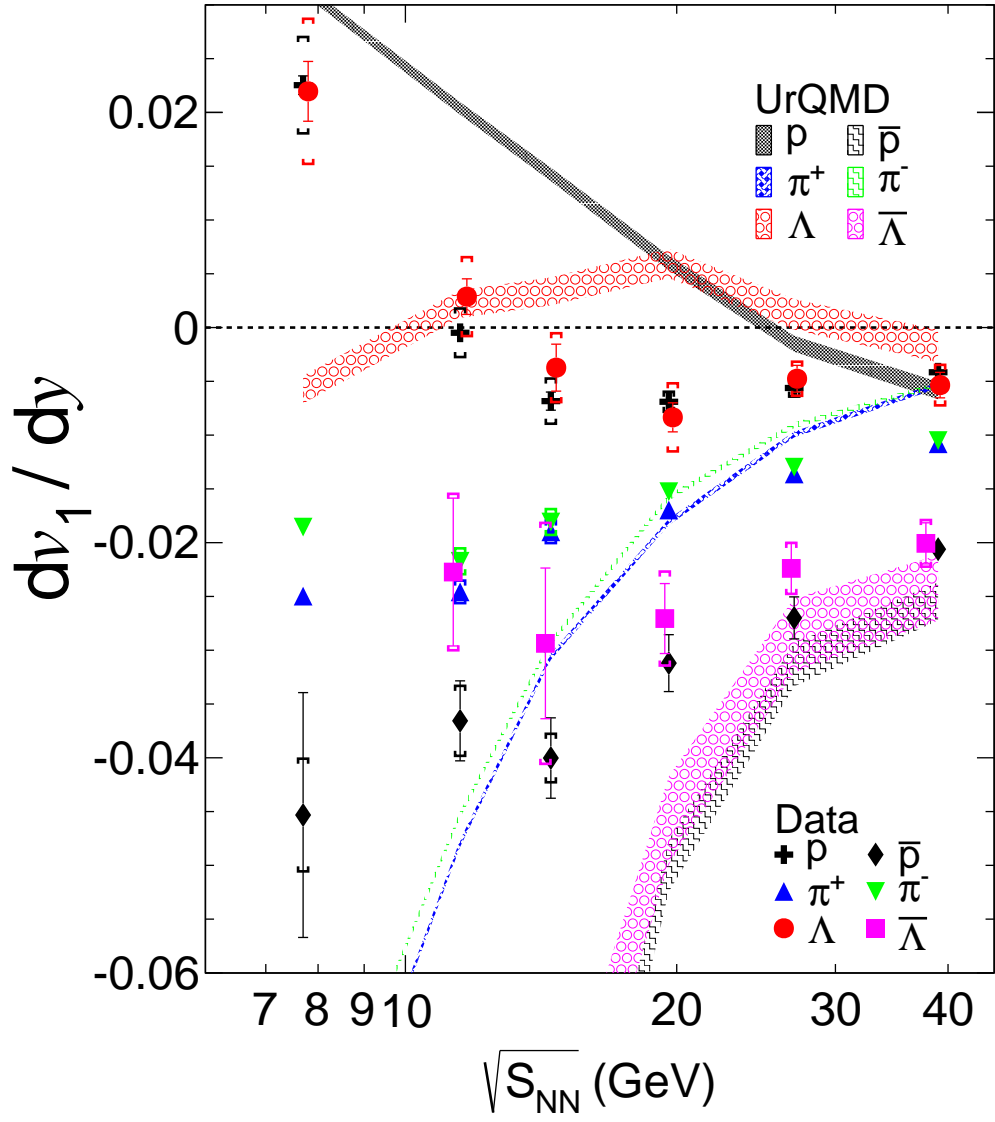


Figure 5.17: Slope of v_1 near mid-rapidity as a function of beam energy for protons, antiprotons, Λ , $\bar{\Lambda}$, and π^\pm for 10-40% central collisions. Solid data points show BES data and shaded bands show UrQMD calculations. The dv_1/dy for $\bar{\Lambda}$ at 7.7 GeV is -0.13 ± 0.02 , which lies off-scale, below the lower end of the vertical axis. Error bars are statistical, while caps show systematic errors.

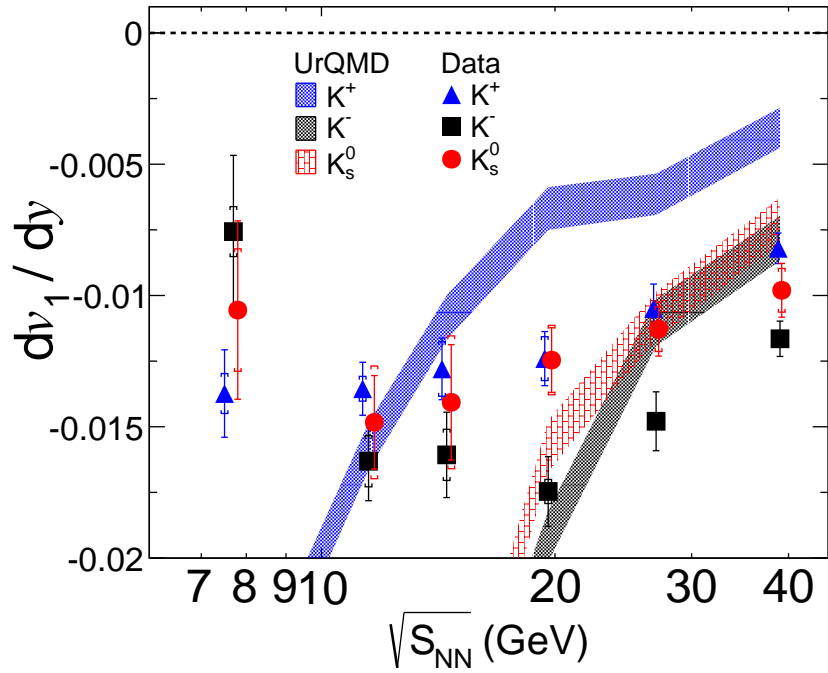


Figure 5.18: Slope of v_1 near mid-rapidity as a function of beam energy for K^\pm and K_s^0 for 10-40% central collisions. Solid data points show BES data and shaded bands show UrQMD calculations. Error bars are statistical, while caps show systematic errors.

5.2.2 Peripheral and Central Au+Au Collisions

Rapidity-dependent v_1 is shown in Figure 5.19 for central (0-10%) collisions, and in Figure 5.20 for peripheral (40-80%) collisions. In general, 0-10% centrality shows small and negative dv_1/dy compared to intermediate centrality. For peripheral collisions, in general the magnitude of dv_1/dy is larger than at intermediate centrality. Statistics for \bar{p} and $\bar{\Lambda}$ at 7.7 and 11.5 GeV are especially low, so a clear trend in dv_1/dy cannot be seen.

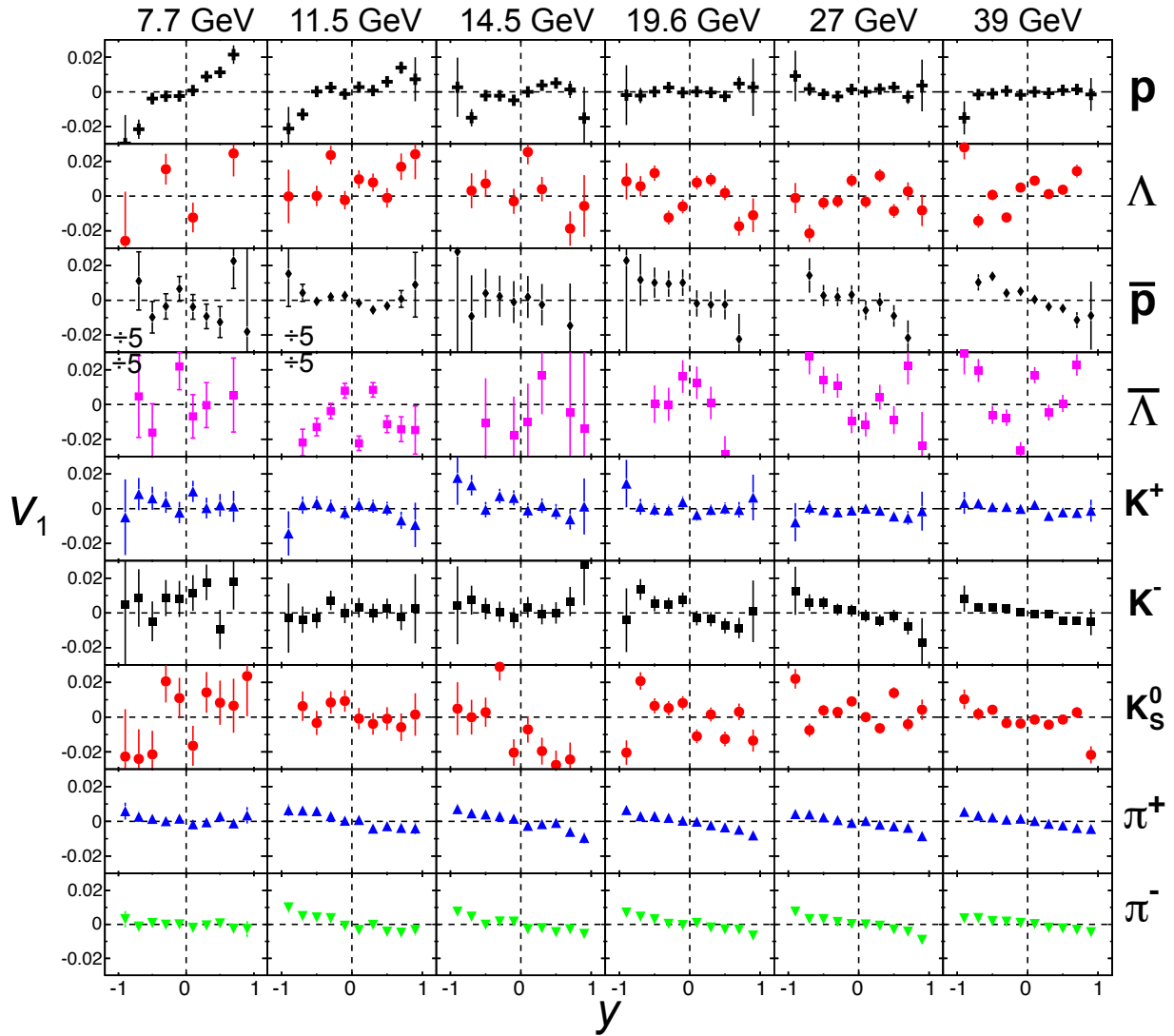


Figure 5.19: Directed flow (v_1) as a function of rapidity for p , Λ , \bar{p} , $\bar{\Lambda}$, K^\pm , K_s^0 and π^\pm in 0-10% centrality Au+Au collisions. Error bars are statistical. The v_1 magnitude is exceptionally large for \bar{p} and $\bar{\Lambda}$ at 7.7 and 11.5 GeV, and hence for only those panels, v_1 and its errors are divided by 5 to fit on the common vertical scale.

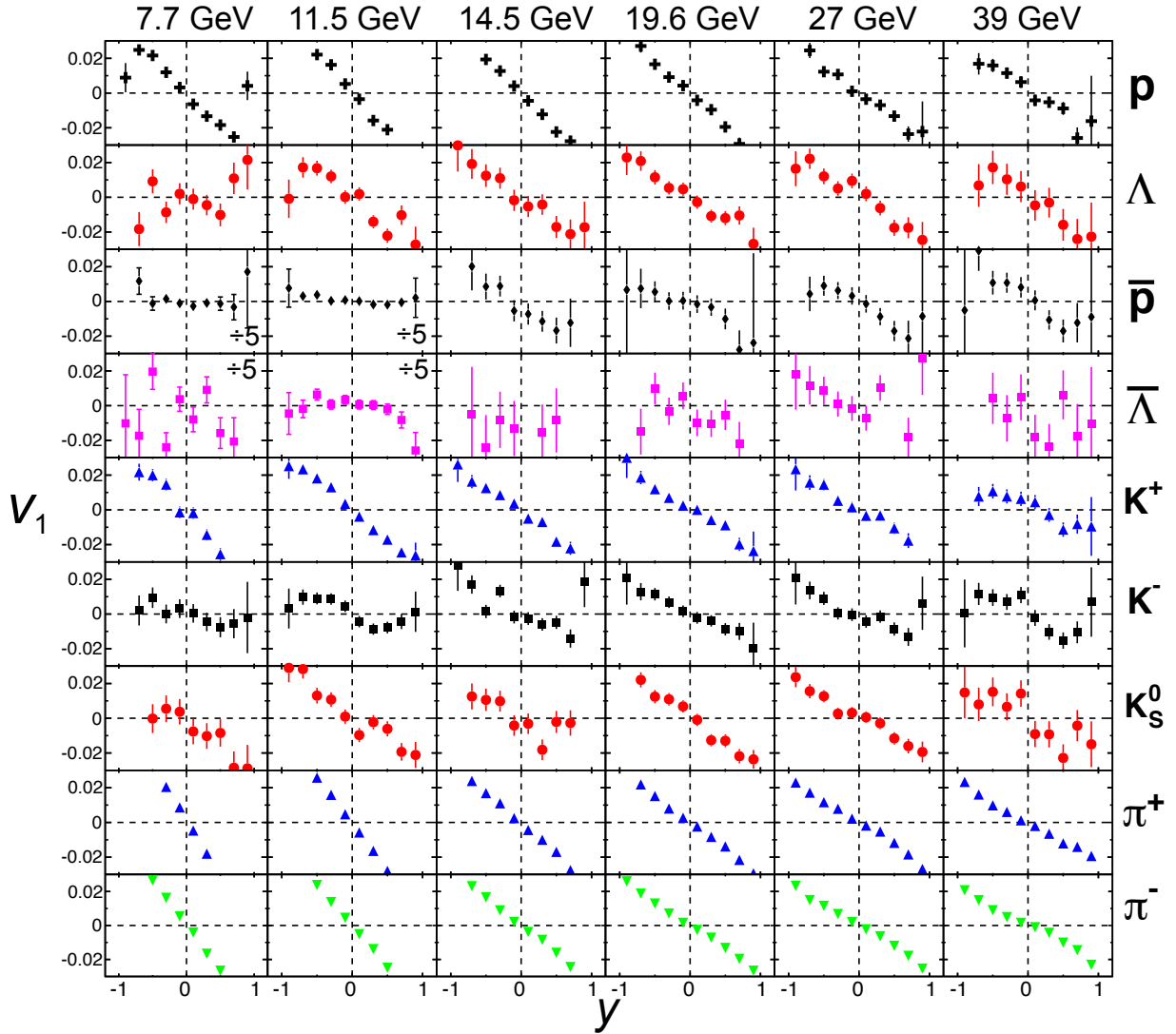


Figure 5.20: Directed flow (v_1) as a function of rapidity for p , Λ , \bar{p} , $\bar{\Lambda}$, K^\pm , K_s^0 and π^\pm in 40-80% centrality Au+Au collisions. Error bars are statistical. The v_1 magnitude is exceptionally large for \bar{p} and $\bar{\Lambda}$ at 7.7 and 11.5 GeV, and hence for only those panels, v_1 and its errors are divided by 5 to fit on the common vertical scale.

5.2.3 Different Definitions of Wide Centrality Bins

Centralities for Au+Au collisions are divided into nine bins as shown in Table 5.2. The intermediate centrality class that has already been studied in detail is a combination of three centrality bins: four, five and six. The effect of changing the upper and lower limit of the intermediate centrality class is investigated in Figure 5.21. It is seen that the qualitative trend of dv_1/dy

Table 5.2: Alternative groupings of coarse centrality bins.

Centrality Bin	Centrality Percentage	Default	Trail-1
0	70-80	Peripheral	Peripheral
1	60-70		Intermediate Centrality
2	50-60		
3	40-50		
4	30-40	Intermediate Centrality	Intermediate Centrality
5	20-30		
6	10-20	Central	Central
7	5-10		
8	0-5		

doesn't depend on the exact definition of the intermediate centrality interval, but the depth and significance of the minimum for baryons (p and Λ) changes with different definitions.

Overall, Figure 5.21 allows the study of Ref. [49] to be revisited with a new energy point close to the position of the minimum in proton directed flow, and with a new baryon species, among other enhancements. The evidence for the phenomenon called “collapse of directed flow” is significantly strengthened.

Figure 5.21 contains hints that the BES-I dataset for 14.5 GeV does not always lie on the smooth trend defined by the other BES energies, but the departure is still within errors. There are similar hints in other BES analysis, and one possible explanation is the added material of the Heavy Flavor Tracker close to the primary vertex. Further study of this issue is continuing.

When more statistics will available from BES-II running in 2019 and 2020 [16], then a clearer conclusion on all the physics topics considered in this dissertation will likely be reached.

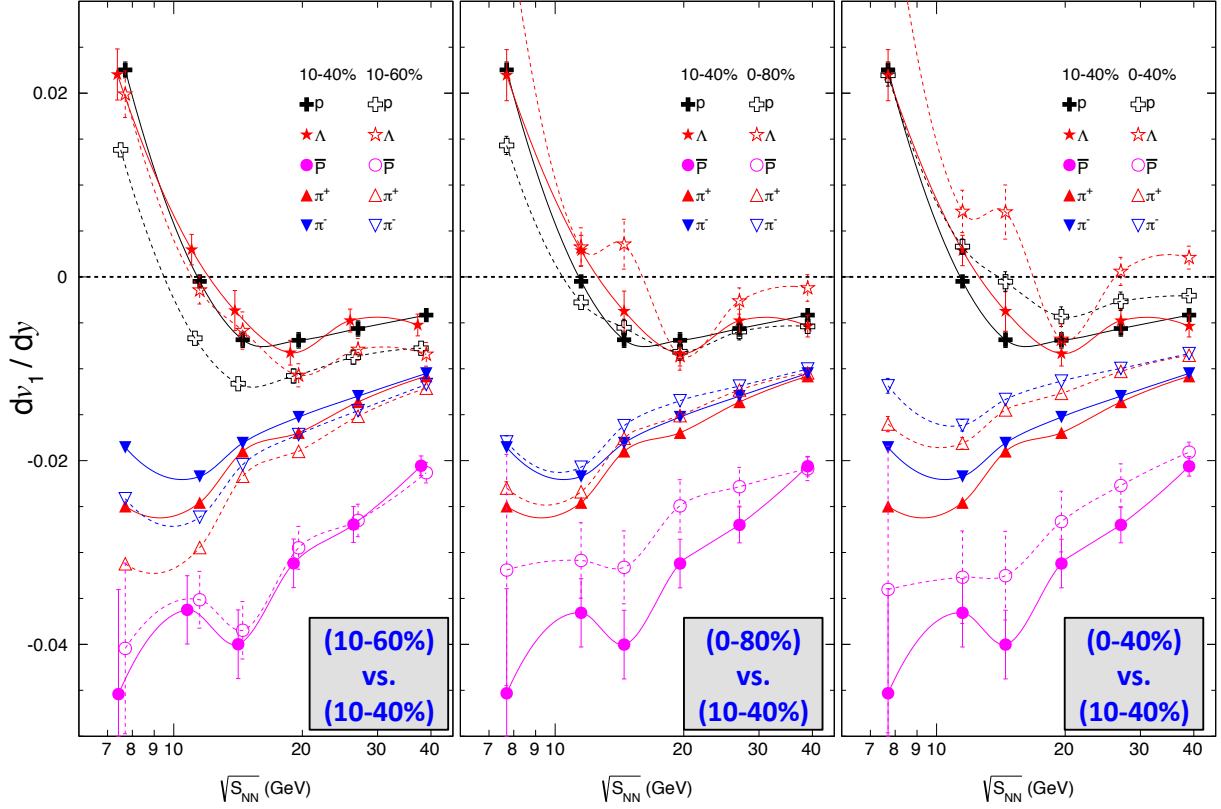


Figure 5.21: Comparison of dv_1/dy for different combinations of centrality bins with the default intermediate-centrality class. Error bars are statistical.

5.3 Centrality Dependence of Directed Flow

The strong centrality dependence of the event plane resolution requires us to calculate directed flow in narrow centrality bins, and then correct for the event plane resolution. During these steps, I have observed that dv_1/dy for the various particle species depends not only on the beam energy, but also on centrality for a given beam energy. The top panels of Figures 5.22, 5.23, 5.24, 5.25 show the centrality dependence of dv_1/dy for particles p , Λ , π^+ and π^- respectively. Results for \bar{p} and $\bar{\Lambda}$ are not discussed due to limited statistics. Protons, charged pions and Λ s shows strong centrality dependence at all beam energies. Furthermore, protons and Λ s show a sign change in dv_1/dy as a function of centrality at lower beam energies. However, these results are hampered by marginal statistics, especially for the most central and most peripheral collisions. The top panels of Figures 5.26, 5.27, 5.28 show the centrality

dependence of dv_1/dy for K^+ , K^- and K_S^0 , respectively. Notice that the measured dv_1/dy for K^+ shows a moderately strong centrality dependence, whereas K^- and K_S^0 tends to show a more flat distribution. With the possible exception of charged pions, the centrality dependence of dv_1/dy is hampered by poor statistics. With the greatly improved statistics of BES-II running in 2019 and 2020, we can expect more promising results. The bottom panels of the above figures show UrQMD, where p shows strong centrality dependence for almost all the energies, while centrality dependence for Λ is much weaker in UrQMD calculations. Charged pions, charged kaons and K_S^0 from UrQMD show very weak centrality dependence at most of the studied beam energies.

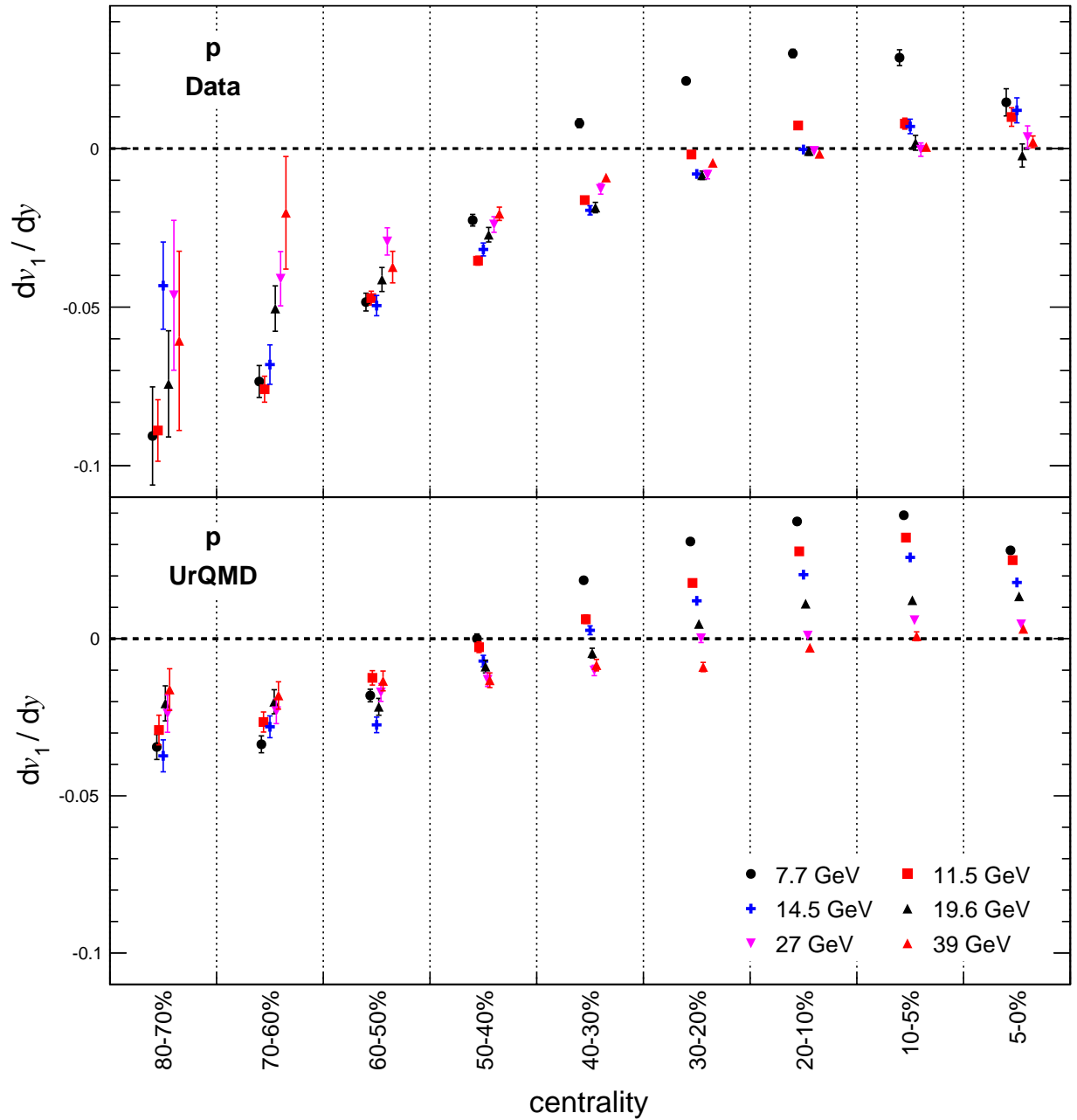


Figure 5.22: dv_1/dy near midrapidity as a function of centrality for p . Top panel from STAR data and bottom panel is from UrQMD. Error bars are statistical. In general, systematic errors are comparable to statistical errors, but are omitted to reduce clutter.

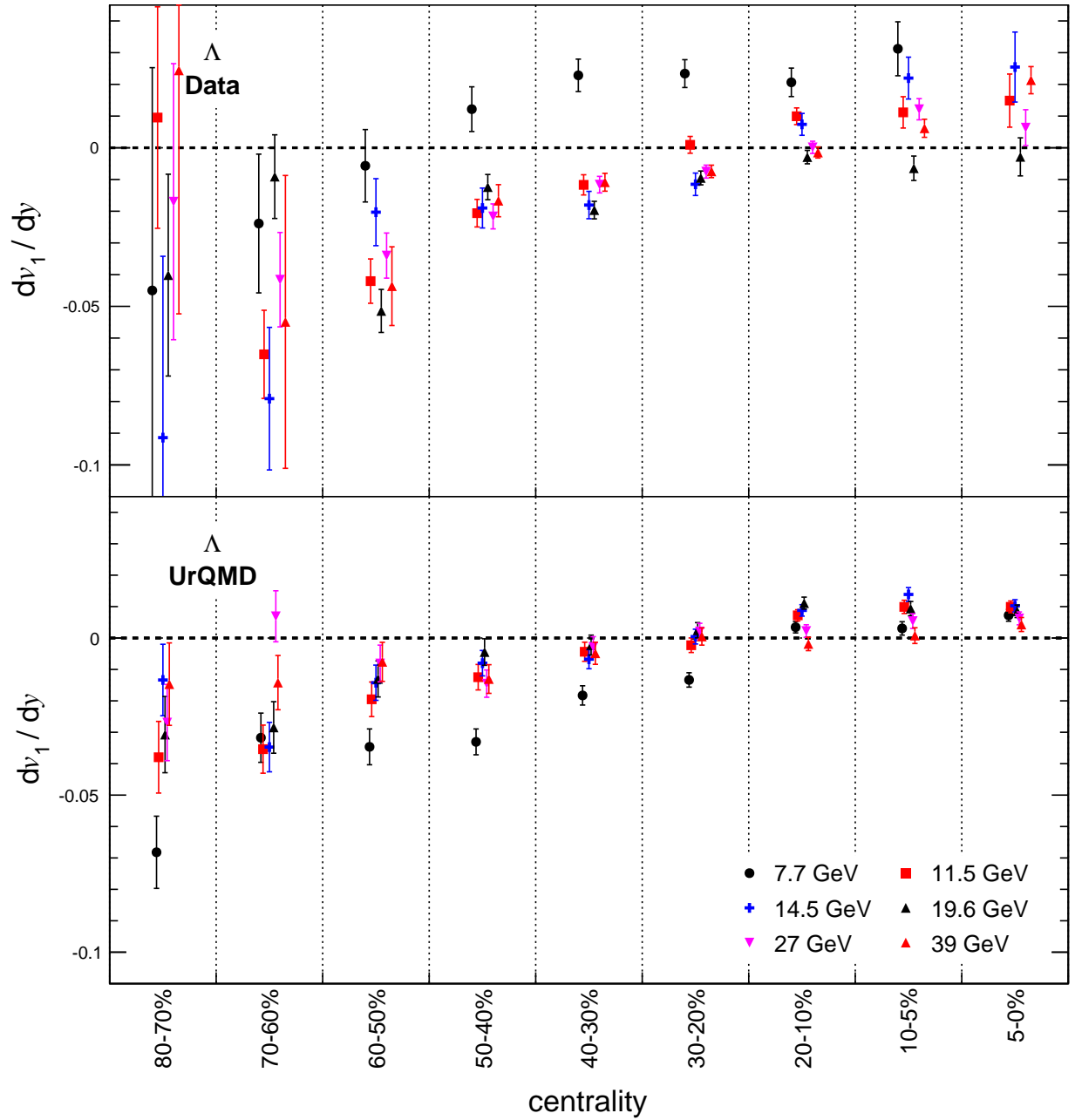


Figure 5.23: dv_1/dy near midrapidity as a function of centrality for Λ . Top panel from STAR data and bottom panel is from UrQMD. Error bars are statistical. In general, systematic errors are comparable to statistical errors, but are omitted to reduce clutter.

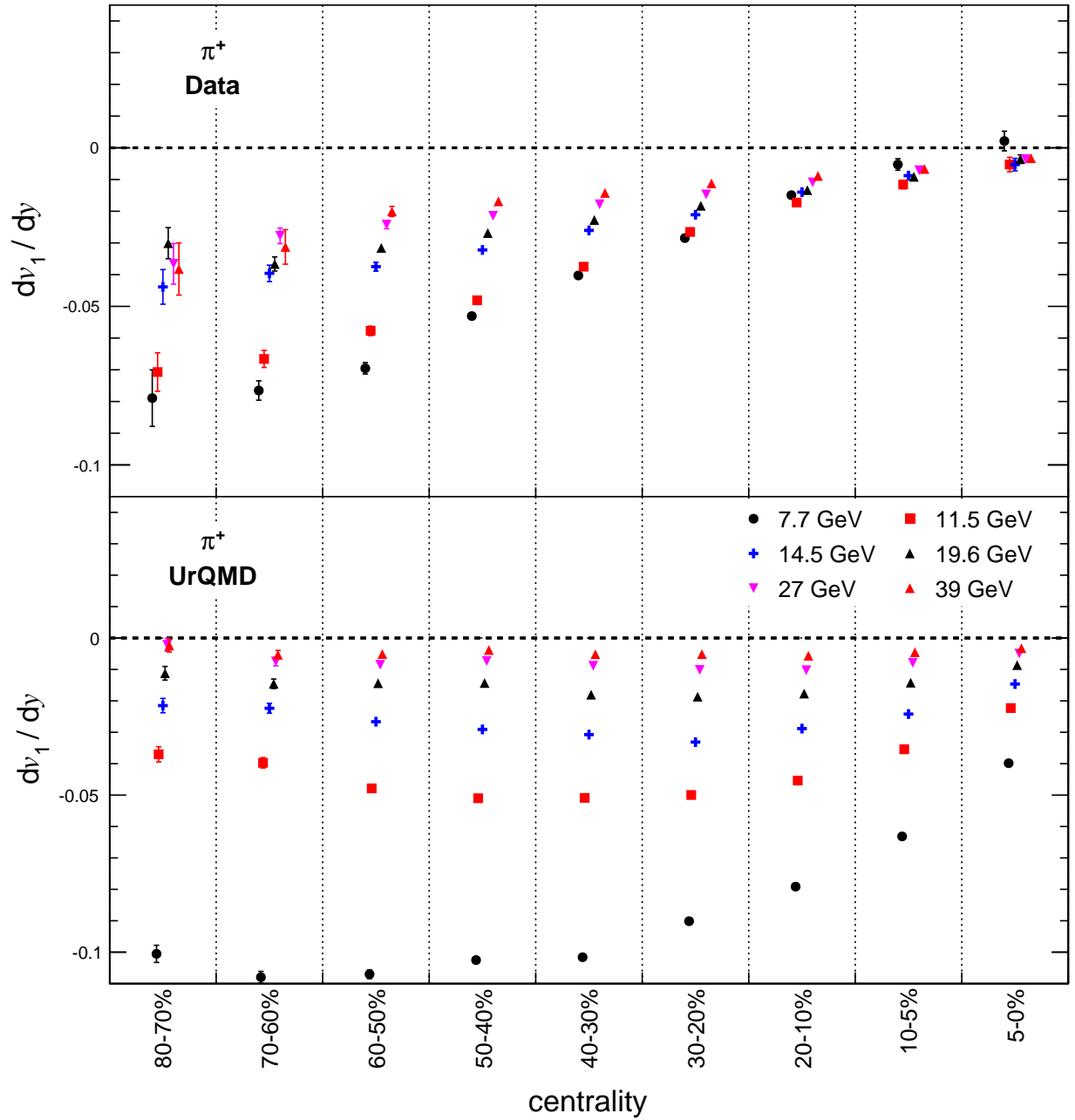


Figure 5.24: dv_1/dy near midrapidity as a function of centrality for π^+ . Top panel from STAR data and bottom panel is from UrQMD. Error bars are statistical. In general, systematic errors are comparable to statistical errors, but are omitted to reduce clutter.

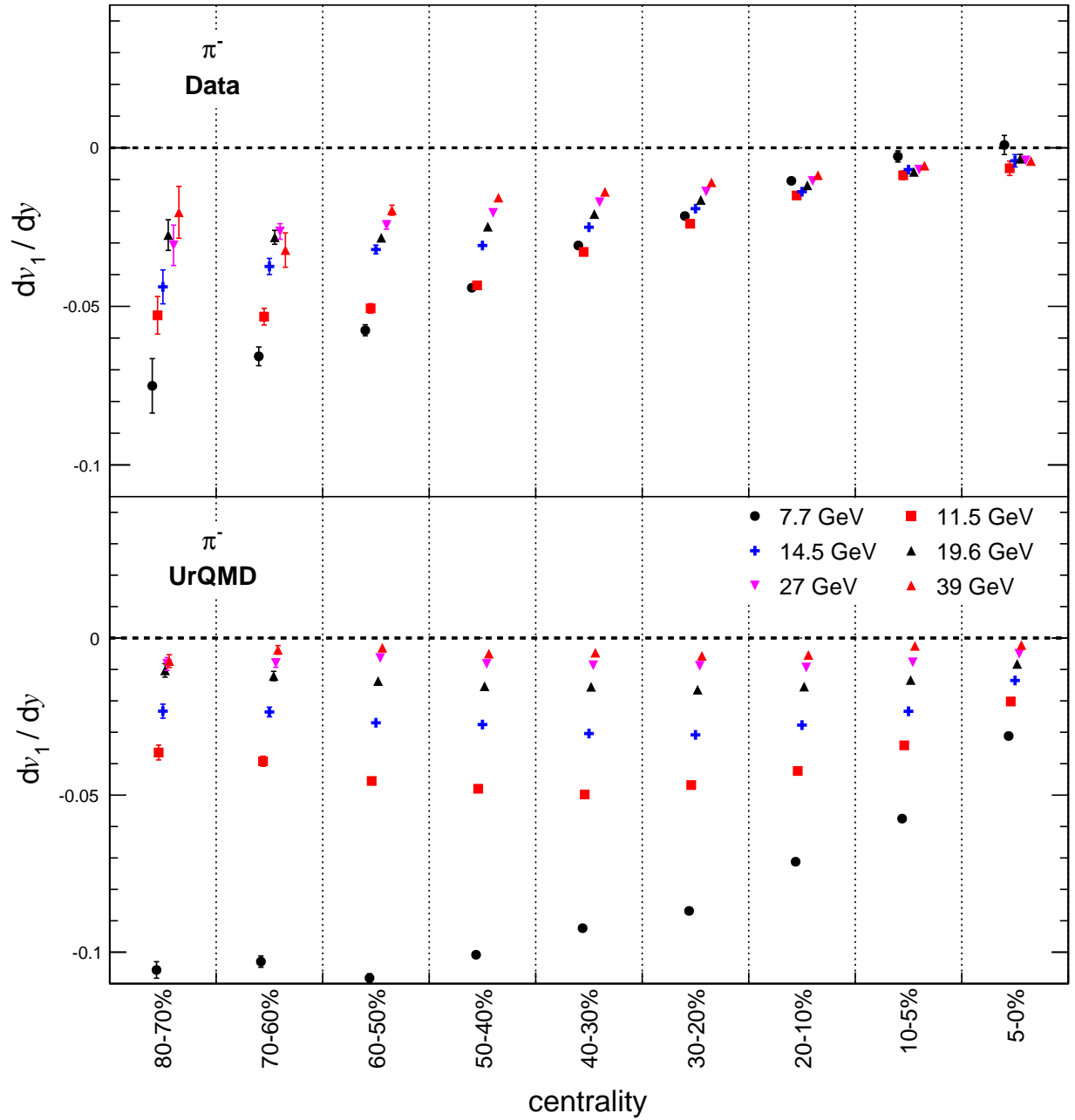


Figure 5.25: dv_1/dy near midrapidity as a function of centrality for π^- . Top panel from STAR data and bottom panel is from UrQMD. Error bars are statistical. In general, systematic errors are comparable to statistical errors, but are omitted to reduce clutter.

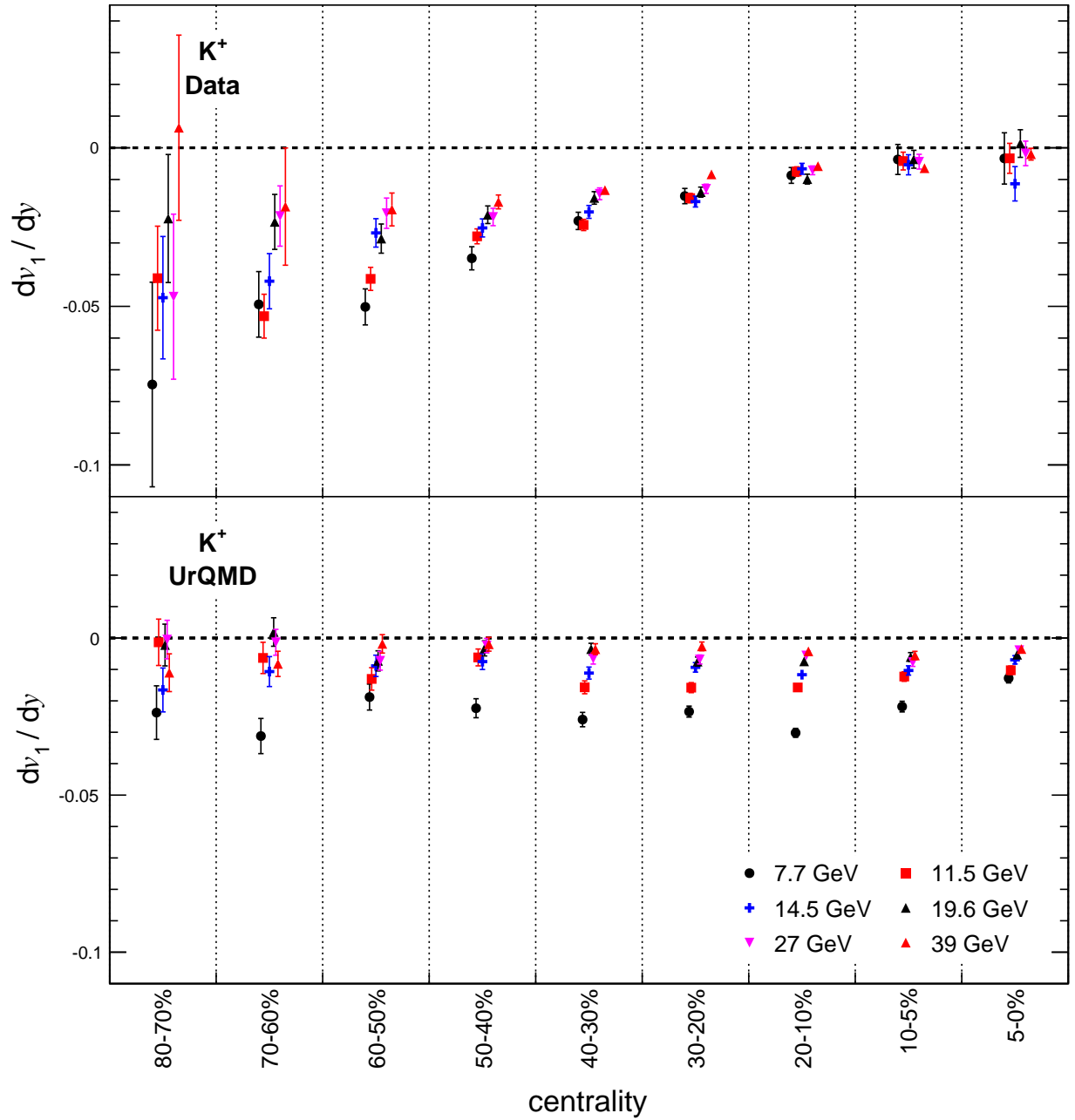


Figure 5.26: dv_1/dy near midrapidity as a function of centrality for K^+ . Top panel from STAR data and bottom panel is from UrQMD. Error bars are statistical. In general, systematic errors are comparable to statistical errors, but are omitted to reduce clutter.

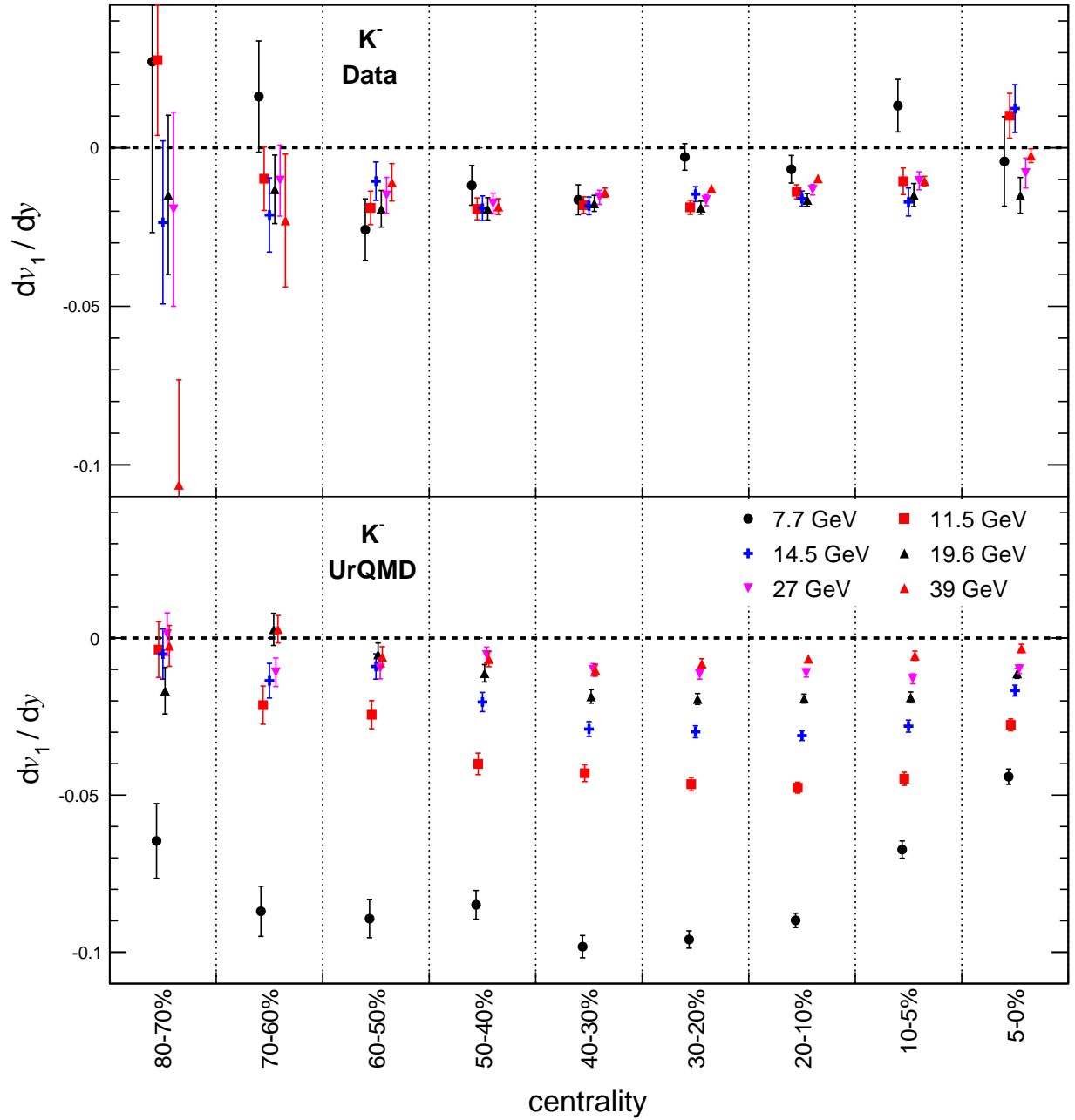


Figure 5.27: dv_1/dy near midrapidity as a function of centrality for K^- . Top panel from STAR data and bottom panel is from UrQMD. Error bars are statistical. In general, systematic errors are comparable to statistical errors, but are omitted to reduce clutter.

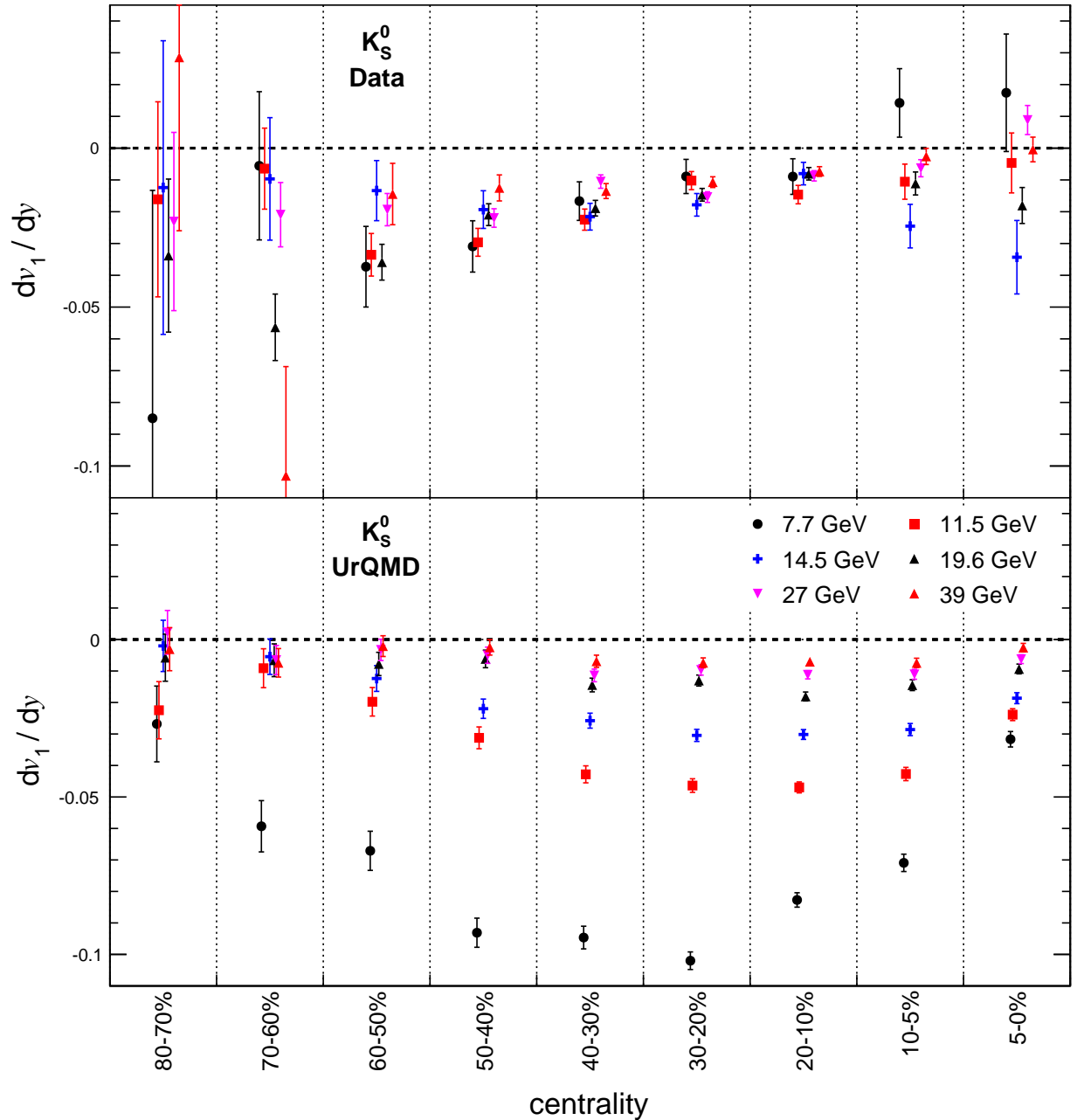


Figure 5.28: dv_1/dy near midrapidity as a function of centrality for K_S^0 . Top panel from STAR data and bottom panel is from UrQMD. Error bars are statistical. In general, systematic errors are comparable to statistical errors, but are omitted to reduce clutter.

The systematic error calculation for centrality dependence of dv_1/dy is very similar to the beam-energy dependence as explained in Section 4.4.3. Parameters and cuts are varied for the detector acceptance and the efficiencies. The systematic error in centrality for dv_1/dy is

shown in Figures 5.29, 5.30 for p , Λ , π^+ and π^- at representative beam energies of 11.5 and 39 GeV respectively. Similarly, Figures 5.29 and 5.30 show the same for K^\pm and K_S^0 at representative beam energies of 11.5 and 39 GeV, respectively. Point-by-point systematic errors are comparable to statistical errors for all particle species at all beam energies.

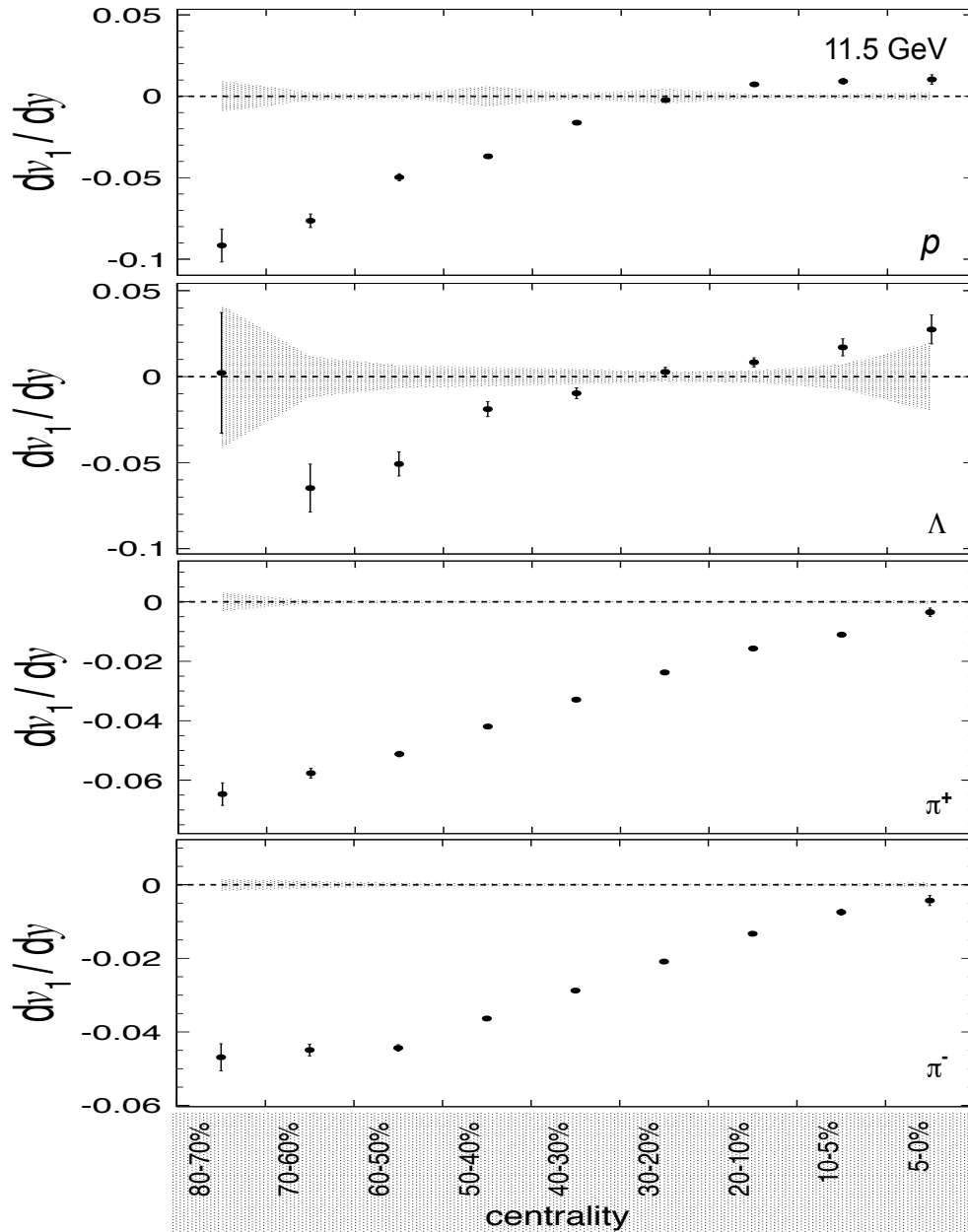


Figure 5.29: Systematic error for dv_1/dy as a function of centrality is shown for p , Λ , π^+ and π^- at a beam energy of 11.5 GeV.

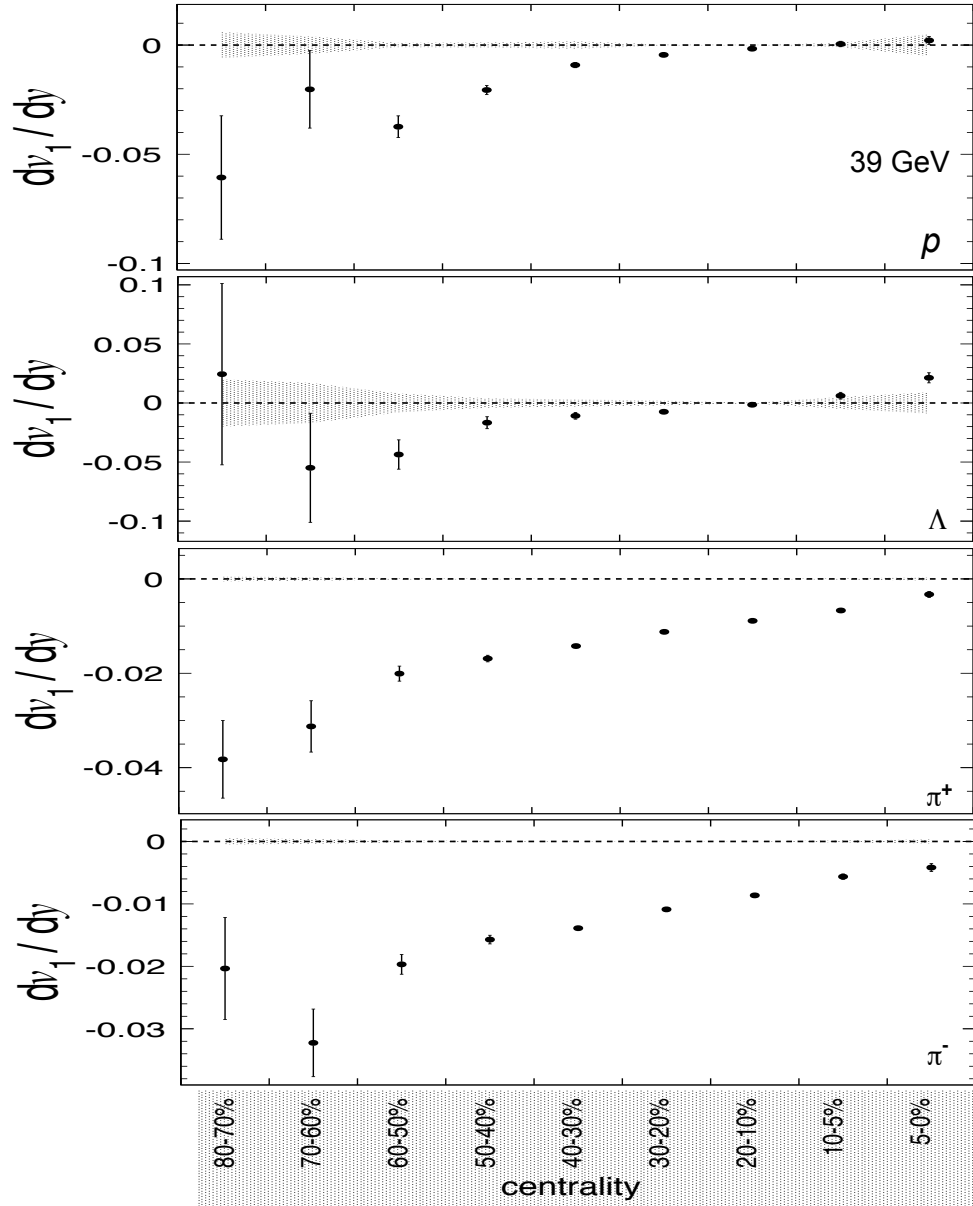


Figure 5.30: Systematic error for dv_1/dy as a function of centrality is shown for p , Λ , π^+ and π^- at a beam energy of 39 GeV.

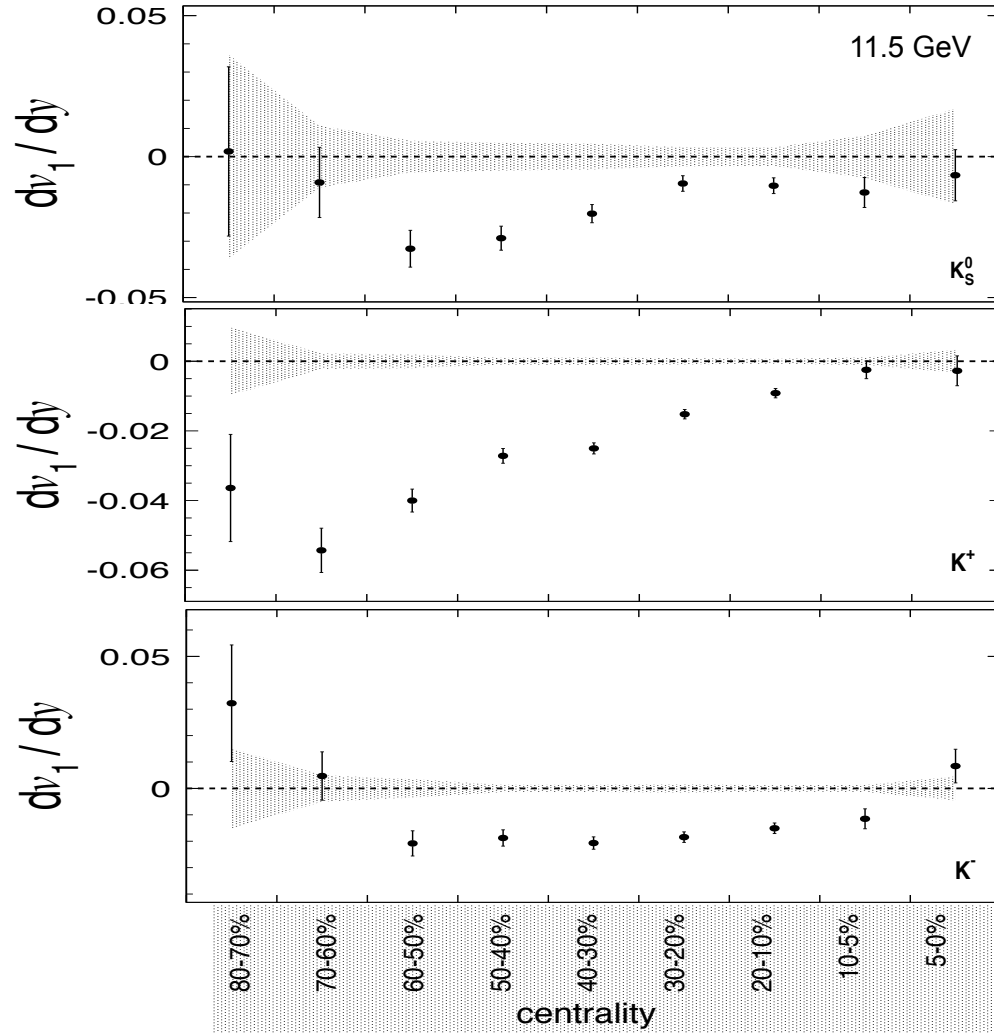


Figure 5.31: Systematic error for dv_1/dy as a function of centrality is shown for K^\pm and K_S^0 at a beam energy of 39 GeV.

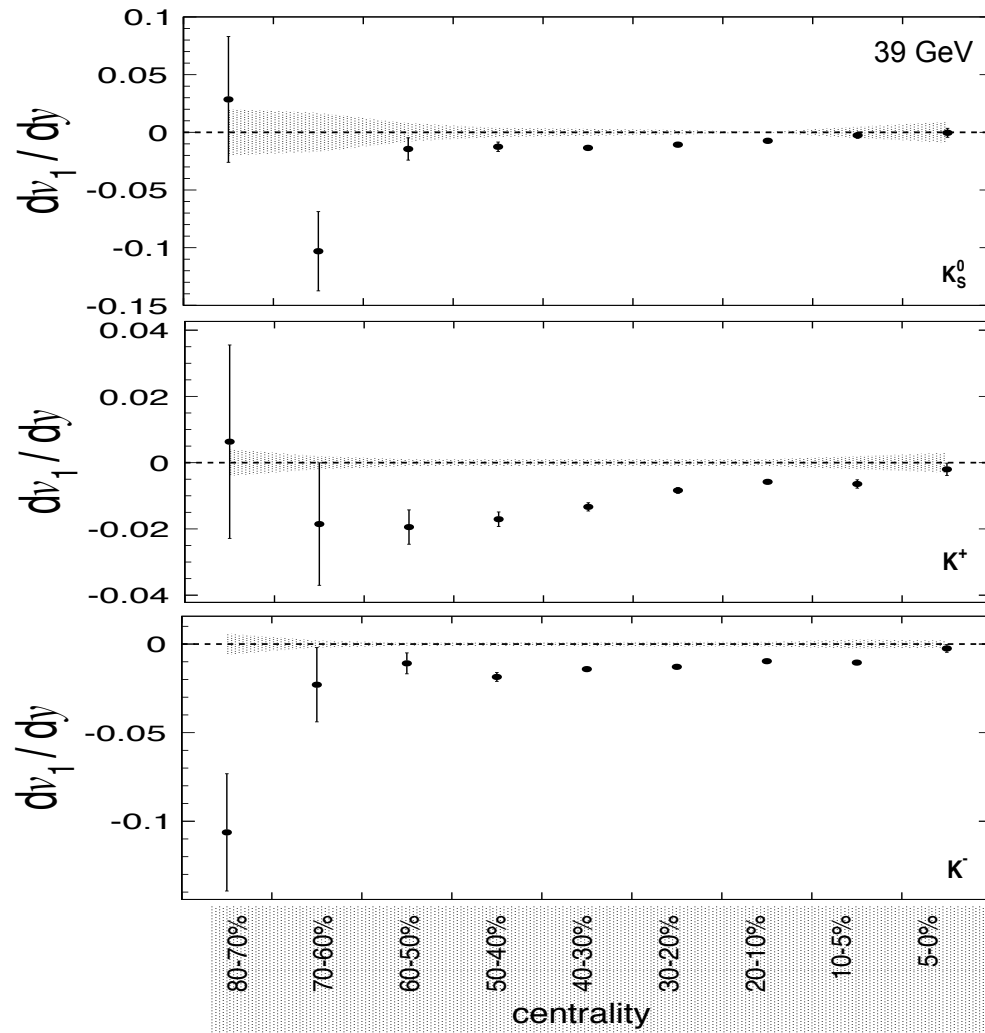


Figure 5.32: Systematic error for dv_1/dy as a function of centrality is shown for K^\pm and K_S^0 at a beam energy of 39 GeV.

CHAPTER 6

SUMMARY AND OUTLOOK

6.1 Summary

Understanding the matter created in a very early stage of the universe is of great interest in heavy-ion collision experiments. It is already reasonably clear that a QGP phase exists and is fleetingly produced in high-energy heavy-ion collisions. It is also widely accepted that a crossover transition happens at top RHIC energies and above, where the net baryon density in the participant fireball (the baryon chemical potential) is very close to zero. However, as we scan down in beam energy, the baryon chemical potential increases, and then the nature of the boundary between the QGP phase and the hadron gas phase is highly uncertain. It could remain a crossover, or there could be a region with a first-order phase transition. The question is of key interest in this dissertation research.

A first-order phase transition between QGP and hadronic gas is predicted in some models. A common pattern in theory papers is that a first-order phase transition is assumed to occur in certain regions of the QCD phase diagram, and then it is demonstrated that this assumption leads to a measurable dip in an experimental observable related to pressure in the highly excited early phase of the collision — such a pattern is called a softening of the equation of state. Typically, it is concluded that a measured dip of this kind would suggest softening, and softening would in turn suggest a first-order phase transition between the QGP phase and the hadron gas phase. A notable example of an observable that models indicate to be a good proxy for pressure in the highly excited early phase is directed flow of baryons near midrapidity.

In this dissertation analysis, I report the first measurement of beam energy dependence for directed flow of particle types Λ , $\bar{\Lambda}$, K_S^0 and K^\pm for Au+Au collisions. Furthermore, I also present measurements of directed flow centrality dependence for particle species Λ , p , π^\pm , K_S^0 , and K^\pm . The STAR experiment at Brookhaven National Laboratory has collected data at beam energies of $\sqrt{s_{\text{NN}}} = 7.7, 11.5, 14.5, 19.6, 27$ and 39 GeV, where the analyzed samples contain 4, 12, 20, 36, 70 and 130 million minimum-bias-trigger events, respectively. These data comprise a set known as Beam Energy Scan Phase-I (BES-I), and were acquired during the years 2010, 2011 and 2014. In a previous publication to quantify the strength of directed flow near midrapidity, STAR used a cubic fit to $v_1(y)$, the rapidity dependence of directed flow, and took the linear term of that fit as a single number to characterize the overall strength of the signal. In the present analysis, I use $dv_1/dy|_{y \leq 0.8}$ from a linear fit, because a cubic fit becomes unstable when used for particle types where statistics are limited, like Λ , $\bar{\Lambda}$, and K_S^0 . In an earlier study, linear and cubic fits were compared. The cubic fit offered smaller systematic uncertainties when statistics are good, but generally, both fit methods are consistent within errors.

A previous STAR publication for protons at BES energies in 10-40% central Au+Au collisions shows positive directed flow at $\sqrt{s_{\text{NN}}} = 7.7$ GeV, with a sign change around 11.5 GeV, followed by small and negative values for the higher BES energies. The energy point at 14.5 GeV was not available at that time. Now with the availability of data at 14.5 GeV, the proton directed flow slope shows a smooth trend and implies a minimum between 14.5 GeV and 19.6 GeV. The new measurements for Λ baryons show the same trend as protons within errors, and the Λ directed flow changes sign in the same beam energy region. This suggests that the trend seen in protons could be generalized for baryons. For Λ , a minimum in the directed flow slope is not resolvable due to large statistical uncertainty. Antiparticles \bar{p} and $\bar{\Lambda}$ shows similar trend to each other at higher BES energies, while at lower beam energies, $\bar{\Lambda}$ suffers from poor statistics. Charged kaons show negative directed flow slope for all BES energies, and closely follow each other except at 7.7 GeV. The directed flow slope for K_S^0 is consistent

with the average of K^+ and K^- within errors. Charged pions have negative slope for all BES energies and closely follow each other.

I also studied how directed flow slope depends on the exact region of centrality used to define 'intermediate centrality'. The default STAR definition of intermediate centrality is 10-40%. Three alternatives have been tested: 10-60%, 0-80% and 0-40%. These tests verify that the qualitative trend of directed flow slope does not depend on where intermediate centrality begins or ends. UrQMD model calculations, which assume a hadron gas phase throughout the collision, show large deviations from data for protons and Λ s, and follow a simple monotonic behavior, unlike the data. However, UrQMD shows a qualitatively similar trend as experiment for particle types \bar{p} , $\bar{\Lambda}$, π^\pm , K^\pm , and K_s^0 .

The final-state quark content of particles near midrapidity has contributions from produced quark-antiquark pairs and from initial-state quarks transported towards midrapidity by the stopping process of the collision. A net-particle analysis can help to disentangle these two contributions. Net-proton directed flow and net- Λ directed flow follow each other within errors and show a double sign-change at BES energies. Net-kaon directed flow shows a similar trend as net protons and net Λ s at 14.5 GeV and above, while below 14.5 GeV, net kaons remain negative. The reason for this pattern so far is not understood.

The centrality dependence of directed flow slope near midrapidity is calculated in narrow bins for particle types Λ , p , π^\pm , K_s^0 , and K^\pm . Statistics are too poor for \bar{p} and $\bar{\Lambda}$, and so these two species are not included in the centrality study. Centrality dependence could help to distinguish geometrical effects from phase transition effects. In hadronic transport models, a sign change happens at large impact parameters, and so this centrality study could offer useful discrimination. Particle types p , π^\pm and Λ show strong centrality dependence in the slope of directed flow. For p and Λ , a large negative slope is observed in peripheral collisions and this gradually decreases to zero around 10 to 30% centrality. Thereafter, the slope becomes small and positive for very central collisions. Charged pions also show a large negative slope in peripheral collisions, decreasing with increasing centrality, and become close to zero for

the most central collisions. Charged kaons and K_S^0 show qualitatively similar directed flow as charged pions, but with larger uncertainties. UrQMD calculations for protons show strong centrality dependence for most of the studied beam energies. However, the other studied particle species show much weaker centrality dependence.

6.2 Outlook

It is generally agreed in the heavy-ion community that strongly-interacting Quark Gluon Plasma, a new phase of matter, is being produced at top RHIC energies and at the CERN LHC. Now we are in a follow-up stage of studying the characteristics of the new phase of matter. The RHIC community has progressed to the stage of mapping the phase diagram of QCD matter via a beam energy scan (BES). During the first BES phase, the STAR collaboration has looked into the disappearance of QGP signatures at top RHIC energy, and searched for a critical point and a first-order phase boundary. Much progress has been made, but answers to the main physics questions remain open. Statistics available during Phase-One of the beam energy scan program are an important factor in limiting the strength of conclusions. Therefore Phase-Two of the beam energy scan has been approved to take data in 2019 and 2020. By then, the RHIC machine will have been upgraded significantly and will provide much improved luminosity at BES energies. The number of event provided will improve at least an order of magnitude. Furthermore, several detector upgrades at STAR will further increase statistics and will also improve acceptance, so that qualitative enhancements to the measurements can be achieved.

Overall, this dissertation research has resulted in a very substantial increase in the body of experimental measurements of directed flow at BES energies. The full physics impact of these new measurements will not be known until after a new round of comparisons with the latest state-of-the-art models.

Bibliography

- [1] K. G. Wilson, Phys. Rev. D **10**, 2445–2459 (1974).
- [2] F. Karsch, Nucl. Phys. **A698**, 199–208 (2002), arXiv:hep-ph/0103314 [hep-ph].
- [3] Y. Aoki, Z. Fodor, S. D. Katz, *et al.*, Phys. Lett. **B643**, 46–54 (2006), arXiv:hep-lat/0609068 [hep-lat].
- [4] Y. Aoki, S. Borsanyi, S. Durr, *et al.*, JHEP **06**, 088 (2009), arXiv:0903.4155 [hep-lat].
- [5] S. Borsanyi, Z. Fodor, C. Hoelbling, *et al.*, JHEP **09**, 073 (2010), arXiv:1005.3508 [hep-lat].
- [6] A. Bazavov *et al.*, Phys. Rev. **D85**, 054503 (2012), arXiv:1111.1710 [hep-lat].
- [7] Y. Aoki, G. Endrodi, Z. Fodor, *et al.*, Nature **443**, 675–678 (2006), arXiv:hep-lat/0611014 [hep-lat].
- [8] S. Ejiri, Phys. Rev. **D78**, 074507 (2008), arXiv:0804.3227 [hep-lat].
- [9] E. S. Bowman and J. I. Kapusta, Phys. Rev. **C79**, 015202 (2009), arXiv:0810.0042 [nucl-th].
- [10] E. Laermann and O. Philipsen, Ann. Rev. Nucl. Part. Sci. **53**, 163–198 (2003), arXiv:hep-ph/0303042 [hep-ph].
- [11] J. Stachel and K. Reygers, *Space-time evolution of the QGP*, (2015) http://www.physi.uni-heidelberg.de/~reygers/lectures/2015/qgp/qgp2015_06_space_time_evo.pdf.
- [12] *The star collaboration*, <http://http://www.star.bnl.gov/>.
- [13] *The phenix collaboration*, <http://www.phenix.bnl.gov/>.

- [14] A. Aduszkiewicz, *Acta Phys. Polon.* **B43**, 635 (2012), arXiv:1201.5879 [nucl-ex].
- [15] *Alternating gradient synchrotron*, <https://www.bnl.gov/rhic/AGS.asp>.
- [16] L. Adamczyk *et al.*, STAR Note SN0598 (2014).
- [17] J. Cleymans, H. Oeschler, K. Redlich, *et al.*, *Phys. Rev.* **C73**, 034905 (2006), arXiv:hep-ph/0511094 [hep-ph].
- [18] L. Kumar, *Nucl. Phys.* **A931**, 1114–1119 (2014), arXiv:1408.4209 [nucl-ex].
- [19] S. Das, *Nucl. Phys.* **A904-905**, 891c–894c (2013), arXiv:1210.6099 [nucl-ex].
- [20] I. Arsene *et al.*, *Nucl. Phys.* **A757**, 1–27 (2005), arXiv:nucl-ex/0410020 [nucl-ex].
- [21] B. B. Back *et al.*, *Nucl. Phys.* **A757**, 28–101 (2005), arXiv:nucl-ex/0410022 [nucl-ex].
- [22] J. Adams *et al.*, *Nucl. Phys.* **A757**, 102–183 (2005), arXiv:nucl-ex/0501009 [nucl-ex].
- [23] K. Adcox *et al.*, *Nucl. Phys.* **A757**, 184–283 (2005), arXiv:nucl-ex/0410003 [nucl-ex].
- [24] B. Back *et al.*, *et al.*, *Hot & Dense QCD Matter*, White Paper submitted to the 2012 Nuclear Science Advisory Committee.
- [25] J. Adams *et al.*, *Phys. Rev. Lett.* **92**, 052302 (2004), arXiv:nucl-ex/0306007 [nucl-ex].
- [26] S. S. Adler *et al.*, *Phys. Rev. Lett.* **91**, 182301 (2003), arXiv:nucl-ex/0305013 [nucl-ex].
- [27] L. Adamczyk *et al.*, *Phys. Rev.* **C88**, 014902 (2013), arXiv:1301.2348 [nucl-ex].
- [28] J. C. Dunlop, M. A. Lisa, and P. Sorensen, *Phys. Rev.* **C84**, 044914 (2011), arXiv:1107.3078 [hep-ph].
- [29] X.-N. Wang and M. Gyulassy, *Phys. Rev. Lett.* **68**, 1480–1483 (1992).
- [30] B. Berdnikov and K. Rajagopal, *Phys. Rev.* **D61**, 105017 (2000), arXiv:hep-ph/9912274 [hep-ph].
- [31] M. A. Stephanov, *Phys. Rev. Lett.* **102**, 032301 (2009), arXiv:0809.3450 [hep-ph].
- [32] M. Cheng *et al.*, *Phys. Rev.* **D79**, 074505 (2009), arXiv:0811.1006 [hep-lat].
- [33] R. V. Gavai and S. Gupta, *Phys. Lett.* **B696**, 459–463 (2011), arXiv:1001.3796 [hep-lat].

- [34] Y. Hatta and M. A. Stephanov, Phys. Rev. Lett. **91**, 129901 (2003).
- [35] L. Adamczyk *et al.*, Phys. Rev. Lett. **112**, 032302 (2014), arXiv:1309.5681 [nucl-ex].
- [36] B.-J. Schaefer and J. Wambach, Phys. Rev. **D75**, 085015 (2007), arXiv:hep-ph/0603256 [hep-ph].
- [37] A. M. Poskanzer and S. A. Voloshin, Phys. Rev. **C58**, 1671–1678 (1998), arXiv:nucl-ex/9805001 [nucl-ex].
- [38] H. Sorge, Phys. Rev. Lett. **78**, 2309–2312 (1997), arXiv:nucl-th/9610026 [nucl-th].
- [39] N. Herrmann, J. P. Wessels, and T. Wienold, Ann. Rev. Nucl. Part. Sci. **49**, 581–632 (1999).
- [40] B. Alver and G. Roland, Phys. Rev. **C81**, [Erratum: Phys. Rev. **C82**, 039903(2010)], 054905 (2010), arXiv:1003.0194 [nucl-th].
- [41] C. M. Hung and E. V. Shuryak, Phys. Rev. Lett. **75**, 4003–4006 (1995), arXiv:hep-ph/9412360 [hep-ph].
- [42] D. H. Rischke, Y. Pursun, J. A. Maruhn, *et al.*, Heavy Ion Phys. **1**, 309–322 (1995), arXiv:nucl-th/9505014 [nucl-th].
- [43] H. Stocker, Nucl. Phys. **A750**, 121–147 (2005), arXiv:nucl-th/0406018 [nucl-th].
- [44] Yu. B. Ivanov, E. G. Nikonov, W. Noerenberg, *et al.*, Heavy Ion Phys. **15**, 117–130 (2002), arXiv:nucl-th/0011004 [nucl-th].
- [45] V. D. Toneev, E. G. Nikonov, B. Friman, *et al.*, Eur. Phys. J. **C32**, 399–415 (2003), arXiv:hep-ph/0308088 [hep-ph].
- [46] J. Brachmann, S. Soff, A. Dumitru, *et al.*, Phys. Rev. C **61**, 024909 (2000).
- [47] L. Csernai and D. Röhrich, Physics Letters B **458**, 454–459 (1999).
- [48] R. J. M. Snellings, H. Sorge, S. A. Voloshin, *et al.*, Phys. Rev. Lett. **84**, 2803–2805 (2000), arXiv:nucl-ex/9908001 [nucl-ex].

- [49] L. Adamczyk *et al.*, Phys. Rev. Lett. **112**, 162301 (2014), arXiv:1401.3043 [nucl-ex].
- [50] R. C. P. Huovinen in Quark-Gluon Plasma 3, Eds: Hwa and X. N. Wang, World Scientific, Singapore, 616 (2003).
- [51] M. Bleicher and H. Stoecker, Phys. Lett. **B526**, 309–314 (2002), arXiv:hep-ph/0006147 [hep-ph].
- [52] Y. Guo, F. Liu, and A. Tang, Phys. Rev. C **86**, 044901 (2012).
- [53] C. Alt *et al.*, Phys. Rev. **C68**, 034903 (2003), arXiv:nucl-ex/0303001 [nucl-ex].
- [54] M. Isse, A. Ohnishi, N. Otuka, *et al.*, Phys. Rev. C **72**, 064908 (2005).
- [55] H. Liu *et al.*, Phys. Rev. Lett. **84**, 5488–5492 (2000), arXiv:nucl-ex/0005005 [nucl-ex].
- [56] M. D. Partlan, S. Albergo, F. Bieser, *et al.*, Phys. Rev. Lett. **75**, 2100–2103 (1995).
- [57] J. Barrette, R. Bellwied, S. Bennett, *et al.*, Phys. Rev. C **56**, 3254–3264 (1997).
- [58] S. A. Moszkowski, Phys. Rev. D **9**, 1613–1625 (1974).
- [59] P. Chung *et al.*, Phys. Rev. Lett. **86**, 2533–2536 (2001), arXiv:nucl-ex/0101002 [nucl-ex].
- [60] S. A. Bass *et al.*, Prog. Part. Nucl. Phys. **41**, [Prog. Part. Nucl. Phys.41,225(1998)], 255–369 (1998), arXiv:nucl-th/9803035 [nucl-th].
- [61] M. Bleicher *et al.*, J. Phys. **G25**, 1859–1896 (1999), arXiv:hep-ph/9909407 [hep-ph].
- [62] A. Muronga, Phys. Rev. C **69**, 034903 (2004).
- [63] J. Steinheimer, J. Auvinen, H. Petersen, *et al.*, Phys. Rev. C **89**, 054913 (2014).
- [64] V. P. Konchakovski, W. Cassing, Yu. B. Ivanov, *et al.*, Phys. Rev. **C90**, 014903 (2014), arXiv:1404.2765 [nucl-th].
- [65] Y. Nara, N. Otuka, A. Ohnishi, *et al.*, Phys. Rev. C **61**, 024901 (1999).
- [66] D. E. Kahana, D. Keane, Y. Pang, *et al.*, Phys. Rev. Lett. **74**, 4404–4407 (1995), arXiv:nucl-th/9405017 [nucl-th].

- [67] B.-A. Li and C. M. Ko, Phys. Rev. **C58**, 1382–1384 (1998), arXiv:nucl-th/9807088 [nucl-th].
- [68] Y. Nara, A. Ohnishi, and H. Stoecker, (2016), arXiv:1601.07692 [hep-ph].
- [69] T. Ludlam, Nuclear Instruments and Methods in Physics Research Section A: Accelerators, Spectrometers, Detectors and Associated Equipment **499**, The Relativistic Heavy Ion Collider Project: RHIC and its Detectors, 428–432 (2003).
- [70] M Adamczyk, L Antvorskov, K Ashktorab, *et al.*, Nuclear Instruments and Methods in Physics Research Section A: Accelerators, Spectrometers, Detectors and Associated Equipment **499**, The Relativistic Heavy Ion Collider Project: RHIC and its Detectors, 437–468 (2003).
- [71] B. Back *et al.*, Nuclear Instruments and Methods in Physics Research Section A: Accelerators, Spectrometers, Detectors and Associated Equipment **499**, The Relativistic Heavy Ion Collider Project: RHIC and its Detectors, 603–623 (2003).
- [72] K. Adcox *et al.*, Nuclear Instruments and Methods in Physics Research Section A: Accelerators, Spectrometers, Detectors and Associated Equipment **499**, The Relativistic Heavy Ion Collider Project: RHIC and its Detectors, 469–479 (2003).
- [73] K. Ackermann *et al.*, Nuclear Instruments and Methods in Physics Research Section A: Accelerators, Spectrometers, Detectors and Associated Equipment **499**, The Relativistic Heavy Ion Collider Project: RHIC and its Detectors, 624–632 (2003).
- [74] *RHIC accelerator complex*, (2016) <https://www.bnl.gov/rhic/complex.asp>.
- [75] M. Anderson, J. Berkovitz, W. Betts, *et al.*, Nuclear Instruments and Methods in Physics Research Section A: Accelerators, Spectrometers, Detectors and Associated Equipment **499**, The Relativistic Heavy Ion Collider Project: RHIC and its Detectors, 659–678 (2003).

- [76] L. Kotchenda, S. Kozlov, P. Kravtsov, *et al.*, Nuclear Instruments and Methods in Physics Research Section A: Accelerators, Spectrometers, Detectors and Associated Equipment **499**, The Relativistic Heavy Ion Collider Project: RHIC and its Detectors, 703 – 712 (2003).
- [77] J. Abele, J. Berkovitz, J. Boehm, *et al.*, Nuclear Instruments and Methods in Physics Research Section A: Accelerators, Spectrometers, Detectors and Associated Equipment **499**, The Relativistic Heavy Ion Collider Project: RHIC and its Detectors, 692 – 702 (2003).
- [78] F. Geurts, M. Shao, B. Bonner, *et al.*, Nuclear Instruments and Methods in Physics Research Section A: Accelerators, Spectrometers, Detectors and Associated Equipment **533**, Proceedings of the Seventh International Workshop on Resistive Plate Chambers and Related Detectors, 60 –64 (2004).
- [79] W. Llope, Nuclear Instruments and Methods in Physics Research Section A: Accelerators, Spectrometers, Detectors and Associated Equipment **661**, **Supplement 1**, X. Workshop on Resistive Plate Chambers and Related Detectors (RPC 2010), S110 – S113 (2012).
- [80] W. J. Llope *et al.*, Nucl. Instrum. Meth. **A522**, 252–273 (2004), arXiv:nuc1-ex/0308022 [nuc1-ex].
- [81] Y. Pandit, Ph.d. Dissertation (Kent State University, Kent, OH, July 2012).
- [82] D. Kharzeev and M. Nardi, Phys. Lett. **B507**, 121–128 (2001), arXiv:nuc1-th/0012025 [nuc1-th].
- [83] E. Sangaline, Ph.d. Dissertation (University of California, Davis, CA, 2014).
- [84] H. Bichsel, Nucl. Instrum. Meth. **A562**, 154–197 (2006).
- [85] M. Shao, O. Yu. Barannikova, X. Dong, *et al.*, Nucl. Instrum. Meth. **A558**, 419–429 (2006), arXiv:nuc1-ex/0505026 [nuc1-ex].

- [86] C. Amsler *et al.*, Phys. Lett. **B667**, 1–1340 (2008).
- [87] J. Beringer *et al.*, Phys. Rev. **D86**, 010001 (2012).
- [88] H. Long, Ph.d. Dissertation (University of California, Los Angeles, CA, 2002).
- [89] M. Lisa and I. Upsal, private communication, Aug. 2014.
- [90] I. Selyuzhenkov and S. Voloshin, Phys. Rev. **C77**, 034904 (2008), arXiv:0707.4672 [nucl-th].
- [91] J. Barrette *et al.*, Phys. Rev. **C56**, 3254–3264 (1997), arXiv:nucl-ex/9707002 [nucl-ex].
- [92] J.-Y. Ollitrault, Nucl. Phys. **A638**, 195–206 (1998), arXiv:nucl-ex/9802005 [nucl-ex].
- [93] N. Borghini, P. M. Dinh, J.-Y. Ollitrault, *et al.*, Phys. Rev. **C66**, 014901 (2002), arXiv:nucl-th/0202013 [nucl-th].
- [94] G. Agakishiev *et al.*, Phys. Rev. **C85**, 014901 (2012), arXiv:1109.5446 [nucl-ex].
- [95] P. Danielewicz, Phys. Rev. **C51**, 716–750 (1995), arXiv:nucl-th/9408018 [nucl-th].
- [96] J. Barrette *et al.*, Phys. Rev. **C55**, [Erratum: Phys. Rev.C56,2336(1997)], 1420–1430 (1997), arXiv:nucl-ex/9610006 [nucl-ex].
- [97] B. I. Abelev *et al.*, Phys. Rev. **C75**, 054906 (2007), arXiv:nucl-ex/0701010 [nucl-ex].
- [98] *RESTful API*, <http://www.ibm.com/developerworks/webservices/library/ws-restful/>.
- [99] T. A. Armstrong *et al.*, Nucl. Instrum. Meth. **A406**, 227–258 (1998).
- [100] R Brun, R Hagelberg, M Hansroul, *et al.*, *Simulation program for particle physics experiments, GEANT: user guide and reference manual* (CERN, Geneva, 1978).
- [101] *STAR GEANT framework*, <http://www.star.bnl.gov/public/comp/simu/newsite/gstar/gstar.html>.
- [102] M. Gyulassy and X.-N. Wang, Comput. Phys. Commun. **83**, 307 (1994), arXiv:nucl-th/9502021 [nucl-th].

[103] T. Sjostrand, S. Mrenna, and P. Z. Skands, JHEP **05**, 026 (2006), arXiv:hep-ph/0603175 [hep-ph].

[104] *Fermilab Test Beam Facility*, <http://ftbf.fnal.gov/>.

APPENDICES

APPENDIX A

SERVICE WORK FOR THE STAR COLLABORATION

In addition to the physics analysis work set out in detail in the main body of this dissertation, the appendices below provide a brief non-technical outline of two “community service” projects I have carried out at Brookhaven National Lab in support of the long-term goals of the STAR collaboration.

A.1 STAR Collaboration’s Record System Upgrade

The STAR collaboration’s record system is a collection of heterogeneous and sparse information associated with each member and institution, currently consisting of information about 550 members from about 58 institutions in 12 countries. In its original incarnation, only unstructured information was stored, revealing many restrictions such as a lack of historical data on changes, inability to keep track of members leaving and re-joining, and the inability to easily extend the saved information as new requirements appear.

My primary role in this project is to revisit the requirements, design and implementation. From the requirements, a tiered architecture design was proposed. This design was motivated by the fact that many STAR tools (such as the phonebook, and the shift sign-up interface) rely on the same logic and storage engine, and are a key and central feature for the maintainability of records. The back-end storage engine was upgraded to a data representation model based on key/value pairs, which allows for future extension of data storage without modifying other layers. The central service RESTful API [98] was used. RESTful API stands for representational state transfer application program interface, in which the server and the clients

are loosely coupled, which gives room to develop/update STAR applications and databases independently and leave no ambiguities.

The new re-factored database satisfies the set of emerging requirements, its flexible design allows reshuffling or extending the set of fields, and any change is automatically recorded into the historical records by the internal logic. A flexible set of presentation layers allows a web-based GUI for easy management of records and databases. A user-friendly public phone-book interface has been built for collaborators with advanced search capabilities. In addition, statistical displays of presentations given by each member and institution are provided to promote transparency, and also are used by STAR management to assist in even assignment of presentations across the collaboration.

A.2 Lead-Scintillating Fiber Calorimeter for STAR Forward Tracking

A forward calorimeter has been proposed to be installed on the west side of the STAR detector, by re-purposing AGS-E864 calorimeter cells [99] to achieve several goals in heavy-ion and spin physics. The proposed detector is capable of estimating the event plane through energy weighting, and unlike two older subsystems currently used for first-order event plane determination, the BBC and the ZDC-SMD, the new Fiber Calorimeter will be useful at all RHIC energies. In addition, it can be used in induced Λ polarization measurements, forward jets in asymmetric heavy-ion collisions, centrality selection, long-range near-side rapidity correlations, etc.

In this project, I am primarily responsible for developing a GEANT [100] model within the STAR GEANT framework [101], both for the 2014 prototype geometry and for the proposed 2017 geometry. Figures A.1 and A.2 show GEANT drawings of the 2014 and 2017 geometries, respectively. A complete analysis package was developed, which generates HIJING [102] and PYTHIA [103] events, feeds these events to the GEANT model to simulate detector responses, and stores the results from various STAR subsystems to data files. These data are then processed by experts for calibration and data analysis. The GEANT model I have developed is

sufficiently detailed to describe the material between the interaction point and the calorimeter, and shows very good agreement with real data recorded from calorimeter cells.

In addition, I was involved in pixelizing 10^2 cm AGS-E864 calorimeter cells into small three by three cells and assembling the cells on the west side of the STAR detector for testing in 2014. I have contributed to the construction of an LED-based light box to study the pixelized cell response, and to the assembly of a pre-shower detector. Also, I took part in a test beam study at the Fermilab Test Beam Facility (FTBF) [104] in Illinois to measure the energy resolution of the pixelized calorimeter cells. In this activity, a small-scale calorimeter was built from scratch, which gave me good experience in building a new detector.

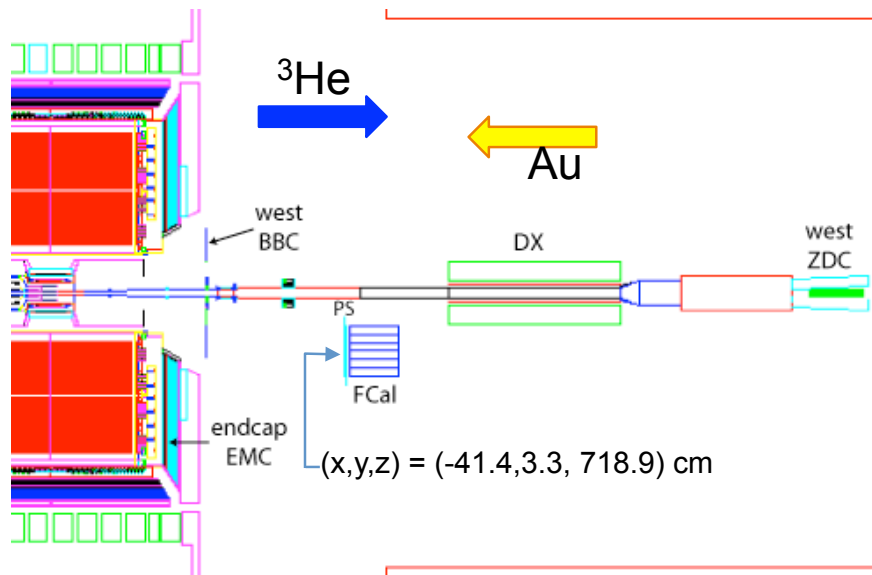


Figure A.1: GEANT drawing of the prototype built in 2014. A cross-sectional view of the calorimeter cells (FCal) and pre-shower (PS) detector is shown, along with the STAR detector and the beam pipe.

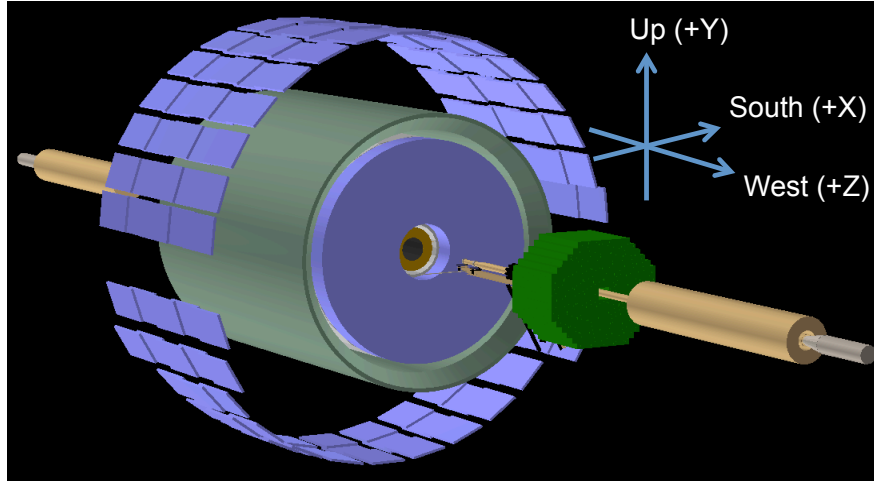


Figure A.2: GEANT drawing of the proposed arrangement of annular calorimeter cells, to be placed on the west side of the STAR detector. The calorimeter cells are shown in green.